

THE MOSDEF SURVEY: SIGNIFICANT EVOLUTION IN THE REST-FRAME OPTICAL EMISSION LINE EQUIVALENT WIDTHS OF STAR-FORMING GALAXIES AT $z = 1.4 - 3.8$

NAVEEN A. REDDY¹, ALICE E. SHAPLEY², RYAN L. SANDERS², MARISKA KRIEK³, ALISON L. COIL⁴, IRENE SHIVAEI⁵, WILLIAM R. FREEMAN¹, BAHRAM MOBASHER¹, BRIAN SIANA¹, MOJEGAN AZADI⁶, TARA FETHEROLF¹, FRANCESCA M. FORNASINI⁶, GENE LEUNG⁴, SEDONA H. PRICE⁷, TOM ZICK³, GUILLERMO BARRO⁸

submitted to ApJ on 2018 August 23, accepted 2018 October 29

ABSTRACT

We use extensive spectroscopy from the MOSFIRE Deep Evolution Field (MOSDEF) survey to investigate the relationships between rest-frame optical emission line equivalent widths (W) and a number of galaxy and ISM characteristics for a sample of 1134 star-forming galaxies at redshifts $1.4 \lesssim z \lesssim 3.8$. We examine how the equivalent widths of [O II] $\lambda\lambda$ 3727, 3730, H β , [O III] $\lambda\lambda$ 4960, 5008, [O III] + H β , H α , and H α + [N II] $\lambda\lambda$ 6550, 6585, depend on stellar mass, UV slope, age, star-formation rate (SFR) and specific SFR (sSFR), ionization parameter and excitation conditions (O32 and [O III]/H β), gas-phase metallicity, and ionizing photon production efficiency (ξ_{ion}). The trend of increasing W with decreasing stellar mass is strongest for [O III] (and [O III]+H β). More generally, the equivalent widths of all the lines increase with redshift at a fixed stellar mass or fixed gas-phase metallicity, suggesting that high equivalent width galaxies are common at high redshift. This redshift evolution in equivalent widths can be explained by the increase in SFR and decrease in metallicity with redshift at a fixed stellar mass. Consequently, the dependence of W on sSFR is largely invariant with redshift, particularly when examined for galaxies of a given metallicity. Our results show that high equivalent width galaxies, specifically those with high W ([O III]), have low stellar masses, blue UV slopes, young ages, high sSFRs, ISM line ratios indicative of high ionization parameters, high ξ_{ion} , and low metallicities. As these characteristics are often attributed to galaxies with high ionizing escape fractions, galaxies with high W are likely candidates for the population that dominates cosmic reionization.

Keywords: galaxies: abundances — galaxies: evolution — galaxies: high-redshift — galaxies: ISM — cosmology: reionization

1. INTRODUCTION

The rest-frame optical spectra ($\lambda_{\text{rest}} \simeq 3700 - 6750 \text{ \AA}$) of star-forming galaxies contain a number of important nebular emission and stellar photospheric absorption lines that serve as diagnostics of the star-formation rate (SFR), dust reddening, electron density, ionization parameter (\mathcal{U}), gas-phase metallicity, and stellar population. These basic properties have been well-characterized for large samples of local galaxies by surveys like the Sloan Digital Sky Survey (SDSS; York et al. 2000). Narrowband surveys have provided a view of subsets of the important diagnostic emission lines for galaxies at $z \gtrsim 1$ (e.g., Thompson et al. 1996; Malkan et al. 1996; Teplitz et al. 1998; Mannucci et al. 1998; Teplitz et al.

2000; Geach et al. 2008; Ly et al. 2012; Sobral et al. 2012, 2013; Ly et al. 2015; Suzuki et al. 2015; Ly et al. 2016; Khostovan et al. 2016; Matthee et al. 2017), while medium/broadband optical/near-IR and *Spitzer*/IRAC data have been used to estimate nebular line (e.g., H α + [N II] (+ [S II]), [O III]+H β) equivalent widths and fluxes at $z \gtrsim 2$ (e.g., Kriek et al. 2011; Shim et al. 2011; van der Wel et al. 2011; Labbé et al. 2013; Stark et al. 2013; Smit et al. 2014; Shivaie et al. 2015a; Smit et al. 2016; Faisst et al. 2016; Rasappu et al. 2016; Forrest et al. 2017; Malkan et al. 2017; Caputi et al. 2017; Castellano et al. 2017).

Concurrent with these largely photometrically based efforts at high redshift, advances in detector technology incorporated in the current generation of moderate resolution multi-object near-IR spectrographs have enabled direct and efficient spectroscopic measurements of rest-frame optical nebular emission lines for large samples of galaxies up to $z \sim 4$ (e.g., Förster Schreiber et al. 2009; Kashino et al. 2013; Schenker et al. 2013; Steidel et al. 2014; Kriek et al. 2015; Wisnioski et al. 2015; Tran et al. 2015; Holden et al. 2016; Nanayakkara et al. 2017). The *Hubble Space Telescope*'s grisms have provided an additional low-resolution ($R \lesssim 200$) probe of these features at $z \gtrsim 0.7$ (e.g., McCarthy et al. 1999; Atek et al. 2010, 2011; Trump et al. 2011; Straughn et al. 2011; Brammer et al. 2012; Fumagalli et al. 2012; Atek et al. 2014; Maseda et al. 2014). Taken together, these studies point to an increase in the mean equivalent widths of galaxies at a fixed stellar mass with redshift, reflecting an in-

¹ Department of Physics and Astronomy, University of California, Riverside, 900 University Avenue, Riverside, CA 92521, USA; naveenr@ucr.edu

² Department of Physics & Astronomy, University of California, Los Angeles, 430 Portola Plaza, Los Angeles, CA 90095, USA

³ Astronomy Department, University of California, Berkeley, Berkeley, CA 94720, USA

⁴ Center for Astrophysics and Space Sciences, University of California, San Diego, 9500 Gilman Drive, La Jolla, CA 92093-0424, USA

⁵ Steward Observatory, University of Arizona, 933 North Cherry Avenue, Tucson, AZ 85721, USA

⁶ Harvard-Smithsonian Center for Astrophysics, 60 Garden Street, Cambridge, MA 02138, USA

⁷ Max-Planck-Institut für Extraterrestrische Physik, Postfach 1312, Garching, D-85741, Germany

⁸ University of the Pacific, Stockton Campus, 3601 Pacific Avenue, Stockton, CA 95211, USA

crease in the rate at which galaxies are building up their stellar mass from $z \sim 2$ to $z \sim 6$ (e.g., Reddy et al. 2012a; Stark et al. 2013; González et al. 2014; Smit et al. 2014, 2016; Faisst et al. 2016). The elevated mean equivalent widths of rest-frame optical emission lines expected for high-redshift galaxies has also prompted the community to re-evaluate the contribution of such line emission to broadband photometry when modeling such photometry to discern the stellar populations in high-redshift galaxies, particularly those which may be faint and have low stellar masses (e.g., Anders & Fritze-v. Alvensleben 2003; Zackrisson et al. 2008; Schaerer & de Barros 2009; Trump et al. 2011; Stark et al. 2013; de Barros et al. 2014; González et al. 2014; Smit et al. 2014).

Many of the advances in our understanding of the ISM conditions in high-redshift galaxies have been based on data taken with the MOSFIRE spectrograph (McLean et al. 2012) on the Keck I telescope. This instrument operates from 0.97 to 2.45 μm , and enables the simultaneous spectroscopic observation of ≈ 30 individual galaxies while affording an increase in sensitivity of at least a factor of five relative to the previous generation of near-IR long-slit spectrographs on 8-10 m class telescopes. The resulting combination of multiplexing and sensitivity results in an increase in surveying efficiency of more than two orders of magnitude, a feature that has been exploited by surveys including the Keck Baryonic Structure Survey (KBSS; Steidel et al. 2014) and the MOSFIRE Deep Evolution Field (MOSDEF) survey (Kriek et al. 2015). Galaxies with moderate resolution rest-frame optical emission line measurements at $z \sim 1.4 - 3.8$ now number in the thousands.

Combining low-redshift galaxy survey data with near-IR spectroscopic and narrowband imaging campaigns of galaxies at $z \simeq 1.5 - 3.8$ has allowed the community to address how the physical conditions in star-forming galaxies have evolved over the last $\simeq 12$ Gyr of cosmic time. For example, several studies have suggested an increase in the ionization parameter with redshift at a fixed stellar mass (Hainline et al. 2009; Hayashi et al. 2015; Kewley et al. 2015; Shapley et al. 2015; Holden et al. 2016; Khostovan et al. 2016; Sanders et al. 2016b; Strom et al. 2017), an evolution that can be largely explained by the decrease in metallicity with redshift at a fixed stellar mass (i.e., the redshift evolution in the mass-metallicity relationship; e.g., Sanders et al. 2016b). Additionally, the mean electron density shifts toward higher values with increasing redshift, being an order of magnitude larger for typical star-forming galaxies at $z \sim 2$ relative to local galaxies of similar stellar masses (Sanders et al. 2016b; Strom et al. 2017). The conclusions regarding the high-excitation nature of high-redshift galaxies appear to be supported by inferences of rest-frame optical emission line equivalent widths in even higher redshift (e.g., $z \gtrsim 4$) galaxies (e.g., Shim et al. 2011; González et al. 2012; Stark et al. 2013; Labbé et al. 2013; de Barros et al. 2014; Smit et al. 2014, 2016), as well as by direct UV/optical spectroscopy of $z \gtrsim 4$ galaxies that indicate on average a harder ionizing radiation field relative to typical star-forming galaxies at $z \sim 2 - 3$ at a fixed stellar mass (Stark et al. 2015; Nakajima et al. 2016; Mainali et al. 2017; Schmidt et al. 2017; Smit et al. 2017; Shapley et al. 2017).

The relative ease of detecting high equivalent width emission lines in high-redshift galaxies leads us natu-

Table 1
Lines Used in This Study

Line	Rest-frame Vacuum Wavelength (\AA)
[O II]	3727, 3730
H β	4863
[O III]	4960, 5008
H α	6565
[N II]	6550, 6585

rally to ask the question of how such strong emission is connected to other characteristics of galaxies and, from the standpoint of demographics, how the properties of those strong line emitters compare with those of the general galaxy population at similar redshifts. In this vein, many of the aforementioned investigations have emphasized the utility of calibrations between rest-frame optical emission line equivalent widths and other observable and derived quantities that characterize galaxies, including their stellar population and ISM properties such as stellar mass, age, reddening, gas-phase metallicity, and ionization parameter. These calibrations and their redshift evolution may be used to estimate the physical conditions in galaxies from rather straightforward measurements of the equivalent widths of rest-frame optical emission lines. Furthermore, these calibrations serve as a reference against which rest-frame optical line measurements with *JWST* and future dark energy missions (e.g., *EUCLID*, *WFIRST*) may be interpreted. Finally, such relationships may be utilized to evaluate the impact of emission lines on broadband photometry which, when uncorrected, may bias the characterization of the stellar populations of high-redshift galaxies.

With these aims in mind, we use the extensive spectroscopic dataset of the MOSDEF survey to characterize the rest-frame optical emission line equivalent width distributions of star-forming galaxies as a function of stellar population and ISM characteristics. The sample analyzed in this paper consists of $> 1,000$ galaxies at redshifts $1.00 \leq z \leq 3.80$, most with multiple emission line measurements, making it one of the largest samples to date for which we can characterize the emission line equivalent width distributions at these redshifts. In this paper, we consider equivalent width measurements of [O II], H β , [O III], [O III]+H β , H α , and H α + [N II], and how these equivalent widths vary with certain galaxy and ISM properties. These lines and their rest-frame wavelengths are listed in Table 1.

The outline of this paper is as follows. In Section 2, we discuss the criteria for selecting galaxies in our sample; the methodology of fitting stellar population models to observed photometry; and the calculation of H α -based SFRs, metallicity- and excitation-sensitive line ratios, and line equivalent widths. Section 3 presents our main results on the correlations between emission line equivalent widths and various stellar population and ISM properties, both for the full sample and as a function of redshift. The physical context of the correlations between equivalent widths and galaxy and ISM properties is discussed in Section 4. Here, we investigate the physical causes of the trends we see and also discuss the redshift evolution of the equivalent widths. We also present a strategy for identifying high-excitation and high-ionization galaxies at high redshift. The appendices

present (a) a discussion of the line luminosity completeness of the MOSDEF survey over the range of stellar masses probed in this study; (b) the methodology used to calculate composite spectra; (c) a comparison between the measured $H\alpha$ equivalent widths and those predicted by models that assume different stellar metallicities and dust attenuation curves; and (d) corrections that can be used to estimate equivalent widths of single ionic species from low-resolution spectral or narrowband data where emission line features may be blended and/or confused. AB magnitudes are assumed throughout (Oke & Gunn 1983), and we adopt a Chabrier (2003) initial mass function (IMF) unless stated otherwise. Wavelengths are presented in the vacuum frame. We adopt a cosmology with $H_0 = 70 \text{ km s}^{-1} \text{ Mpc}^{-1}$, $\Omega_\Lambda = 0.7$, and $\Omega_m = 0.3$.

2. DATA, SAMPLE, AND MEASUREMENTS

2.1. MOSDEF Survey

The MOSDEF survey (Kriek et al. 2015) used the MOSFIRE instrument on the Keck I telescope to obtain *YJHK* spectroscopy of a large sample of rest-frame optical selected galaxies in three redshift windows— $z \simeq 1.37 - 1.70$, $2.09 - 2.70$, and $2.95 - 3.80$ —in the CANDLES fields (AEGIS, COSMOS, GOODS-N, GOODS-S, UDS; Grogin et al. 2011; Koekemoer et al. 2011). These redshift windows ensure the coverage of as many of the strong rest-frame optical emission lines (e.g., [O II], $H\beta$, [O III], $H\alpha$) that are accessible within the near-IR atmospheric transmission windows. The survey was conducted over 48.5 nights during the 2012B-2016A observing semesters.

Objects were selected from the 3D-HST photometric catalogs (Skelton et al. 2014) to limiting rest-frame optical magnitudes of $H = 24.0$, 24.5 , and 25.0 mag, respectively, for the three aforementioned redshift ranges, corresponding roughly to a limit in stellar mass of $\sim 10^9 M_\odot$. For comparison, the characteristic stellar mass derived from stellar mass functions at redshifts $1.4 \lesssim z \lesssim 3.8$ is $M^* \simeq (2.5 - 6.8) \times 10^{10} M_\odot$ (e.g., Davidzon et al. 2017). Thus, the MOSDEF sample probes galaxies that are anywhere from more than an order of magnitude less massive, to a factor of $\approx 3\times$ more massive, than typical galaxies at these redshifts. For brevity, we refer to the subsamples in the $z = 1.0 - 1.8$, $z = 1.8 - 2.7$, and $z = 2.7 - 4.0$ redshift ranges as the $z \sim 1.5$ (low-redshift), $z \sim 2.3$ (middle-redshift), and $z \sim 3.4$ (high-redshift) samples, respectively. Galaxies in the two lower redshift ranges (e.g., where some line ratios, such as [N II]/ $H\alpha$, are accessible) are hereafter referred to as lying in the $z \sim 2$ sample.

Objects were targeted for MOSFIRE spectroscopy if they had external spectroscopic redshifts, 3D-HST grism redshifts, and/or photometric redshifts that placed them in the redshift ranges specified above. Multi-object slit masks that primarily targeted objects in the two higher redshift intervals had integration times of ~ 2 hr in each band (*JHK* for the $z \sim 2.3$ sample, and *HK* for the $z \sim 3.4$ sample), while those targeting objects in the lowest redshift range had integration times of ~ 1 hr in each of the *YJH* bands. The adopted slit widths of $0''.7$ resulted in a spectral resolutions of $R \approx 3000 - 3650$. The very high spectroscopic success rate ($\sim 80\%$) of our survey resulted in redshifts for ≈ 1500 objects. Further details

on the target selection, observations, and spectroscopic data reduction are provided in Kriek et al. (2015).

2.2. Slit Loss Corrections and Line Flux Measurements

The continuum emission of the galaxies in the MOSDEF sample is generally not detected in individual spectra, with the exception of those objects with the brightest *H*-band magnitudes. As such, our method of computing the equivalent widths of lines relies on combining spectroscopic line flux measurements with continuum flux densities obtained from stellar population model fits to the photometry of galaxies. When computed in this way, the equivalent widths rely on accurate slit loss corrections to the line fluxes, as well as robust absolute flux calibrations based on slit stars observed simultaneously with the primary targets. The corrections for slit loss are based on modeling the two-dimensional *H*-band light distribution of galaxies and computing the amount of light passing through the slit while taking into account the seeing at the time the observations were obtained. Details on the slit loss calculations are provided in Kriek et al. (2015) and Reddy et al. (2015).

Line fluxes from the MOSFIRE spectra were measured by fitting Gaussian functions on top of a linear continuum (Kriek et al. 2015). The $H\alpha$ and $H\beta$ emission line fluxes were corrected for underlying Balmer absorption that arises from the stellar atmospheres of primarily A stars (with weaker contributions from B and F stars). These absorption lines are typically wider than the emission lines due to pressure broadening in stellar atmospheres. As such, the degree to which an emission line is corrected for Balmer absorption will depend on the amount by which the emission line fills the absorption line, or the “emission filling fraction” (f_{fill}). As the continuum, and hence the Balmer absorption, is not detected in the individual MOSDEF spectra, we computed an average filling fraction by constructing composite spectra (see Appendix B) of all galaxies where $H\alpha$ or $H\beta$ were covered in the individual spectra, regardless of whether the $H\alpha$ or $H\beta$ emission lines were detected. The average continuum, and average Balmer absorption, are significantly detected in the composite spectra. We simultaneously fit a Gaussian function with a negative amplitude to the $H\beta$ absorption and a Gaussian function with a positive amplitude to the $H\beta$ emission line in the composite spectrum. Due to its proximity to the [N II] doublet, the $H\alpha$ emission line was fit simultaneously with [N II], while the width of the underlying $H\alpha$ absorption line was fixed to that measured for the $H\beta$ absorption line. The two-component fit for $H\beta$ and multi-component fit for $H\alpha$ yielded a measure of the “true” average emission line flux, $f_{\text{em}}^{\text{two}}$, and the total absorbed flux, $f_{\text{abs}}^{\text{two}}$.

We then derived a second estimate of the emission line flux by assuming no absorption ($f_{\text{em}}^{\text{one}}$). To do this, we fit a single Gaussian function to the $H\beta$ emission line and a triple Gaussian function to the $H\alpha + [\text{N II}]$ complex in the composite spectrum, and assumed a flat continuum with no absorption, effectively mimicking the way in which line fluxes are measured in individual spectra. In order to compute $f_{\text{em}}^{\text{one}}$, we constrained the continuum level using a linear fit to the flux density points on either side of the Balmer absorption. The emission filling fraction is then

given by

$$f_{\text{fill}} = \frac{f_{\text{em}}^{\text{two}} - f_{\text{em}}^{\text{one}}}{f_{\text{abs}}^{\text{two}}}. \quad (1)$$

Performing these measurements on the composite spectra yielded values of $f_{\text{fill}} \simeq 0.36$ and 0.23 for $\text{H}\alpha$ and $\text{H}\beta$, respectively. For every galaxy, we computed the amount of absorbed flux from the best-fit stellar population model, multiplied this flux by f_{fill} , and added the resulting number to the measured $\text{H}\alpha$ and $\text{H}\beta$ emission line fluxes. The Balmer absorption corrections serve to increase the $\text{H}\alpha$ and $\text{H}\beta$ line fluxes by $\lesssim 1\%$ and $\lesssim 3\%$, respectively.

2.3. Sample Selection

To establish the sample analyzed in this paper, we considered only those objects that had secure spectroscopic redshifts measured from the MOSFIRE spectra. Specifically, to be included in our sample, the object must have either more than one emission line with an integrated line flux with $S/N \geq 3$, or a single emission line with an integrated line flux with $S/N \geq 3$ and a redshift from that single line that agrees with a previously published spectroscopic redshift. We excluded active galactic nuclei (AGNs) that were detected in the X-ray, and/or detected in all four of the *Spitzer*/IRAC channels and satisfied the Donley et al. (2012) criteria, and/or had an optical emission line ratio $\log[[\text{N II}]/\text{H}\alpha] > -0.4$ (Coil et al. 2015; Azadi et al. 2017). Finally, objects lying outside of the redshift range $1.0 \leq z_{\text{MOSFIRE}} \leq 4.0$ were excluded. These selection criteria resulted in a final sample of 1,134 unique objects with the spectroscopic redshift distribution shown in Figure 1. There are 21, 20, and 12 objects in the $z \sim 1.5$, $z \sim 2.3$, and $z \sim 3.4$ subsamples, respectively, that are not in our parent sample and are fainter than the H limits specified above, but for which we were able to derive redshifts as they happened to fall on spectroscopic slits assigned to other primary targets.

As discussed elsewhere (e.g., Shivaie et al. 2015b), the sample includes galaxies that are largely representative of “typical” star-forming galaxies at redshifts $1.0 \leq z \leq 4.0$, as judged by their distributions of SFRs and stellar masses. However, because the sample consists of galaxies selected by their rest-frame optical continuum (i.e., to the H limits specified above), it is highly incomplete for UV-faint blue star-forming galaxies, i.e., those that dominate the faint-end of the UV luminosity function. This incompleteness is illustrated in Figure 2, where the difference in apparent magnitude at rest-frame 1600 \AA and the apparent magnitude at $1.6 \mu\text{m}$ (i.e., the UV-optical color) is shown against the apparent magnitude at rest-frame 1600 \AA . The H limits adopted for the MOSDEF sample selection result in a distribution of colors that favors very red galaxies ($m_{1600 \times (1+z)} - m_{F160W} > 3$) at faint UV luminosities ($m_{1600 \times (1+z)} > 27$)—or at masses lower than $\simeq 10^9 M_{\odot}$ —over essentially the entire redshift range of interest. As such, in the following discussion we purposely avoid presenting relationships between equivalent widths and UV magnitude or UV luminosity, as these relationships will not be representative of the general galaxy population.

As we are primarily interested in how line equivalent widths vary with other galaxy properties, it is instructive

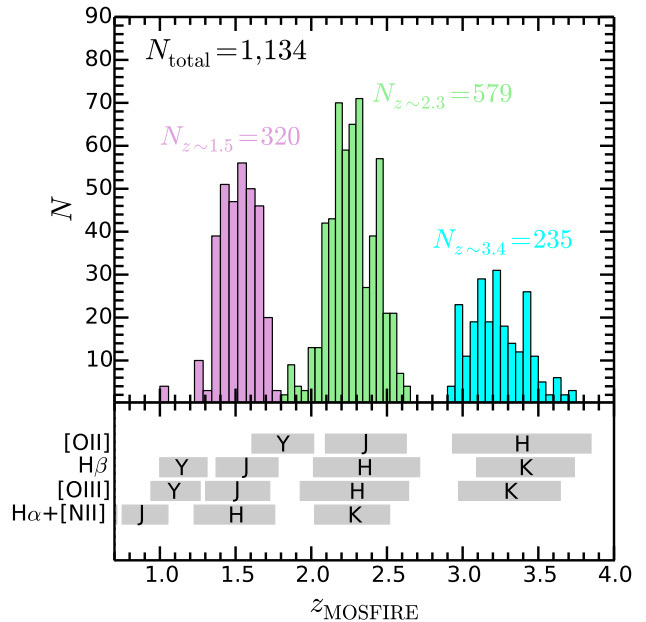


Figure 1. *Top:* Redshift distribution of the $N = 1,134$ galaxies in our sample, color-coded by the $z \sim 1.5$, $z \sim 2.3$, and $z \sim 3.4$ subsamples to which the galaxies belong. *Bottom:* Redshift ranges over which the strong rest-frame optical emission lines ($[\text{O II}]$, $\text{H}\beta$, $[\text{O III}]$, $\text{H}\alpha$, and $[\text{N II}]$) are shifted into the MOSFIRE $YJHK$ filters, as determined by the half-power points of the transmission profiles of these bands.

to determine the degree to which our sample is complete in line luminosity and equivalent width for galaxies of different masses. In Appendix A, we present evidence that the MOSDEF sample is complete in line luminosity over the range of stellar masses relevant for the current analysis (i.e., $M_* \gtrsim 10^9 M_{\odot}$).

The local reference sample used to evaluate the redshift evolution in line equivalent widths was drawn from Data Release 7 (DR7) of the SDSS (Abazajian et al. 2009). We combined the cataloged DR7 line fluxes and continuum flux densities to compute equivalent widths. SFRs and stellar masses for the local sample were also included in our analysis, where these values were computed using the techniques discussed in Brinchmann et al. (2004) and Salim et al. (2007). The DR7 SDSS sample was restricted to include only those objects with redshifts $0.04 \leq z \leq 0.1$ to minimize aperture effects and integrated line fluxes in $[\text{O II}]$, $\text{H}\beta$, $[\text{O III}]$, $\text{H}\alpha$, and $[\text{N II}]$ with $S/N \geq 3$. AGNs were excluded based on the Kauffmann et al. (2003) criteria. The resulting local comparison sample consists of 49,865 galaxies.

2.4. Stellar Population Modeling

Stellar masses, ages, color excesses, and star-formation rates (SFRs) were derived by modeling the photometry of galaxies in our sample—as assembled in the 3D-HST photometric catalogs (Skelton et al. 2014). The number of photometric bands that were modeled varies from 18 bands in UDS to 44 bands in COSMOS. The fiducial modeling assumes the Bruzual & Charlot (2003) (BC03) $Z = 0.004$ model, corresponding to $Z = 0.28Z_{\odot}$ on the current abundance scale (Asplund et al. 2009), for a constant SFR and reddened by an SMC extinction curve. These choices are based on previous studies that have suggested that typical (L^*) galaxies at $z \gtrsim 1.5$ can be

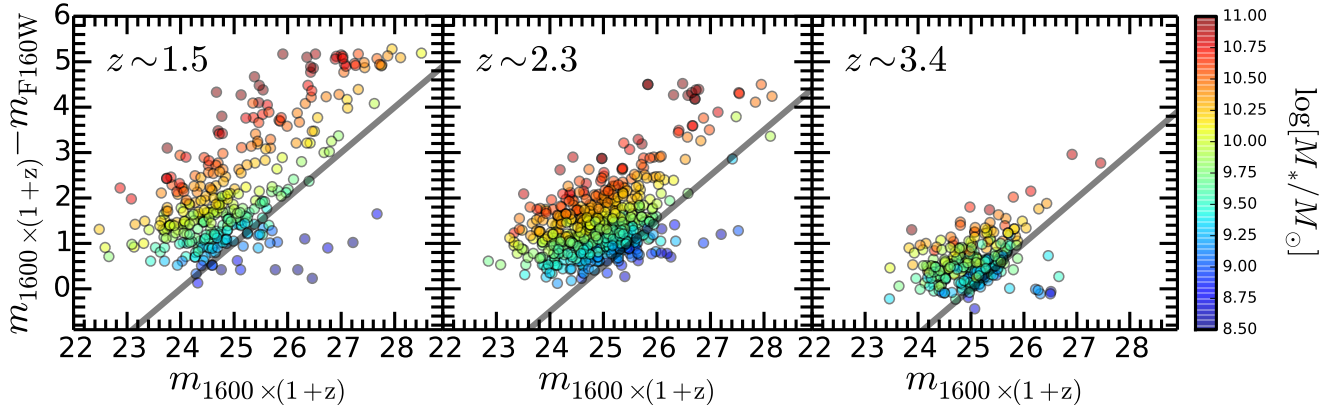


Figure 2. Distribution of UV-optical colors as a function of UV magnitude for galaxies in three redshift subsamples. The UV magnitude is taken to be the apparent magnitude at rest-frame 1600 Å, while the optical magnitude is taken to be the *HST* F160W (i.e., *H*) magnitude. The *H* limits of 24.0, 24.5, and 25.0 for the low, middle, and high redshift subsamples, respectively, are indicated by the solid lines in each panel. The few objects lying below these limits fell serendipitously on spectroscopic slits assigned to other (primary) targets, and were ones where we were able to derive redshifts that placed them in the redshift ranges of interest. All points are color-coded according to $\log[M_*/M_\odot]$.

approximated on average with a constant or rising star-formation history (Reddy et al. 2012a), and that steeper (e.g., SMC-like) attenuation curves are required to reproduce the dust obscurations (as constrained from far-infrared data) of sub-solar metallicity galaxies at high redshift (Reddy et al. 2018). In Appendix C, we provide further evidence that supports our default choice of the stellar metallicity and attenuation curve. The SMC curve assumed in our study is from Gordon et al. (2003), with a revised determination of the shape of the curve at $\lambda \simeq 950 - 1250$ Å from Reddy et al. (2016a). If applicable, the photometry was first corrected for the contribution from the strongest emission lines in the MOSFIRE spectra, including [O II], $H\beta$, [O III], and $H\alpha$. The age was allowed to vary from 50 Myr (approximating the dynamical timescale; e.g., Reddy et al. 2012b) to the age of the universe at the redshift of each galaxy. We considered a range of reddening from $0.0 \leq E(B-V)_{\text{stars}} \leq 0.6$. The best-fit stellar mass, reddening, age, and SED-inferred SFR (SFR[SED]) were taken to be those from the model that gave the minimum value of χ^2 relative to the photometry.

As the MOSDEF sample includes galaxies over a range of stellar masses, and hence stellar metallicities, we explore further in Appendix C how adopting a different metallicity stellar population model and attenuation curve for subsets of galaxies in our sample affects the calibrations between line equivalent widths and stellar population parameters.

2.5. $H\alpha$ SFRs

In addition to SED-derived SFRs, we also included $H\alpha$ SFRs (SFR[$H\alpha$], corrected for dust using the Balmer decrement) in our analysis, where the latter are computed using the methodology presented in Reddy et al. (2015) and Shivaei et al. (2015b). To maintain consistency with the assumptions adopted for the SED fitting, the $H\alpha$ luminosities were converted to SFRs based on the assumed stellar population models. Specifically, the factor required to convert $L(H\alpha)$ in units of erg s^{-1} to SFR[$H\alpha$] in units of $M_\odot \text{ yr}^{-1}$ is 3.236×10^{-42} for our fiducial model with a stellar metallicity of $0.28Z_\odot$. The

same factor for the $1.4Z_\odot$ BC03 constant star formation models is 4.457×10^{-42} . For comparison, the Kennicutt (1998) conversion factor is 4.165×10^{-42} assuming a Chabrier (2003) IMF, while the Hao et al. (2011) conversion factor is 4.634×10^{-42} for the same IMF.

2.6. Excitation-sensitive Line Ratios, Gas-phase Metallicities, and ξ_{ion}

We present relationships between equivalent widths and several excitation-sensitive line ratios. These ratios are summarized in Table 2, and include O32, which is sensitive to the ionization parameter. As the lines of this ratio are well-separated in wavelength, the [O III] λ 5008 and [O II] lines were corrected for dust attenuation assuming the reddening derived from the Balmer decrement ($H\alpha/H\beta$)—i.e., $E(B-V)_{\text{gas}}$ —and the Cardelli et al. (1989) extinction curve (e.g., see Sanders et al. 2016b). We also consider O3. This ratio was also corrected for dust in a manner similar to that for O32, though the dust corrections are small relative to the flux measurement errors given the proximity of the [O III] and $H\beta$ lines in wavelength. The two strong-line metallicity indicators examined here include the N2 and O3N2 indices. These indices were converted to gas-phase oxygen abundances based on the calibrations of Pettini & Pagel (2004).

All of the strong line ratios for SDSS galaxies were corrected for the contribution of diffuse ionized gas (DIG) and the effects of flux weighting from multiple emission regions using the prescriptions of Sanders et al. (2017) and assuming a DIG fraction of $f_{\text{dig}} = 0.55$, the median value for the sample of SDSS galaxies examined in Sanders et al. (2017). Aside from the DIG component, flux weighting from multiple emission regions, each of which may have different physical properties, can result in biases in globally measured line ratios relative to the median H II region properties. Some line ratios measured in local integrated galaxy spectra, such as O3 and N2, are biased primarily by the effects of flux weighting, while contributions from DIG emission dominate the biases in certain low-ionization line ratios, such as O2 (e.g., Sanders et al. 2017). The corrections applied to the local sample result in O3, O32, N2, and O3N2 ratios that

Table 2
Diagnostics Used in this Study

Diagnostic	Definition	Inferred Property
β (UV Slope)	$f_\lambda \propto \lambda^\beta$, $\lambda = 1268 - 2580 \text{ \AA}$	Reddening
ξ_{ion}	$\frac{Q(\text{H})}{L_{\text{UV}}} \text{ (Hz erg}^{-1}\text{)}^{\text{a}}$	Ionizing photon production efficiency
O32	$\frac{[\text{O III}]\lambda 5008}{[\text{O II}]\lambda 3727, 3730}$	Ionization parameter (U)
O3	$\frac{[\text{O III}]\lambda 5008}{\text{H}\beta}$	Excitation
N2	$\frac{[\text{N II}]}{\text{H}\alpha}$	Gas-phase Metallicity
O3N2	$\frac{\text{O3}}{\text{N2}}$	Gas-phase Metallicity
R23	$\frac{[\text{O II}] + [\text{O III}]}{\text{H}\beta}$	Gas-phase Metallicity

^a $Q(\text{H})$ is the number of ionizing photons produced per second, and is commonly inferred from the dust-corrected $\text{H}\alpha$ luminosity. L_{UV} is the dust-corrected UV luminosity density in units of $\text{erg s}^{-1} \text{Hz}^{-1}$.

are on average 0.76, 1.21, 0.93, and $0.78\times$ those of the uncorrected ratios, respectively. Similarly, the corrected values of R23 are on average $0.76\times$ those of the uncorrected values. Note that the equivalent widths of the lines were not corrected for DIG emission, as we are interested in establishing relations between the directly measured equivalent widths and the aforementioned galaxy and ISM properties.

We have *not* applied similar corrections to the line ratios for the high-redshift galaxies in the MOSDEF sample. As discussed in Sanders et al. (2017), the DIG contribution to emission line ratios for high-redshift galaxies is expected to be small ($\lesssim 20\%$) given their high SFR surface densities—a smaller DIG contribution is also observed for local starburst galaxies. Additionally, the high sSFRs and efficient feedback-driven metal mixing expected for high-redshift galaxies would suggest that flux-weighting effects play a minor role. Having noted that DIG contamination and flux-weighting effects are expected to be less severe for typical star-forming galaxies at high redshift, there are other possible factors that may complicate the interpretation of globally measured line ratios at high redshift, such as the presence of shocks or low-level AGN activity that may not reveal itself through the methods typically used to identify AGNs at high redshift.

Finally, we include in our analysis the ionizing photon production efficiency (ξ_{ion})—the ratio of the production rate of ionizing photons to the non-ionizing UV continuum luminosity density—as computed in Shivaee et al. (2018). To maintain consistency with the attenuation curve adopted in modeling the SEDs of the galaxies, we assumed the values of ξ_{ion} obtained with the SMC extinction curve: these are generally 0.3 dex larger than those obtained with the Calzetti attenuation curve (see Shivaee et al. 2018 for details).

2.7. Equivalent Width (W) Measurements

Equivalent widths (W) for all but the Balmer recombination lines were calculated by dividing the line flux by the continuum flux density, where the latter was determined from the flux density at line center from the best-fit stellar population model. For $W(\text{H}\alpha)$ and $W(\text{H}\beta)$,

the continuum flux density was computed as follows. We fit a linear function to the continuum flux density points of the best-fit SED model in two wavelength windows bracketing the Balmer absorption: $(\lambda_0 - 100) \times (1 + z)$ to $(\lambda_0 - 30) \times (1 + z)$ and $(\lambda_0 + 30) \times (1 + z)$ to $(\lambda_0 + 100) \times (1 + z)$, where λ_0 is the rest-frame wavelength of $\text{H}\alpha$ or $\text{H}\beta$ in \AA . The value of the linear function at $\lambda_0 \times (1 + z)$ was then taken to be the continuum flux density at line center.

As the best-fit model is determined as that which gives the minimum χ^2 relative to the observed photometry, varying the modeling assumptions (e.g., using a different stellar metallicity model or star-formation history) typically results in a small variation in the continuum flux density at line center. For example, assuming the BC03 “solar” metallicity models—corresponding to $1.4Z_\odot$ on the current abundance scale (Asplund et al. 2009)—results in continuum flux densities that are on average $\simeq 5\%$ lower, and hence line equivalent widths that are the same percentage higher, than those obtained with our fiducial modeling.

The reported equivalent widths of $[\text{O II}]$, $[\text{O III}]$, and $[\text{N II}]$ represent the sum of the equivalent widths of the individual lines of the doublets, in the case where both lines of the doublet are significantly detected with an integrated $S/N \geq 3$. If only one of the lines of the $[\text{O III}]$ or $[\text{N II}]$ doublet is undetected (typically because it either falls out of the spectral coverage or falls on a sky line), then the total equivalent width of the doublet is computed by assuming a 2.97 : 1 ratio of the flux of the stronger line of the doublet to the flux of the weaker line. For those galaxies where both $[\text{O III}]\lambda 4960$ and $[\text{O III}]\lambda 5008$ are covered and at least one line is detected, $\approx 96\%$ have a ratio, or limits on the ratio, of $[\text{O III}]\lambda 5008$ to $[\text{O III}]\lambda 4960$ that is within 5σ of the theoretical ratio of 2.97:1. If both lines of the doublet are undetected, then the upper limit in the total equivalent width is taken to be the quadrature sum of the upper limits on the equivalent widths of the individual lines of the doublet. Galaxies with upper limits in equivalent width are included in our analysis through the construction of composite spectra and the measurement of average equivalent widths,

as described in Appendix B. The equivalent widths of emission lines are taken to be positive and, unless stated otherwise, are divided by the factor $1+z$ and hence refer to the *rest-frame* values.

3. RELATIONS

In this section, we present the relationships between rest-frame optical emission line equivalent widths and several properties of the SEDs of high-redshift galaxies, including stellar mass, rest-frame UV slope (reddening), age, SFR, and specific SFR. We also discuss how the equivalent widths vary with several excitation-sensitive line ratios including O32 and O3, gas-phase oxygen abundance indicators including N2 and O3N2, and the ionizing photon production efficiency, ξ_{ion} . Readers who wish to proceed directly to a discussion of the physical context behind the redshift evolution in line equivalent widths may skip to Section 4.

3.1. Stellar Mass

The equivalent widths (W) of [O II], H β , [O III], [O III]+H β , H α , and H α + [N II] as a function of stellar mass are shown in Figure 3. The equivalent width of the H α + [N II]+ [S II] complex is roughly 0.09 dex larger on average—going from 0.07 dex larger to 0.11 dex larger than the H α + [N II] complex, and thus we only present results for the latter. The Spearman rank correlation coefficient, significance of correlation, and slope and intercept for the best-fit linear correlation between W and M_* —as is the case for all the other SED parameters considered here—are indicated in Table 8.⁹ These linear correlations are based on fitting the average equivalent widths measured from composite spectra of galaxies in bins of stellar mass (Appendix B), and thus include both detections and upper limits in equivalent width. Also listed in Table 8 are the total numbers of galaxies with detected and undetected lines, the total number of galaxies, and the redshift range and mean redshift of the galaxies. The Spearman tests indicate a high degree of correlation between W and M_* ($\sigma_{\text{P}} > 3$), such that galaxies with lower stellar masses have higher equivalent widths.

The trends between equivalent width and stellar mass are not surprising given that W is inversely proportional to the continuum flux density, and the continuum flux density is tightly correlated with the derived stellar mass. To guide the eye, the purple lines in Figure 3 indicate the arbitrarily normalized relationships between W and M_* under the assumption of a constant line luminosity. Because the equivalent widths of the different lines are correlated with stellar mass to different degrees, and with different slopes, we can conclude that the variation in W with M_* cannot solely be driven by changes in continuum flux density. In particular, it is clear from the comparison of the constant-line-luminosity (purple) line and the best-fit relation to $W([\text{O III}])$ versus M_* that the [O III] luminosity is roughly constant with mass above a

stellar mass of $\simeq 10^9 M_{\odot}$, while the line luminosity decreases with decreasing mass for other lines such as [O II], H β , and H α . More generally, we find that the equivalent widths of [O III] (and, hence, [O III]+H β) present the greatest variation with stellar mass. Galaxies with stellar masses of $M_* \approx 10^9 M_{\odot}$ have [O III] and [O III]+H β equivalent widths that are factor of $\simeq 7-9$ times higher than those of galaxies with $M_* \approx 10^{10.5} M_{\odot}$. As we will see shortly, the [O III] and [O III]+H β equivalent widths are more sensitive than any other line equivalent widths to essentially all of the observables and derived quantities examined here.

Figure 3 shows in more detail how the relationship between W and stellar mass varies with redshift, when dividing the MOSDEF sample into low, middle, and high-redshift bins. For each of these redshift bins, we further subdivided the galaxies into bins of stellar mass, constructed the composite spectrum in each of these redshift/stellar mass bins, and computed the average equivalent width from these composite spectra.

The relationship between equivalent width and stellar mass evolves with redshift (Figure 3). Among galaxies in the MOSDEF sample, we find that the equivalent width increases with redshift at a fixed stellar mass, a trend that is most pronounced when considering $W([\text{O III}])$. This trend has been noted before in the context of $W(\text{H}\alpha)$ (e.g., Fumagalli et al. 2012; Sobral et al. 2014) and $W([\text{O III}] + \text{H}\beta)$ (e.g., Khostovan et al. 2016). More generally, the equivalent widths of $z \sim 2.3$ galaxies in the MOSDEF sample are a factor of $\simeq 30\times$ larger than those of local galaxies at a fixed mass of $10^{9.7} M_{\odot}$, corresponding roughly to the average stellar mass of galaxies in our sample. In Section 4.1, we discuss how the redshift evolution in W versus M_* can be explained in terms of corresponding redshift evolutions in the SFR versus M_* and gas-phase metallicity versus M_* (i.e., the mass-metallicity or MZR) relations.

3.2. UV Slope

Another fundamental property of galaxy SEDs is the UV slope, an observable quantity that can be directly related to the reddening of the stellar population for star-forming galaxies given a dust attenuation curve (Table 2). Figure 4 shows the line equivalent widths as a function of the UV spectral slope. The UV slope was computed by fitting a power law through the observed photometry spanning the rest-frame wavelength range $\lambda = 1268-2580 \text{ \AA}$ (Calzetti et al. 1994). Spearman tests indicate that there are significant correlations between W and β , such that galaxies with bluer UV spectral slopes have larger equivalent widths (Table 8). In particular, while $W([\text{O II}])$ changes by only $\approx 30\%$ from galaxies with $\beta = -2.2$ to -0.7 , $W([\text{O III}])$ and $W([\text{O III}] + \text{H}\beta)$ change by a factor of $\simeq 2.5$ over the same range in UV slope. Given the monotonic relationship between UV slope and $E(B-V)_{\text{stars}}$ for simple star-formation histories, the trends between W and $E(B-V)_{\text{stars}}$ are similar to those obtained between W and β , such that galaxies with bluer stellar color excesses have higher equivalent widths on average than galaxies with redder stellar color excesses. Likewise, the trends observed between W and β are similar to those between W and the nebular, or gas, color excess, $E(B-V)_{\text{gas}}$. For brevity, the trends between W and $E(B-V)_{\text{stars}}/E(B-V)_{\text{gas}}$ are not shown

⁹ We note that massive galaxies with $M_* \gtrsim 10^{11} M_{\odot}$ may be under-represented in our sample given their rarity and the relatively small volumes probed with spectroscopy. However, the rarity of these massive galaxies suggests that their inclusion will not significantly affect the relationships between W and M_* presented here, particularly if they follow the same relationship between W and M_* as galaxies with more moderate stellar masses.

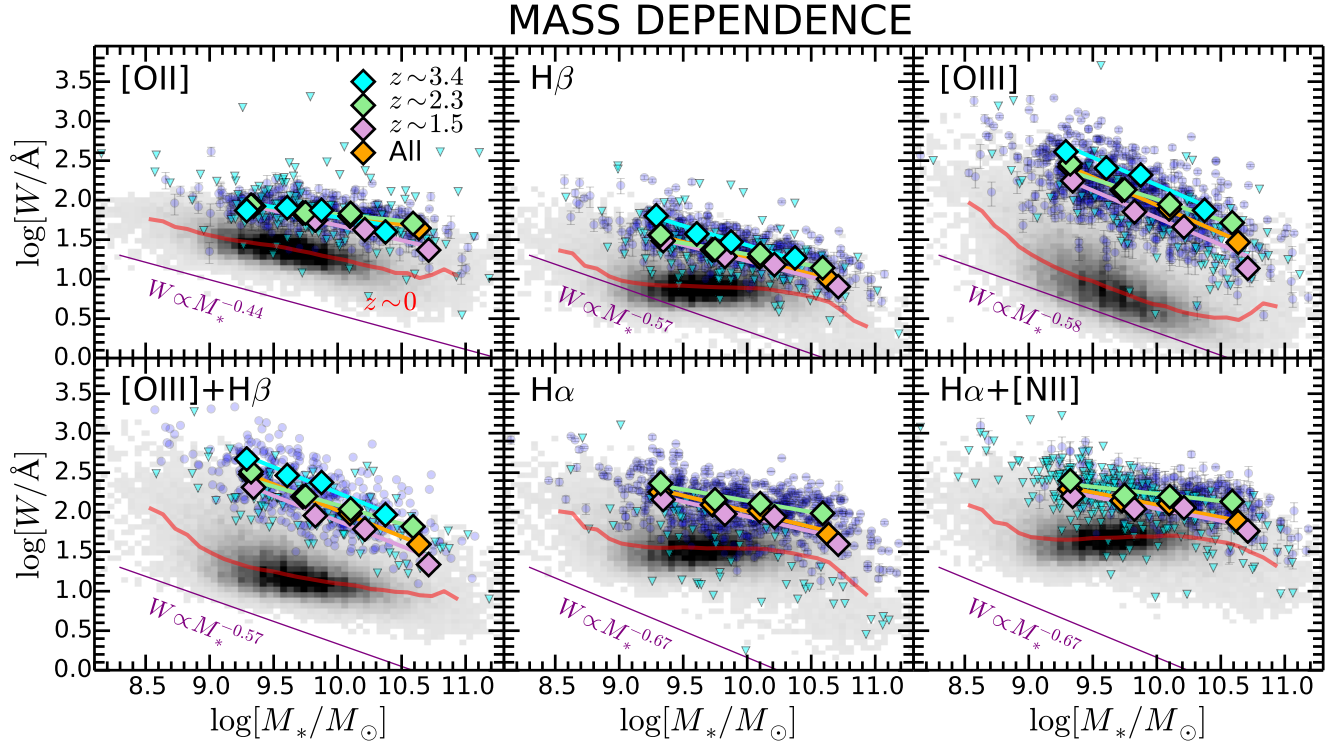


Figure 3. Rest-frame equivalent widths (W) of [O II], H β , [O III], [O III]+H β , H α , and H α + [N II], as a function of stellar mass for the full sample. Objects where the lines have been detected are indicated by the small light blue points, while objects with undetected lines have 3σ upper limits on the equivalent widths indicated by the small downward-pointing triangles. The large diamonds denote the average equivalent widths obtained from composite spectra of objects in four bins of stellar mass, and the thick solid line indicates the best-fit linear relation to the average values (parameters are given in Table 8). Average equivalent widths and best-fit linear relations are also shown for galaxies in three redshift bins ($z \sim 1.5$, $z \sim 2.3$, and $z \sim 3.4$). The distribution of equivalent width versus stellar mass for the local SDSS sample is shown in grayscale, where the red lines indicate the running median equivalent width as a function of stellar mass for the local sample. For reference, the thin solid purple lines indicate the arbitrarily normalized relationships between equivalent width and stellar mass for a constant line luminosity for galaxies in the MOSDEF sample.

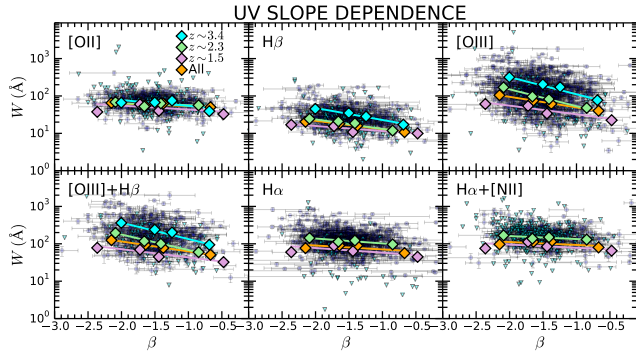


Figure 4. Rest-frame equivalent widths (W) of [O II], H β , [O III], [O III]+H β , H α , and H α + [N II], as a function of UV slope, β , for objects in the full sample. Symbols are the same as in Figure 3.

here.

The redshift evolution in the relationship between W and β is such that W increases with redshift at a fixed β . The mildest evolution occurs with W ([O II]), while the strongest evolution occurs with W ([O III]) and W ([O III]+H β). In the latter case, the equivalent widths increase on average by a factor of $\simeq 2$ and $\simeq 4$ at $z \sim 2.3$ and $z \sim 3.4$, respectively, relative to the values at $z \sim 1.5$. As the UV slope can be directly related to the reddening of the UV continuum, the redshift dependence of W versus β can be largely explained in terms of the relationship between UV slope/reddening and stellar mass, as discussed in Section 4.

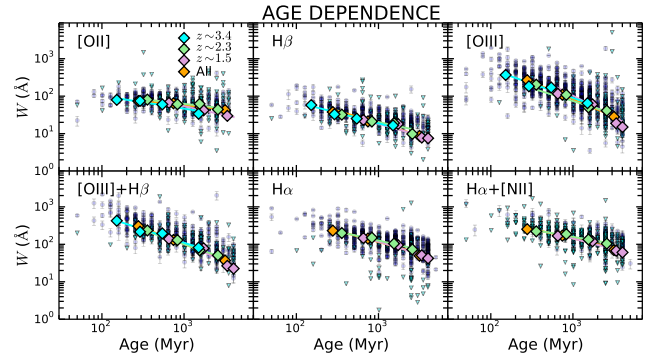


Figure 5. Rest-frame equivalent widths (W) of [O II], H β , [O III], [O III]+H β , H α , and H α + [N II], as a function of the luminosity-weighted stellar age for the full sample. Symbols are the same as in Figure 3.

3.3. Age

In the broadband stellar population modeling considered here, the luminosity-weighted stellar population age is constrained primarily by the shape or strength of the Balmer and 4000 Å breaks. The equivalent widths of all the strong rest-frame optical emission lines as a function of age are shown in Figure 5. The equivalent widths of recombination lines have long been used as proxies for stellar population age in star-forming galaxies for a simple reason. The recombination line equivalent widths are the ratios of the recombination line luminosities, which

are sensitive to the current rate of star formation, to the continuum luminosity densities, which are sensitive to the past average SFR. Thus, for simple star-formation histories, there is a direct correspondence between equivalent width and age (Stasińska & Leitherer 1996). While we find significant correlations between equivalent width and age for both $H\alpha$ and $H\beta$, the most significant correlation is found between $W([\text{O III}])$ (and $W([\text{O III}] + H\beta)$) versus age. While the $[\text{O III}]$ line luminosity is partly dependent on SFR, it is also sensitive to other factors including the hardness of the ionizing radiation field and metallicity. The fact that $W([\text{O III}])$ correlates more strongly with age than the Balmer recombination lines then suggests that these additional factors must also depend on age (e.g., see also Stasińska & Leitherer 1996; Gallazzi et al. 2005). In terms of the MOSDEF sample, the youngest galaxies have $[\text{O III}]$ equivalent widths that are an order of magnitude higher than those of the oldest galaxies.

Figure 5 shows that while the average age of galaxies in our sample decreases toward higher redshifts, the relationship between average equivalent width and age does not evolve strongly with redshift. Given that the age is sensitive to the shape of the SED (see above), we conclude that the equivalent width can serve as a rough proxy for spectral shape, independent of redshift. As we discuss below, this conclusion is supported by another probe of the spectral shape, namely the specific SFR. From a practical standpoint, the redshift invariance of the $\langle W \rangle$ versus $\langle \text{age} \rangle$ relationship would nominally suggest a promising avenue for estimating the *average* age of stellar populations based on simple measurements of line equivalent widths for high-redshift galaxies (e.g., Stasińska & Leitherer 1996). However, we must keep in mind that there is typically at least an order of magnitude spread in ages at a given W (Figure 5), not even accounting for an increase the spread of ages if one were to allow the star-formation history to vary between individual galaxies. Thus, the aforementioned relations may be useful for predicting average ages for large samples of high-redshift galaxies, but age estimates for individual galaxies should be treated with an abundance of caution.

3.4. SFR and sSFR

Because $\text{SFR}[\text{SED}]$ is tightly correlated with stellar mass (i.e., both quantities are sensitive to the normalization of the best-fit SED), we have chosen to focus instead on SFR measurements made independently of the SED fitting, namely SFRs derived from $H\alpha$. Figure 6 shows how the equivalent widths vary with $H\alpha$ -based SFRs ($\text{SFR}[H\alpha]$) for the two lower redshift bins where $H\alpha$ is accessible. In general, the correlations between W and $\text{SFR}[H\alpha]$ are less significant than those found for other trends (e.g., between W and M_* , or W and age). Specifically, there is only a weak dependence of the equivalent width as a function of $\text{SFR}[H\alpha]$ at a fixed redshift, though we note that galaxies at a fixed SFR have equivalent widths that increase with redshift—the only exception being $W([\text{O II}])$ versus $\text{SFR}[H\alpha]$, trends that do not change significantly between $z \sim 1.5$ and $z \sim 2.3$.

We find that W is very tightly correlated with the specific SFR, $\text{sSFR}[H\alpha]$, such that galaxies with larger sSFRs have higher equivalent widths (Figure 7). These tight relationships are directly related to the fact that

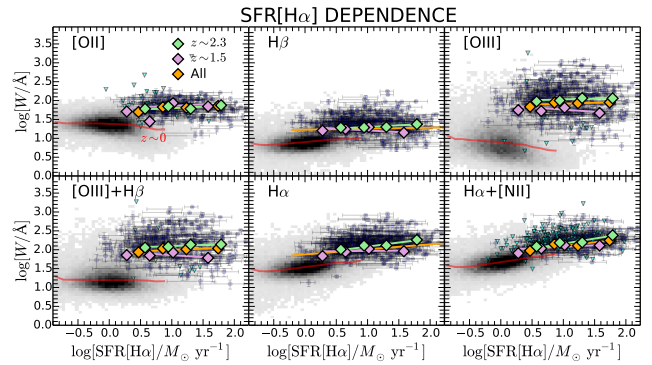


Figure 6. Rest-frame equivalent widths (W) of $[\text{O II}]$, $H\beta$, $[\text{O III}]$, $[\text{O III}] + H\beta$, $H\alpha$, and $H\alpha + [\text{N II}]$, as a function of the SFR inferred from the dust-corrected $H\alpha$ luminosity. Only those galaxies with significantly detected $H\alpha$ and $H\beta$ lines are shown. Symbols are the same as in Figure 3.

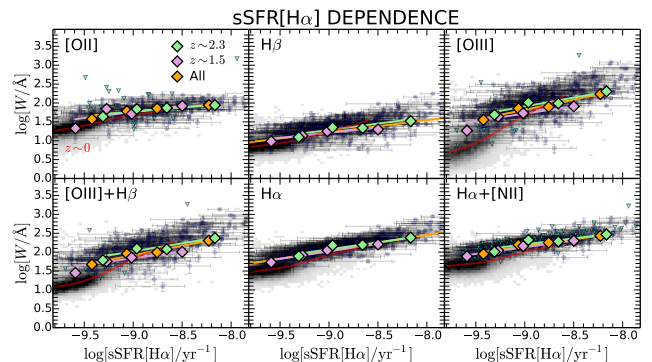


Figure 7. Rest-frame equivalent widths (W) of $[\text{O II}]$, $H\beta$, $[\text{O III}]$, $[\text{O III}] + H\beta$, $H\alpha$, and $H\alpha + [\text{N II}]$, as a function of the specific SFR, where the SFR is inferred from the dust-corrected $H\alpha$ luminosity. Only those galaxies with significantly detected $H\alpha$ and $H\beta$ lines are shown. Symbols are the same as in Figure 3.

equivalent width is a ratio of the line luminosity to continuum luminosity density, where the line luminosity is sensitive to SFR and where the continuum luminosity density is sensitive to stellar mass. Figure 3 shows that the equivalent width rises with redshift at a fixed mass. The redshift evolution of the $\text{SFR}-M_*$ relation implies that the sSFR rises with redshift at a fixed stellar mass. Hence, W is correlated with sSFR. It is also evident that the relationships between W and sSFR are largely redshift-invariant, a result that is also supported by the trends between W and $\text{sSFR}[\text{SED}]$ for galaxies in the $z \sim 1.5$, $z \sim 2.3$, and $z \sim 3.4$ redshift subsamples. This issue is discussed further in Section 4.5.

3.5. Excitation and Gas-phase Metallicity

The response of the ISM to the radiation field in high-redshift galaxies is reflected in the excitation-sensitive line ratios including O32 and O3. The ionizing properties of the massive stars that give rise to that radiation field can be ascertained from calculations of ξ_{ion} (e.g., Robertson et al. 2013; Bouwens et al. 2015; Shivaei et al. 2018). Another significant quantity associated with the state of the ISM is the gas-phase oxygen abundance. Here we examine how line equivalent widths vary with these properties of the ISM.

3.5.1. O32 (Ionization Parameter)

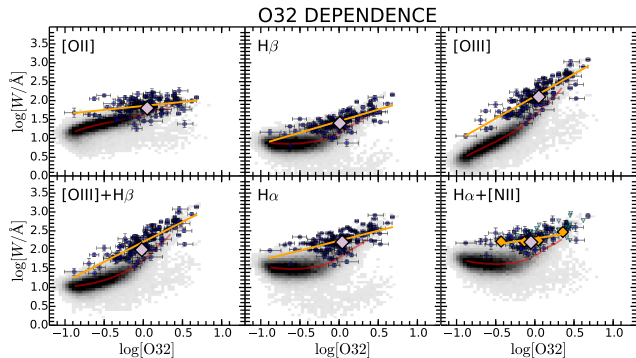


Figure 8. Rest-frame equivalent widths (W) of [O II], $H\beta$, [O III], [O III]+ $H\beta$, $H\alpha$, and $H\alpha$ + [N II], as a function of $\log[\text{O}32]$ for galaxies in the MOSDEF sample (*blue circles* and *cyan triangles*). The O32 values have been corrected for dust based on the Balmer decrement ($H\alpha/H\beta$). Thus, the figure shows only those objects where [O II], [O III], $H\beta$, and $H\alpha$ were all significantly detected, and only shows objects in the two lower redshift bins of our sample that have coverage of $H\alpha$. Orange diamonds in the lower rightmost panel indicate the mean equivalent width of $H\alpha$ + [N II] in bins of $\log[\text{O}32]$, while the orange lines in all panels indicate the mean trend in W versus $\log[\text{O}32]$. Purple diamonds denote the average values obtained from composite spectra of objects with spectral coverage of [O II], [O III], $H\beta$, and $H\alpha$, irrespective of whether the lines were detected. The distribution of local SDSS galaxies is shown in grayscale, with the running median trend indicated by the red line.

The dependence of the equivalent widths on O32, a proxy for the ionization parameter (U ; e.g., Sanders et al. 2016b), is shown in Figure 8, with details of the sample redshift ranges, number of galaxies, significance of correlation, and best-fit parameters given in Table 3. As noted earlier, the O32 values were corrected for dust attenuation based on the Balmer decrement, and thus the figure only shows those galaxies that had significant (i.e., $\geq 3\sigma$) detections of [O II], [O III], $H\beta$, and $H\alpha$. For reference, also shown are $\langle W \rangle$ and $\langle \log[\text{O}32] \rangle$ obtained from composite spectra that include galaxies where all four aforementioned lines were covered in the spectra, but not necessarily detected (*purple diamonds* in Figure 8). These average values lie close to the mean trend of W versus $\log[\text{O}32]$ obtained for objects with significant detections of all four lines, suggesting that galaxies where one or more of these lines may be undetected have a similar distribution in W and $\log[\text{O}32]$.

In general, we find that W is strongly correlated with O32. Of course, this is by construction for lines like [O II] and [O III], which enter into the calculation of O32. On the other hand, while the dust-corrected O32 values are dependent on the $H\alpha/H\beta$ ratio, they are less sensitive to the individual $H\alpha$ and $H\beta$ line luminosities. Even in this case, we find that the equivalent widths of $H\alpha$ and $H\beta$ increase with O32 (see also Kewley et al. 2015). We also computed the dust-corrected O32 for the SDSS sample of galaxies in the same manner as was done for the MOSDEF sample, with values indicated by the grayscale distribution in Figure 8. We note that correcting the $H\alpha$ and $H\beta$ emission lines for Balmer absorption in the local galaxies using the empirically derived prescription of Groves et al. (2012) does not significantly alter the dust corrections derived for O32 and, as such, the trends between W and O32 for local galaxies are affected only minimally. We remind the reader that the O32 values for the SDSS sample shown in this figure were corrected for

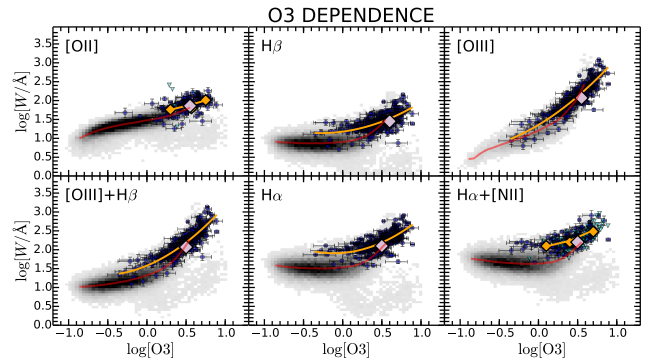


Figure 9. Rest-frame equivalent widths (W) of [O II], $H\beta$, [O III], [O III]+ $H\beta$, $H\alpha$, and $H\alpha$ + [N II], as a function of $\log[\text{O}3]$ for galaxies in the MOSDEF sample (*blue circles* and *cyan triangles*). The O3 values have been corrected for dust based on the Balmer decrement ($H\alpha/H\beta$). Thus, the figure shows only those objects where [O III], $H\beta$, and $H\alpha$ were all significantly detected, and only shows objects in the two lower redshift bins of our sample which have coverage of $H\alpha$. The orange lines indicate the best-fit quadratic trend between W and $\log[\text{O}3]$. Other symbols are the same as in Figure 8.

DIG emission (Section 2.6).

A comparison between the MOSDEF and SDSS samples suggests that there may be some mild redshift evolution in the W versus $\log[\text{O}32]$ relation, though the amount of evolution depends sensitively on whether O32 for the local sample is corrected for DIG emission. We return to this point in Section 4.4. At any rate, while the $z \sim 2$ MOSDEF sample is on average offset to higher O32 and W relative to the local sample, there are still substantial numbers of local “analog” galaxies that occupy the same region of W -O32 parameter space as the higher redshift galaxies.

3.5.2. O3

The O3 ratio is sensitive to both the ionization parameter and metallicity of the ISM, and thus may be expected to exhibit the same behavior with respect to equivalent widths as the O32 ratio. Figure 9 shows that this is indeed the case. Once again, we find a high significance of (positive) correlation between the equivalent widths and O3, particularly as it concerns $W([\text{O III}])$. As the $z \sim 2$ data indicate some curvature in the response of W to $\log[\text{O}3]$, we chose to fit second-order polynomials to the trends of W versus $\log[\text{O}3]$, with the best-fit parameters given in Table 4. Comparison with the local SDSS sample suggests that there is little, if any, redshift evolution in the trends between W and $\log[\text{O}3]$ as far as those galaxies with $\log[\text{O}3] \gtrsim 0.3$ are concerned. On the other hand, there may be some mild evolution of higher W at a given $\log[\text{O}3]$ below this threshold. However, as with O32, there are local galaxies that span the same parameter space in W versus O3 as the $z \sim 2$ galaxies.

3.5.3. Metallicity-sensitive Line Indices

There are several indices based on strong rest-frame optical emission lines that are used to estimate gas-phase oxygen abundances (Kewley & Ellison 2008). Abundances estimated from the N2 and O3N2 indices are advantageous as they rely on lines that are typically detected in $\sim L^*$ star-forming galaxies at high redshift, dust corrections are negligible owing to the close proximity in wavelength of the lines used to compute the O3

Table 3
Dependence of Equivalent Widths on O32, Oxygen Abundance, and ξ_{ion}

Attribute ^a	Line ^a	z -Range ($\langle z \rangle$) ^b	N (det/undet) ^c	ρ^d	σ_P^d	Intercept ^e	Slope ^e	RMS ^e
log[O32]	[O II]	1.604 – 2.545 (2.229)	125 (125/0)	0.34	4.7	1.858 ± 0.017	0.212 ± 0.059	0.18
	H β	1.604 – 2.545 (2.229)	125 (125/0)	0.75	10.0	1.456 ± 0.015	0.609 ± 0.053	0.17
	[O III]	1.604 – 2.545 (2.229)	125 (125/0)	0.81	11.8	2.114 ± 0.019	1.178 ± 0.068	0.21
	[O III]+H β	1.604 – 2.545 (2.229)	125 (125/0)	0.80	10.2	2.208 ± 0.018	1.058 ± 0.064	0.20
	H α	1.604 – 2.545 (2.229)	125 (125/0)	0.51	7.8	2.241 ± 0.018	0.525 ± 0.064	0.20
	H α + [N II]	1.688 – 2.545 (2.213)	118 (82/36)	0.48	5.9	2.298 ± 0.003	0.318 ± 0.007	0.18
$12 + \log[\text{O}/\text{H}]_{\text{N2}}$	[O II]	1.604 – 2.580 (2.246)	169 (158/11)	-0.53	6.9	7.806 ± 0.727	-0.719 ± 0.086	0.18
	H β	1.358 – 2.529 (2.053)	201 (189/12)	-0.62	8.9	11.775 ± 0.352	-1.245 ± 0.046	0.22
	[O III]	1.358 – 2.580 (2.044)	277 (257/20)	-0.61	10.4	19.111 ± 1.406	-2.049 ± 0.165	0.32
	[O III]+H β	1.358 – 2.527 (2.024)	170 (152/18)	-0.62	8.0	18.887 ± 1.927	-2.012 ± 0.305	0.30
	H α	1.005 – 2.580 (2.027)	360 (360/0)	-0.64	12.6	13.631 ± 0.482	-1.367 ± 0.069	0.21
	H α + [N II]	1.005 – 2.580 (2.027)	360 (360/0)	-0.55	10.4	10.960 ± 0.672	-1.039 ± 0.074	0.20
$12 + \log[\text{O}/\text{H}]_{\text{O3N2}}$	[O II]	1.604 – 2.483 (2.219)	81 (80/1)	-0.62	7.0	10.607 ± 1.246	-1.054 ± 0.150	0.16
	H β	1.390 – 2.527 (2.026)	151 (151/0)	-0.69	9.5	12.121 ± 0.846	-1.286 ± 0.101	0.19
	[O III]	1.390 – 2.527 (2.026)	151 (151/0)	-0.88	13.0	25.074 ± 1.047	-2.771 ± 0.125	0.19
	[O III]+H β	1.390 – 2.527 (2.026)	151 (151/0)	-0.86	11.1	21.965 ± 0.981	-2.385 ± 0.117	0.19
	H α	1.390 – 2.527 (2.026)	151 (151/0)	-0.70	10.8	12.987 ± 0.851	-1.297 ± 0.102	0.16
	H α + [N II]	1.390 – 2.527 (2.026)	151 (151/0)	-0.63	9.5	10.898 ± 0.862	-1.035 ± 0.103	0.16
$\log[\xi_{\text{ion}}/\text{Hz erg}^{-1}]$	[O II]	1.581 – 2.654 (2.251)	170 (150/20)	0.29	4.1	-6.013 ± 1.025	0.307 ± 0.040	0.19
	H β	1.368 – 2.654 (2.080)	332 (332/0)	0.30	5.5	-4.423 ± 1.053	0.230 ± 0.042	0.26
	[O III]	1.369 – 2.586 (2.064)	281 (270/11)	0.33	6.2	-10.969 ± 1.562	0.506 ± 0.061	0.41
	[O III]+H β	1.369 – 2.586 (2.064)	281 (270/11)	0.35	5.9	-10.116 ± 1.587	0.476 ± 0.063	0.37
	H α	1.369 – 2.654 (2.080)	332 (332/0)	0.69	13.6	-10.343 ± 0.699	0.494 ± 0.028	0.19
	H α + [N II]	1.390 – 2.654 (2.050)	304 (201/103)	0.66	10.6	-11.324 ± 0.819	0.531 ± 0.032	0.21

^a Statistics are presented for the relationship between $\log[W/\text{\AA}]$ for the line (or lines) listed under column heading “Line” and the property listed under column heading “Attribute.”

^b Redshift range and mean redshift of objects in this subsample.

^c Total number of objects and the number of detections and non-detections of the line (or lines) listed under column heading “Line.”

^d Spearman rank correlation coefficient and the number of standard deviations by which the correlation deviates from the null hypothesis of no correlation.

^e Intercept and slope of the best-fit linear function to the composite averages, and the rms of the data points about this best-fit linear function.

Table 4
Dependence of Equivalent Widths on $\log[\text{O3}]$

Line ^a	z -Range ($\langle z \rangle$) ^b	N (det/undet) ^c	ρ^d	σ_P^d	Coefficients ^e	RMS ^e
[O II]	1.604 – 2.545 (2.220)	124 (116/8)	0.53	5.6	$c_0 = 1.635 \pm 0.053$; $c_1 = 0.346 \pm 0.224$; $c_2 = 0.197 \pm 0.249$	0.19
H β	1.357 – 2.586 (2.069)	241 (241/0)	0.61	9.4	$c_0 = 1.178 \pm 0.029$; $c_1 = 0.278 \pm 0.124$; $c_2 = 0.498 \pm 0.155$	0.20
[O III]	1.357 – 2.586 (2.069)	241 (241/0)	0.88	13.6	$c_0 = 1.357 \pm 0.028$; $c_1 = 1.241 \pm 0.121$; $c_2 = 0.530 \pm 0.151$	0.20
[O III]+H β	1.357 – 2.586 (2.069)	241 (241/0)	0.85	13.2	$c_0 = 1.580 \pm 0.028$; $c_1 = 0.863 \pm 0.121$; $c_2 = 0.727 \pm 0.152$	0.20
H α	1.357 – 2.586 (2.069)	241 (241/0)	0.67	10.4	$c_0 = 1.917 \pm 0.029$; $c_1 = 0.171 \pm 0.127$; $c_2 = 0.750 \pm 0.159$	0.20
H α + [N II]	1.390 – 2.586 (2.040)	217 (140/77)	0.64	7.6	$c_0 = 2.067 \pm 0.028$; $c_1 = 0.150 \pm 0.126$; $c_2 = 0.699 \pm 0.181$	0.18

^a Statistics are presented for the relationship between $\log[W/\text{\AA}]$ for the line (or lines) listed in this column and $\log[\text{O3}]$.

^b Redshift range and mean redshift of objects in this subsample.

^c Total number of objects and the number of detections and non-detections of the line (or lines) listed under column heading “Line.”

^d Spearman rank correlation coefficient and the number of standard deviations by which the correlation deviates from the null hypothesis of no correlation.

^e Coefficients of the best-fit quadratic function of the form $c_0 + c_1x + c_2x^2$, and the rms of the data points about this best-fit quadratic function.

and N2 indices, and the indices vary monotonically with abundance, unlike the R23 index. On the other hand, the R23 index may be preferable given apparent anomalies in oxygen abundances derived based on nitrogen lines for high-redshift galaxies. We discuss these issues further in Section 4.4.

Oxygen abundances estimated from the N2 and O3N2 indices are shown in Figures 10 and 11, and the redshift ranges, significance of correlations, and best-fit parameters for the different subsamples are listed in Table 3. Not shown are galaxies with either upper or lower limits in oxygen abundance: most of these galaxies have upper limits in N2, and including them will make the best-fit slopes of the relations shown in Figure 10 slightly

less negative. In general, inclusion of galaxies with either upper or lower limits in oxygen abundance will not shift the relations shown in Figures 10 and 11 enough for them to completely overlap with the locus of where most $z \sim 0$ galaxies lie. The data indicate significant correlations between equivalent widths and oxygen abundance, such that galaxies with higher W have lower oxygen abundances. These correlations are undoubtedly a by-product of the relationships between metallicity and stellar mass, and between W and stellar mass (Figure 3). As with many of the other parameters we have examined, $W([\text{O III}])$ shows the most significant variation with metallicity given the steeper (i.e., more negative) slope of $W([\text{O III}])$ versus $12 + \log[\text{O}/\text{H}]$ relative to those derived

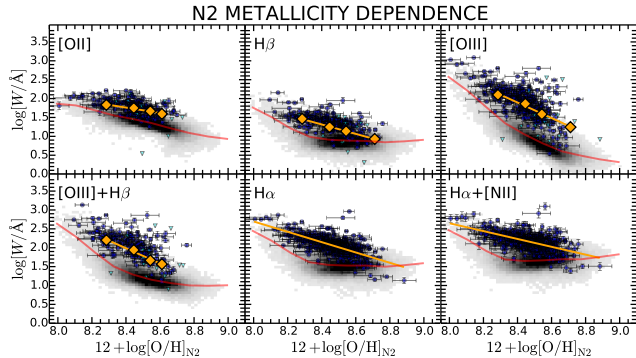


Figure 10. Rest-frame equivalent widths (W) of [O II], $H\beta$, [O III], [O III]+ $H\beta$, $H\alpha$, and $H\alpha$ +[N II], as a function of the gas-phase oxygen abundance inferred from the N2 index, and assuming the Pettini & Pagel (2004) calibration, for galaxies in the MOSDEF sample (*blue* circles and *cyan* triangles). The same is shown for the local SDSS sample in grayscale. Symbols are the same as in Figure 8. Stacked points are shown only in those panels where for some galaxies the corresponding line equivalent width have upper limits.

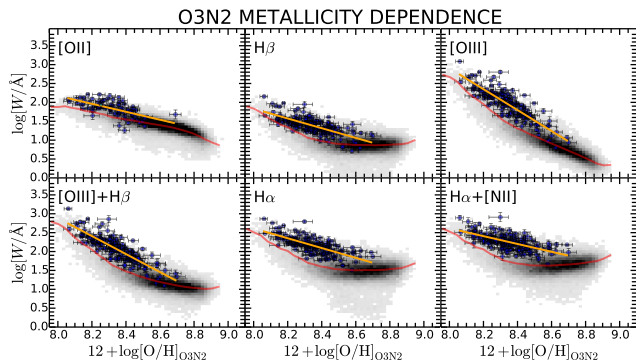


Figure 11. Rest-frame equivalent widths (W) of [O II], $H\beta$, [O III], [O III]+ $H\beta$, $H\alpha$, and $H\alpha$ +[N II], as a function of the gas-phase oxygen abundance inferred from the O3N2 index and assuming the Pettini & Pagel (2004) calibration. Symbols are the same as in Figure 10.

for the other lines.

Abundances for the local SDSS sample were computed in the same way as for the MOSDEF sample, and are denoted by the grayscale distributions in Figures 10 and 11. Comparison with the local sample suggests that galaxies at $z \sim 2$ have $\simeq 0.2 - 0.5$ dex larger $\log[W/\text{\AA}]$ at a given oxygen abundance. Despite these average offsets, the $z \sim 2$ galaxies lie within the distribution of W versus $12 + \log[\text{O}/\text{H}]$ found for local galaxies.

3.6. Ionizing Photon Production Efficiency (ξ_{ion})

As noted earlier, ξ_{ion} is a convenient metric for characterizing the hardness of the far-UV spectra of galaxies, in particular the production rate of ionizing photons relative to the SFR. Shivaei et al. (2018) present the most comprehensive analysis of how ξ_{ion} varies with a number of other galaxy/ISM properties, including stellar mass, ionization parameter, metallicity, and age. Here, we focus on how the equivalent widths of the strong rest-frame optical emission lines vary with ξ_{ion} .

Figure 12 shows the equivalent widths of [O II], $H\beta$, [O III], [O III]+ $H\beta$, $H\alpha$, and $H\alpha$ +[N II] as a function of ξ_{ion} . Spearman tests indicate a high degree of significance in the correlations between W and ξ_{ion} (e.g.,

see Table 3), such that galaxies with larger ξ_{ion} have higher line equivalent widths. Note that the scatter in the trends between the Balmer lines ($H\alpha$ in particular) and ξ_{ion} is artificially tight as $H\alpha$ and the Balmer decrement are used, in part, to compute ξ_{ion} . Nevertheless, if we consider [O III]—a line that is not used in the computation of ξ_{ion} —we still find a significant positive correlation between line equivalent width and ξ_{ion} , albeit with a large scatter (e.g., see also ? and Tang et al. 2018). Specifically, $W([\text{O III}])$ varies by an order of magnitude (or more) at a given ξ_{ion} . However, it is clear from the upper rightmost panel of Figure 12 that galaxies with the highest $W([\text{O III}]) \gtrsim 500 \text{\AA}$ exclusively have ξ_{ion} that exceed the value typically assumed for high-redshift galaxies ($\xi_{\text{ion}} = 25.2$; Robertson et al. 2013). The relations between W and ξ_{ion} provided in Table 3, can be inverted to infer ξ_{ion} from a measurement of W . For convenience, we have refit the average (binned) values of ξ_{ion} as a function of $W([\text{O III}])$ to obtain the following relation:

$$\log \left[\frac{\xi_{\text{ion}}}{\text{Hz erg}^{-1}} \right] = (1.83 \pm 0.31) \times \log \left[\frac{W([\text{O III}])}{\text{\AA}} \right] + (21.96 \pm 0.57). \quad (2)$$

We remind the reader that the relation above is valid for ξ_{ion} values computed using the SMC extinction curve.

4. DISCUSSION

Having presented the relations between equivalent widths and various SED-derived parameters and ISM properties in Section 3, we now turn to a discussion of how the various aforementioned trends arise, and how the equivalent widths evolve with redshift when placing our measurements in context with those of the literature. We also consider practical applications of our results in terms of selecting high-ionization and high-excitation galaxies, and those that may dominate cosmic reionization.

4.1. The Sensitivity of [O III] Equivalent Width to Mass, Metallicity, and SFR

In Section 3.1, we presented evidence that the relationships between equivalent width and stellar mass evolve with redshift, such that galaxies of a fixed M_* have larger W with redshift. This evolution in W at a fixed mass may be associated with the increase in SFR with redshift at a given mass (e.g., Noeske et al. 2007; Reddy et al. 2006; Daddi et al. 2007; Rodighiero et al. 2011; Wuyts et al. 2011; Reddy et al. 2012b; Whitaker et al. 2014; Schreiber et al. 2015), and/or the decrease in metallicity with redshift at a given mass (e.g., Erb et al. 2006a; Maiolino et al. 2008; Troncoso et al. 2014; Sanders et al. 2015; Onodera et al. 2016). The former is indicated by Figure 6, where the higher redshift galaxies are found to have higher average $\text{SFR}[H\alpha]$ and W relative to the local sample. The latter is indicated by Figures 10 and 11, showing that galaxies with lower metallicities have higher equivalent widths.

4.1.1. Calculation of Residuals

To further explore the cause of this evolution, we focused on [O III], and we computed the amount by which each galaxy's $W([\text{O III}])$, $\text{SFR}[H\alpha]$, oxygen abundance,

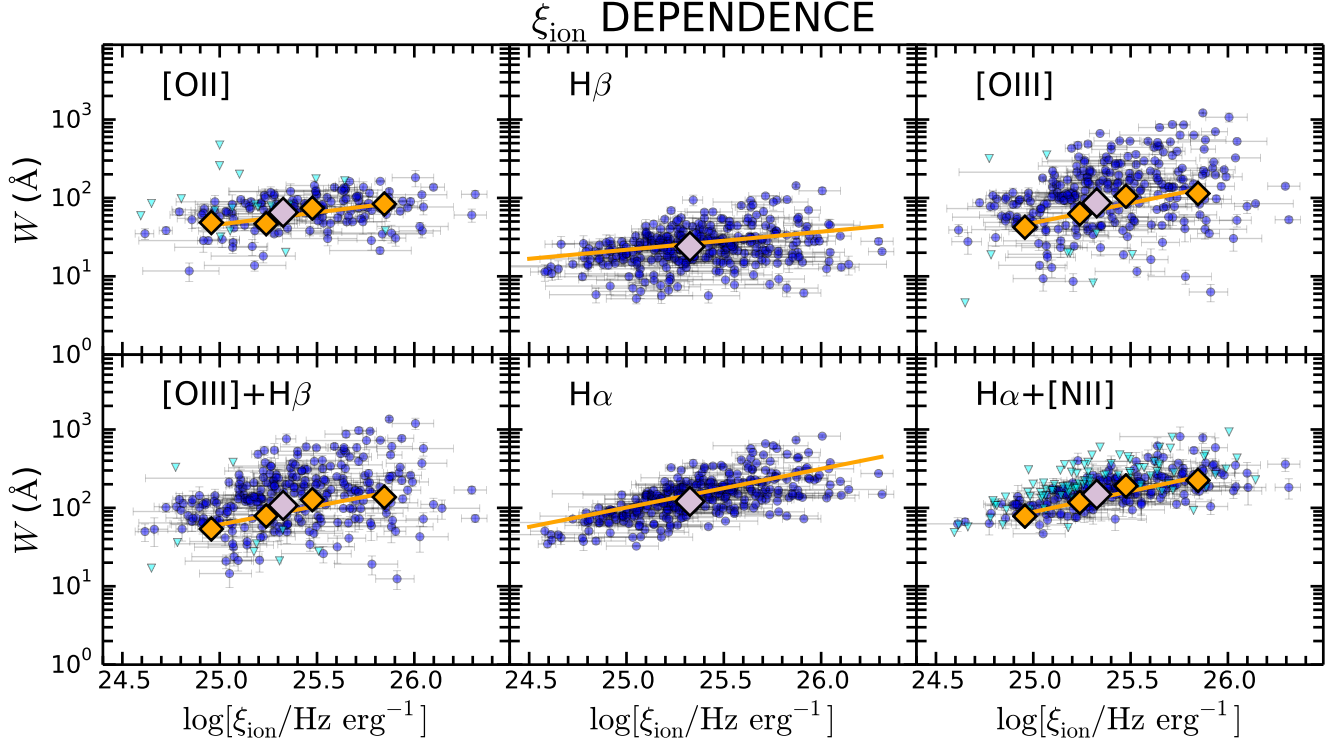


Figure 12. Rest-frame equivalent widths (W) of [O II], H β , [O III], [O III]+H β , H α , and H α + [N II], as a function of the ionizing photon production efficiency, ξ_{ion} . Symbols are the same as in previous figures. As detailed in the text, the values of ξ_{ion} shown here assume the SMC curve when dust-correcting the UV continuum.

and O32 deviates from the mean values of these quantities for galaxies of the same stellar mass. We considered oxygen abundances estimates from N2, as there is a larger number of galaxies with N2-based metallicities than O3N2-based metallicities. O32 is included in this analysis as it is inversely correlated with metallicity, and thus serves as a second proxy for metallicity. We first determined the best-fit linear functions describing the behavior of $\log[M_*/M_\odot]$ with $\log[W/\text{\AA}]$ (e.g., as exemplified in Figure 3), $\log[\text{SFR}[\text{H}\alpha]/M_\odot \text{ yr}^{-1}]$ (i.e., the SFR- M_* relation), $12 + \log(\text{O}/\text{H})_{\text{N2}}$ (i.e., the mass-metallicity relation), and $\log[\text{O32}]$, where all these quantities could be directly measured—i.e., we required direct detections of [O II], [O III], H β , H α , and [N II], leaving a sample of 141 objects. The functional forms of these linear relations are:

$$\log[W([\text{O III}])/\text{\AA}] = 8.41 - 0.64 \log[M_*/M_\odot] \quad (3)$$

$$\log[\text{SFR}[\text{H}\alpha]/M_\odot \text{ yr}^{-1}] = -4.11 + 0.54 \log[M_*/M_\odot] \quad (4)$$

$$12 + \log(\text{O}/\text{H}) = 6.70 + 0.17 \log[M_*/M_\odot] \quad (5)$$

$$\log(\text{O32}) = 3.98 - 0.40 \log[M_*/M_\odot]. \quad (6)$$

We then computed the amount by which each galaxy deviates at a fixed stellar mass from the best-fit relations listed above (i.e., the residuals) in $\log[W([\text{O III}])/\text{\AA}]$, $\log[\text{SFR}[\text{H}\alpha]/M_\odot \text{ yr}^{-1}]$, $12 + \log(\text{O}/\text{H})$, and $\log(\text{O32})$. These residuals are referred to as $\Delta \log[W]$, $\Delta \log[\text{SFR}(\text{H}\alpha)]$, $\Delta[12 + \log(\text{O}/\text{H})]$, and $\Delta \log(\text{O32})$, respectively. Below, we consider how the relationship between the residuals in equivalent width versus residuals in SFR varies in bins of residual metallicity, and how the relationships between the residuals in equivalent width versus residuals in metallicity and O32 vary

in bins of residual SFR (e.g., Figure 14). The residuals allow us to examine how the quantities of interest vary at a given stellar mass in a way that is analogous to the methods employed by Salim et al. (2015), Kashino et al. (2017), and Sanders et al. (2018).

In the context of the present analysis, our goal is to use the residuals as a diagnostic tool to determine whether, at a given mass, $W([\text{O III}])$ is sensitive to SFR, metallicity, or both. For instance, if $W([\text{O III}])$ is primarily sensitive to SFR (and not metallicity) at a given mass, then $\Delta \log[W]$ and $\Delta \log[\text{SFR}(\text{H}\alpha)]$ should be correlated and exhibit no systematic offsets when determined in different bins of metallicity. On the other hand, if $W([\text{O III}])$ is primarily sensitive to metallicity (and not SFR) at a given mass, then $\Delta \log[W]$ and $\Delta \log[\text{SFR}(\text{H}\alpha)]$ should be uncorrelated and the locus of points should shift systematically for galaxies in different bins of metallicity. Similar behaviors will manifest themselves in the relations between $\Delta \log[W]$ and $\Delta[12 + \log(\text{O}/\text{H})]$: if $W([\text{O III}])$ is only sensitive to SFR at a given mass, then $\Delta \log[W]$ and $\Delta[12 + \log(\text{O}/\text{H})]$ should be uncorrelated in different bins of SFR, with the locus of points shifting systematically with SFR; if $W([\text{O III}])$ is only sensitive to metallicity at a given stellar mass, then $\Delta \log[W]$ and $\Delta[12 + \log(\text{O}/\text{H})]$ should be correlated and exhibit no systematic offsets when determined in bins of SFR.

4.1.2. A Physical Context for the Sensitivity of [O III] to SFR and Metallicity

In reality, the equivalent width is sensitive to both SFR and metallicity at a fixed mass. For example, for galaxies of a fixed mass and metallicity, an increase in SFR translates to a larger ionizing photon rate and hence higher [O III] luminosities. For galaxies of a fixed mass and

Table 5
 $\Delta \log[W([\text{O III})/\text{\AA}]]$ Residual Spearman Correlation Tests and Best-fit Parameters

Attribute ^a	Criteria ^b	ρ^c	σ_P^c	Intercept ^d	Slope ^d
$\Delta \log[\text{SFR}(\text{H}\alpha)/M_\odot \text{ yr}^{-1}]$	All	0.55	6.5	0.00 ± 0.02	0.64 ± 0.06
	$\Delta[12 + \log(\text{O}/\text{H})_{\text{N2}}] < -0.1$	0.56	2.8	0.10 ± 0.06	0.62 ± 0.15
	$-0.1 \leq \Delta[12 + \log(\text{O}/\text{H})_{\text{N2}}] < 0.05$	0.26	1.9	0.02 ± 0.03	0.40 ± 0.11
	$\Delta[12 + \log(\text{O}/\text{H})_{\text{N2}}] \geq 0.05$	0.50	3.4	-0.09 ± 0.03	0.47 ± 0.08
$\Delta[12 + \log(\text{O}/\text{H})_{\text{N2}}]$	All	-0.58	6.8	0.00 ± 0.03	-2.95 ± 0.42
	$\Delta[\text{SFR}(\text{H}\alpha)/M_\odot \text{ yr}^{-1}] < -0.4$	-0.57	2.4	-0.07 ± 0.16	-1.98 ± 0.10
	$-0.4 \leq \Delta[\text{SFR}(\text{H}\alpha)/M_\odot \text{ yr}^{-1}] < 0.3$	-0.46	4.4	-0.01 ± 0.05	-2.39 ± 0.35
	$\Delta[\text{SFR}(\text{H}\alpha)/M_\odot \text{ yr}^{-1}] \geq 0.3$	-0.45	2.4	0.09 ± 0.12	-1.47 ± 0.82
$\Delta[\log(\text{O32})]$	All	0.71	8.5	0.00 ± 0.02	1.11 ± 0.07
	$\Delta[\text{SFR}(\text{H}\alpha)/M_\odot \text{ yr}^{-1}] < -0.4$	0.61	2.6	-0.22 ± 0.03	1.09 ± 0.20
	$-0.4 \leq \Delta[\text{SFR}(\text{H}\alpha)/M_\odot \text{ yr}^{-1}] < 0.3$	0.76	7.2	-0.01 ± 0.02	0.88 ± 0.06
	$\Delta[\text{SFR}(\text{H}\alpha)/M_\odot \text{ yr}^{-1}] \geq 0.3$	0.91	4.9	0.18 ± 0.02	1.09 ± 0.09

^a Statistics are presented for the relationship between $\Delta \log[W([\text{O III})/\text{\AA}]]$ and the attribute listed in this column.

^b Criteria used to construct the subsamples.

^c Spearman rank correlation coefficient and the number of standard deviations by which the correlation deviates from the null hypothesis of no correlation.

^d Intercept and slope of the best-fit linear function.

SFR, a lower metallicity implies stellar populations with a harder ionizing spectrum and hence higher [O III] luminosities. The sensitivity of [O III] to gas-phase metallicity, as predicted from Cloudy photoionization modeling (Ferland et al. 2017), is shown in Figure 13. For the modeling, we assumed an open geometry (i.e., constant density slab of gas) with $n_e = 250 \text{ cm}^{-3}$; a range of ionization parameters $\log(\mathcal{U}) = -3.5$ to -1.5 ; and two Starburst99 (Leitherer et al. 1999) stellar population model spectra taken from Sanders et al. (2016a), called “SB99hard” and “SB99soft,” which encompass the range of ionizing spectral shapes relevant for galaxies in our sample. Specifically, the “SB99hard” model assumes a $1/7 Z_\odot$ stellar population formed in a single burst of star formation that occurred 0.5 Myr ago. The “SB99soft” model assumes a solar metallicity stellar population formed with a continuous SFR of $1 M_\odot \text{ yr}^{-1}$. This figure indicates that for metallicities $\gtrsim \frac{1}{3} Z_\odot$, and over the range of metallicities spanned by most of the galaxies in the MOSDEF sample, the [O III] line luminosity at a fixed SFR and stellar mass will increase with decreasing metallicity. Correspondingly, $W([\text{O III}])$ will also increase with decreasing metallicity in this regime at a fixed SFR and stellar mass.

4.1.3. Results for the High-redshift Sample

The expected sensitive of $W([\text{O III}])$ to both SFR and metallicity (at a fixed mass) is borne out by the results of Figure 14, where we show how $\Delta \log[W]$ depends on the other residuals: $\Delta \log[\text{SFR}(\text{H}\alpha)]$, $\Delta[12 + \log(\text{O}/\text{H})]$, and $\Delta \log(\text{O32})$. Focusing on the top panel of this figure (and Table 5), we find that the correlations between $\Delta \log[W]$ and $\Delta \log[\text{SFR}(\text{H}\alpha)]$ in different bins of $\Delta[12 + \log(\text{O}/\text{H})]$ are generally significant at the $\gtrsim 2\sigma$ level. Moreover, the intercept of $\Delta \log[W]$ versus $\Delta \log[\text{SFR}(\text{H}\alpha)]$ increases monotonically from the bin of highest to lowest metallicity. Thus, at a given stellar mass and SFR, the equivalent width increases with decreasing metallicity.

The correlations between $\Delta \log[W]$ and $\Delta \log(\text{O32})$ are also significant, though we note that the scatter between these quantities is tightened artificially as the [O III] line luminosity factors into both $W([\text{O III}])$ and O32. Nevertheless, it is clear from the bottom panel of Figure 14 that the normalization of the relation between

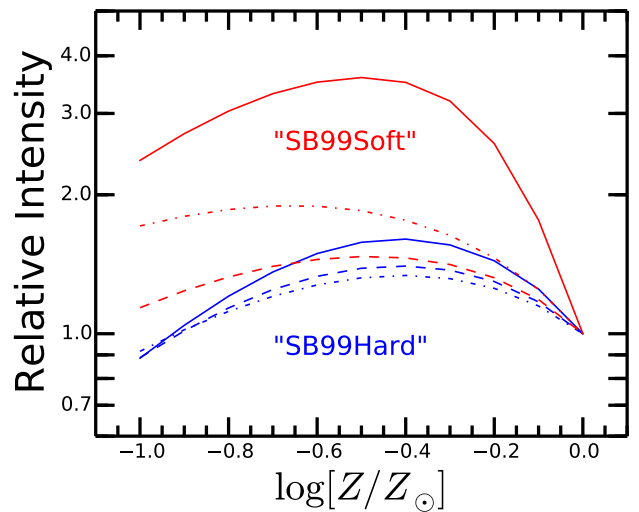


Figure 13. Intensity of the [O III] $\lambda\lambda 4960, 5008$ doublet relative to its solar value as a function of gas-phase metallicity for two stellar population models with different ionizing spectral shapes and $\log(\mathcal{U}) = -3.5, -2.5, -1.5$ (solid, dashed, and dotted-dashed lines, respectively). Curves corresponding to the SBsoft and SBhard models are indicated in red and blue, respectively.

$\Delta \log[W]$ and $\Delta \log(\text{O32})$ increases systematically with $\Delta \log[\text{SFR}(\text{H}\alpha)]$. In the context of the anti-correlation between ionization parameter and metallicity (e.g., Dopita & Evans 1986; Dopita et al. 2006; Pérez-Montero 2014; Sanders et al. 2016b; c.f., Strom et al. 2017), this increase in normalization implies that the equivalent width changes with SFR at a fixed stellar mass and metallicity. This behavior is marginally supported by the $\Delta \log[W]$ versus $\Delta[12 + \log(\text{O}/\text{H})]$ relations, which also increase in normalization with $\Delta \log[\text{SFR}(\text{H}\alpha)]$.

4.1.4. Results for the Local Sample

It is instructive to determine whether the high-redshift residual trends are reflected in the local sample. For the SDSS galaxies, the residuals were computed in a manner similar to those for the high-redshift sample, where we assumed the median relations between stellar mass, SFR, and metallicity in Andrews & Martini (2013), and the median relationship between O32 and stellar mass

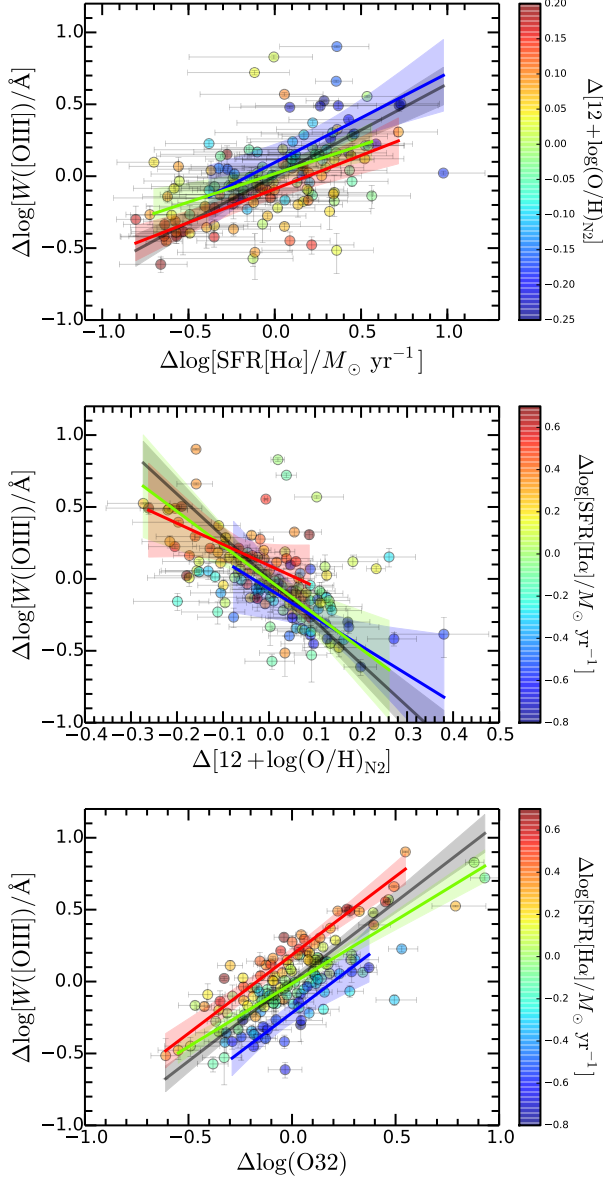


Figure 14. Residuals of equivalent width versus residuals in SFR[H α] (*top*), oxygen abundance inferred from N2 (*middle*), and O32 (*bottom*). The residual is defined as the amount by which a quantity for a galaxy deviates from its mean value expected for galaxies of the same stellar mass. Only the 141 galaxies with significantly detected [O II], [O III], H β , H α , and [N II] lines are shown, such that the same set of galaxies appears in every panel. The gray lines and gray-shaded regions indicate the best-fit linear function and 95% confidence intervals of the fit, respectively, for all galaxies shown. Similarly, the blue, green, and red lines and similarly colored shaded regions show the best-fit linear functions and 95% confidence intervals of the fits when dividing galaxies into different bins of residuals in oxygen abundance and SFR[H α]. Details of the binning, Spearman correlation tests, and best-fit intercepts and slopes are provided in Table 5.

in Sanders et al. (2016b). For the local galaxies, we find significant correlations ($\sigma_P \gtrsim 4$; Figure 15) between $\Delta \log[W]$ and $\Delta \log[\text{SFR}(\text{H}\alpha)]$, $\Delta[12 + \log(\text{O}/\text{H})]$, and $\Delta \log(\text{O}32)$. Moreover, the local sample segregates in the same way as the high-redshift sample, in the sense that the median value of $\Delta \log[W]$ increases with $\Delta[12 + \log(\text{O}/\text{H})]$ at a fixed $\Delta \log[\text{SFR}(\text{H}\alpha)]$, while $\Delta \log[W]$ increases with $\Delta \log[\text{SFR}(\text{H}\alpha)]$ at a fixed $\Delta[12 + \log(\text{O}/\text{H})]$

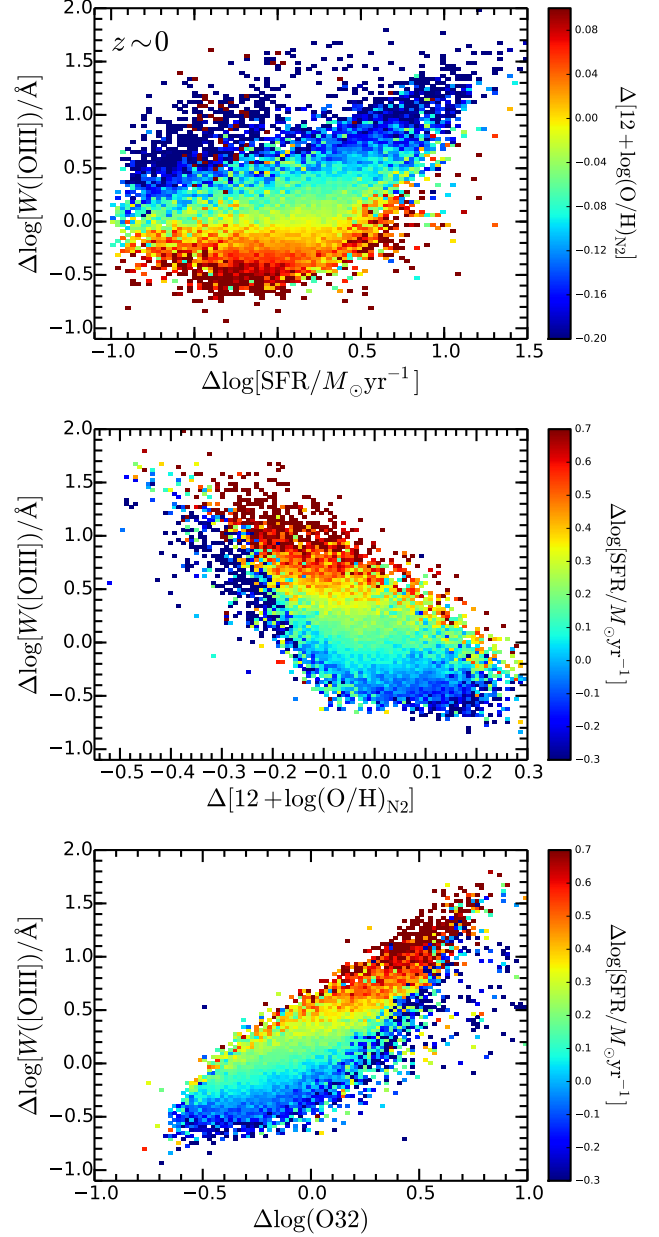


Figure 15. Same as Figure 14 for the $z \sim 0$ SDSS sample. Shown are the residuals in [O III] equivalent width versus the residuals in SFR (*top*), $12 + \log(\text{O}/\text{H})_{\text{N}2}$ (*middle*), and $\log(\text{O}32)$ (*bottom*). The residuals are obtained in a manner similar to that of the MOSDEF sample, where the mean relations between stellar mass, metallicity, and SFR are taken from Andrews & Martini (2013), and the mean relation between O32 and stellar mass is taken from Sanders et al. (2016b). The same trends observed for the $z \sim 2$ MOSDEF sample are also observed locally: galaxies of a fixed sSFR have equivalent widths that increase with decreasing metallicity, galaxies of a fixed metallicity have equivalent widths that increase with SFR, and galaxies of a fixed ionization parameter have equivalent widths that increase with SFR.

or $\Delta \log(\text{O}32)$.

4.1.5. Summary

The residual plots for the high-redshift and local galaxies indicate that the equivalent width of [O III] is sensitive to both the metallicity and SFR at a given stellar mass. A $z \sim 2$ galaxy with $M_* = 10^{10} M_\odot$ has an average $\log[\text{SFR}/M_\odot \text{ yr}^{-1}]$ that is $\simeq 1.0$ dex larger, and

Table 6
UV Slope versus Stellar Mass

Redshift Subsample	ρ^a	σ_P^a	Intercept ^b	Slope ^b
$z \sim 1.5$	0.51	9.6	-8.06 ± 0.42	0.65 ± 0.04
$z \sim 2.3$	0.44	10.7	-9.42 ± 0.39	0.80 ± 0.04
$z \sim 3.4$	0.55	8.7	-9.67 ± 0.57	0.85 ± 0.06

^a Spearman rank correlation coefficient and the number of standard deviations by which the correlation deviates from the null hypothesis of no correlation.

^b Intercept and slope of the best-fit linear function between β and $\log[M_*/M_\odot]$.

a $12 + \log(\text{O}/\text{H})$ that is $\simeq 0.2$ dex lower, than those of a $z \sim 0$ galaxy with the same stellar mass, according to the redshift evolution of the SFR- M_* and MZR relations, respectively. The relations shown in Figure 14 and listed in Table 5 indicate that these changes in SFR and metallicity translate to a $\simeq 0.64$ dex and a $\simeq 0.59$ dex increase, respectively, in $\log[W([\text{O III}])/\text{\AA}]$, for a total increase of $\simeq 0.64 + 0.59 \approx 1.23$ dex. This overall change in equivalent width is entirely consistent with the $\delta \log[W([\text{O III}])/\text{\AA}] \approx 1.3$ dex offset indicated in the evolution of $W([\text{O III}])$ versus M_* with redshift shown the upper rightmost panel of Figure 3. Thus, the redshift evolution in the SFR- M_* and metallicity versus M_* relations is sufficient to explain the increase in $W([\text{O III}])$ with redshift at a fixed stellar mass.

4.2. Trends for Emission Lines Other Than [O III]

The other emission lines of interest are sensitive to SFR and metallicity to varying degrees. For example, not surprisingly, $W(\text{H}\alpha)$ and $W(\text{H}\beta)$ are more sensitive to SFR and less sensitive to metallicity than $W([\text{O III}])$ is at a given stellar mass. As a result, the evolution in the $W(\text{H}\alpha)$ and $W(\text{H}\beta)$ versus M_* relations is not as pronounced as it is for $W([\text{O III}])$ versus M_* , a result noted in Section 3.1. For [O II], we find no significant correlations between the residuals discussed above, a finding that at face value suggests that $W([\text{O II}])$ is not as sensitive as $W([\text{O III}])$ is to either SFR or metallicity for the high-redshift sample. As a consequence, the $W([\text{O II}])$ versus M_* relations among MOSDEF galaxies show markedly less evolution with redshift relative to the $W([\text{O III}])$ versus M_* relations (Figure 3). Nonetheless, when examined over a large enough baseline in redshift or lookback time, $W([\text{O II}])$ is systematically larger for the MOSDEF galaxies relative to local galaxies at a fixed stellar mass (Figure 3).¹⁰

4.3. Other Redshift-dependent Trends

There are several other trends noted in Section 3 that can be explained by the dependence of equivalent width on SFR and metallicity at a given stellar mass. The rest-frame UV slope (β) is sensitive to the reddening, or $E(B-V)_{\text{stars}}$, and there is a monotonic relation between the two for a given intrinsic stellar population and dust attenuation curve. Figure 4 shows that for all of the lines of interest except [O II], the equivalent width increases with redshift at a fixed β , or reddening.

¹⁰ Some of this evolution may be due to the evolving contribution of DIG emission to the [O II] line (e.g., Sanders et al. 2017).

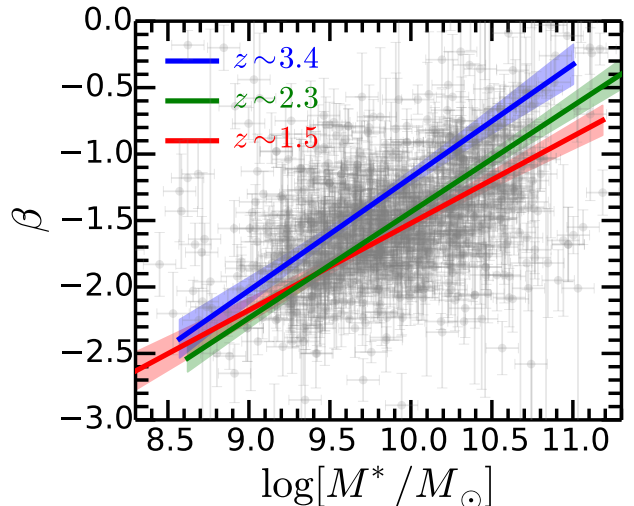


Figure 16. Variation of UV slope, β , with stellar mass for the MOSDEF sample. Spearman tests indicate a high degree of significance ($\sigma_P \gtrsim 10$) in the correlations between β and M_* for the low, middle, and high redshift subsamples. The best-fit linear correlations their 95% confidence intervals are indicated by the red, green, and blue lines and shaded regions for the $z \sim 1.5$, $z \sim 2.3$, and $z \sim 3.4$ subsamples, respectively. The best-fit parameters are listed in Table 6.

The observed redshift evolution of the trends between W and β is a logical outcome of the dependence of UV slope (or reddening) on stellar mass which, for the MOSDEF sample, is shown in Figure 16. A formal fit to the data indicates that β is correlated with M_* with $\gtrsim 8\sigma$ significance for the $z \sim 1.5$, $z \sim 2.3$, and $z \sim 3.4$ subsamples (Table 6). Between the two lower redshift subsamples, galaxies of a given β will on average have roughly the same stellar mass, while there is some indication that galaxies in the highest redshift subsample have stellar masses that are a factor of $2 - 3\times$ lower than those of $z \sim 2$ galaxies at a given β . Or, alternatively, the $z \sim 3.4$ galaxies have β that are on average $\delta\beta \simeq 0.2$ redder than $z \sim 2$ galaxies of the same stellar mass.

At face value, the apparent redshift evolution in the β versus M_* relation runs counter to the conclusions of a number of studies that have suggested that the correlation between stellar mass and dust attenuation—which is directly related to β and is typically parameterized by the ratio of the infrared-to-UV luminosity (IRX; Meurer et al. 1999)—does not evolve with redshift (Pannella et al. 2009; Reddy et al. 2010; Bouwens et al. 2016; Reddy et al. 2018). However, the relationship between IRX and β may evolve with redshift (e.g., Bouwens et al. 2016; Reddy et al. 2018). For example, if higher redshift galaxies follow steeper attenuation curves than lower redshift galaxies of a fixed stellar mass, then the higher redshift galaxies will exhibit redder β for a given IRX (e.g., see Reddy et al. 2018 for further discussion). Thus, an evolution of β with redshift at a fixed stellar mass does not necessarily imply that IRX evolves in the same manner, and in fact, the relation between IRX and stellar mass does not appear to evolve strongly with redshift as noted above.

Viewed in this context of the strong correlation between β and M_* and the fact that the correlation does not evolve strongly with redshift (or, that it evolves toward lower stellar masses at a given β), it follows that

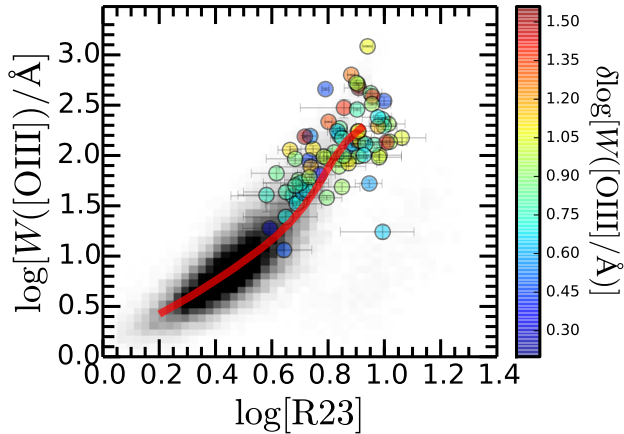


Figure 17. Equivalent width of the [O III] line versus the R23 metallicity index for the 114 galaxies where [O II], H β , [O III], H α , and [N II] are significantly detected, color-coded by their offset in $\log[W([\text{O III})]/\text{\AA}]$ from the median trend of $\log[W([\text{O III})]/\text{\AA}]$ versus $12 + \log(\text{O}/\text{H})_{\text{N2}}$ for local SDSS galaxies (red line in the upper rightmost panel of Figure 10). Also shown is the distribution of R23 for the SDSS sample, corrected for DIG emission and flux-weighting effects (Sanders et al. 2017), with the running median for the local galaxies indicated by the red line.

the increase in W with redshift at a given stellar mass will translate to an increase in W with redshift at a given β , for essentially the same reasons delineated in the previous section.

Finally, a consequence of the redshift evolution in the SFR- M_* relation is that high-redshift galaxies have on average lower stellar masses than local galaxies at a fixed SFR. Therefore, the increasing normalization of the W versus SFR relation with redshift (e.g., Figure 6) reflects the trend of higher equivalent widths at lower stellar masses and higher redshifts, precisely the behavior shown in Figure 3.

4.4. Redshift Evolution in the Trends between Equivalent Width and ISM Physical Conditions

4.4.1. Equivalent Width versus Metallicity

We can use similar lines of reasoning as those invoked above to explain the redshift evolution in the relationship between equivalent width and oxygen abundance, at least as determined through nitrogen lines (Figures 10 and 11). An outcome of the redshift evolution in the MZR (Sanders et al. 2018) is that galaxies of a fixed N2-inferred (or O3N2-inferred) oxygen abundance of $12 + \log(\text{O}/\text{H}) = 8.45$ —roughly the mean abundance for the $z \sim 2$ sample—have an average $\log[M_*/M_\odot]$ that is ≈ 1 dex larger than that of $z \sim 0$ galaxies. On the other hand, such galaxies at $z \sim 2$ have SFRs that are *two* orders of magnitude larger than those of $z \sim 0$ galaxies at the same metallicity. Thus, the stellar mass increases with redshift by a modest amount relative to the SFR at a fixed (N2-based) metallicity, resulting in an overall increase in sSFR of ≈ 1 dex with redshift. According to the relations listed in Table 8 for $\log[\text{sSFR}[\text{H}\alpha]/\text{yr}^{-1}]$, this increase in sSFR results in an ≈ 0.5 dex increase in $\log[W([\text{O III})]/\text{\AA}]$, similar to the difference in $\log[W([\text{O III})]/\text{\AA}]$ between $z \sim 2$ and $z \sim 0$ galaxies for a fixed oxygen abundance of $12 + \log(\text{O}/\text{H})_{\text{N2}} = 8.45$ (Figure 10).

Several studies have found that high-redshift galaxies

exhibit larger N2 ratios at a given oxygen abundance and/or are offset toward higher N2 in the BPT plane (Kewley et al. 2013; Masters et al. 2014; Steidel et al. 2014; Shapley et al. 2015; Sanders et al. 2016b). Various possible explanations have been given for this offset, including elevated nitrogen abundances at a fixed oxygen abundance (Masters et al. 2014; Shapley et al. 2015), or differences in ISM conditions, including gas pressure (Kewley et al. 2013) or ionization parameter (Steidel et al. 2014), and/or differences in stellar populations (Masters et al. 2014; Steidel et al. 2014). Thus, metallicity estimates based on N2 may be biased to higher values than metallicities computed using other strong lines for galaxies of a fixed ionizing spectrum (e.g., Steidel et al. 2016). We find some indication of this metallicity bias in our analysis. For example, we find that the trend between $W([\text{O III})]$ and $12 + \log(\text{O}/\text{H})_{\text{O3N2}}$ evolves less strongly with redshift than the trend between $W([\text{O III})]$ and $12 + \log(\text{O}/\text{H})_{\text{N2}}$, a difference that may be related to the fact that the O3N2 index is less sensitive to the nitrogen lines than N2. In view of the N2-based metallicity offsets, it is useful to examine whether the offsets in W at a given N2- or O3N2-inferred oxygen abundance between high- and low-redshift galaxies persist when using abundance indicators that do not involve nitrogen lines.

To this end, we calculated the R23 values for the local SDSS galaxies as well as the 114 MOSDEF galaxies with direct detections of the lines used in calculating this index—i.e., [O II], [O III], H β , and H α (H α is required in addition to H β in order to correct the lines for dust attenuation based on the Balmer decrement)—as well as detections of [N II] (i.e., to ensure that the galaxies have measured N2 values). As noted previously, the line ratios (including R23) were corrected for the effects of DIG emission and flux weighting using the prescriptions of Sanders et al. (2017). As discussed in Shapley et al. (2015) (see also Sanders et al. 2016b), galaxies follow a monotonic increase in metallicity proceeding from high O32 and R23 values to low O32 and R23 values (e.g., Sanders et al. 2016b). From Figure 8, we see that $W([\text{O III})]$ correlates tightly with O32 (Figure 8). It then follows that there will be a similar monotonic increase in metallicity as $W([\text{O III})]$ and R23 decrease in tandem.

Figure 17 shows that the $z \sim 2$ galaxies mostly follow the local relationship between $\log[W([\text{O III})]$ and R23. In particular, we find that those $z \sim 2$ galaxies that exhibit the largest offsets in their [O III] equivalent widths relative to local SDSS galaxies at the same $12 + \log(\text{O}/\text{H})_{\text{N2}}$ scatter around the median trend of $\log[W([\text{O III})]/\text{\AA}]$ versus $\log[\text{R23}]$ for $z \sim 0$ galaxies.¹¹ In summary, our results suggest that, when using metallicity indicators that do not depend on nitrogen lines, the relationship between equivalent width and metallicity at

¹¹ If the line ratios of the SDSS galaxies are not corrected for DIG emission and flux weighting, the relationship between $\log[W([\text{O III})]$ and $\log[\text{R23}]$ for the local sample would be shifted by ≈ 0.1 dex to larger $\log[\text{R23}]$. In this case of no correction, we find that at a fixed $\log[\text{R23}] = 0.8$, corresponding roughly to $12 + \log(\text{O}/\text{H})_{\text{R23}} \approx 8.5$, galaxies at $z \sim 2$ have an average $\log[W([\text{O III})]$ that is ≈ 0.3 dex larger than that of local galaxies. This offset is smaller than the ≈ 0.6 dex offset between $W([\text{O III})]$ versus $12 + \log(\text{O}/\text{H})_{\text{N2}}$ at a similar oxygen abundance, implying a smaller degree of redshift evolution in $W([\text{O III})]$ versus $12 + \log(\text{O}/\text{H})_{\text{R23}}$ relative to the redshift evolution in $W([\text{O III})]$ versus $12 + \log(\text{O}/\text{H})_{\text{N2}}$.

$z \sim 2$ is similar to that seen at $z \sim 0$, or at the least, does not evolve with redshift as strongly as that observed when using N2-based metallicities. Further evidence supporting this conclusion is provided by an analysis of the relationship between W and O3, as the latter is also sensitive to metallicity (see next section).

On a note of caution, the sensitivity of the R23 index to metallicity is limited over the range of metallicities represented in the MOSDEF sample, as it is for this range that the R23 index effectively saturates. Going forward, robust calibrations of strong-line metallicity indicators—such as those obtained through [O III] λ 4364 auroral line measurements of electron temperatures—will be crucial for robustly quantifying some of the redshift offsets in W versus metallicity discussed here. We note that the aforementioned bias in N2-based metallicities does not affect our analysis of the correlations between residuals in equivalent width, metallicity, and SFR presented in Section 4.1, since these correlations are examined in a relative sense at a fixed redshift (e.g., Sanders et al. 2018).

4.4.2. Equivalent Width versus Excitation Conditions

A primary conclusion of Section 4.1 is that the equivalent width of [O III] is sensitive to both SFR and metallicity at a given stellar mass. Here, we focus on the extent to which the sensitivity of W to SFR and metallicity translates to the observed behavior of W versus O32 and O3. Specifically, the anti-correlation between ionization parameter and metallicity implies that the redshift invariance of the W versus R23-based-metallicity relation (Figure 17) should translate to a similar redshift invariance of the W versus O32 relation if we assume that the O32 versus R23 relation does not evolve with redshift. However, this expected behavior is not observed in Figure 8. Rather, we observe some mild redshift evolution in the W versus O32 relation. The redshift evolution in W ([O III]) versus O32 and the apparent redshift invariance of W ([O III]) versus R23 implies that the O32 versus R23 relation evolves with redshift, as shown in Figure 18. Interestingly, if we do not correct the SDSS galaxies for DIG emission and flux-weighting effects, the resulting relation between $\log[W(\text{[O III]})]$ and $\log[\text{O32}]$ for the local sample provides an adequate description of this same relation for the $z \sim 2$ galaxies.

On the other hand, the O3 ratio—sensitive to both ionization parameter and metallicity—is not as significantly affected by DIG emission and flux-weighting effects as O32. Indeed, for local galaxies, the O3 ratio is biased < 0.1 dex over the range of excitation and metallicity displayed by the majority of $z \sim 0$ SDSS galaxies (Sanders et al. 2017). We find that the $\log[W(\text{[O III]})]$ versus $\log[\text{O3}]$ relation does not evolve significantly, on average, between the low- and high-redshift samples (Figure 9). This fact, combined with the observation that the $\log[W(\text{[O III]})]$ versus $12 + \log(\text{O}/\text{H})_{\text{O3N2}}$ does not evolve with redshift as strongly as the $\log[W(\text{[O III]})]$ versus $12 + \log(\text{O}/\text{H})_{\text{N2}}$ relation, suggests that the observed redshift evolution in the latter (i.e., $\log[W(\text{[O III]})]$ versus $12 + \log(\text{O}/\text{H})_{\text{N2}}$) results from a systematic bias in the nitrogen-based metallicity indicators at high redshift. A full analysis of the relationships between O32, O3, and metallicity, and how these relations are affected by DIG, flux-weighting effects, and shock emission, is beyond the scope of this paper and will be presented else-

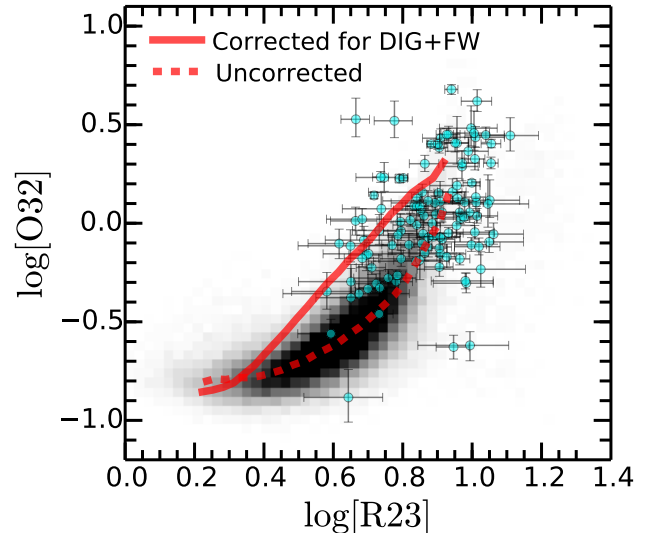


Figure 18. Relationship between $\log[\text{O32}]$ and $\log[\text{R23}]$ for the $z \sim 2$ MOSDEF galaxies, shown by the cyan circles. For comparison, we also show the median relationship for SDSS galaxies when correcting both $\log[\text{O32}]$ and $\log[\text{R23}]$ for DIG emission and flux-weighting effects using the prescriptions of Sanders et al. (2017) (solid line). The grayscale distribution shows $\log[\text{O32}]$ versus $\log[\text{R23}]$, with the median relation indicated by the dashed line, when leaving these quantities uncorrected for DIG emission and flux-weighting effects. A full discussion of how the inferred redshift evolution in O32 versus R23 depends on corrections made to these ratios for DIG emission and flux-weighting effects will be discussed elsewhere (Shapley et al. 2018, in preparation).

where (Shapley et al. 2018, in preparation). Nonetheless, at face value, our results suggest a redshift invariance in both $\log[W(\text{[O III]})]$ versus $\log[\text{R23}]$ and $\log[W(\text{[O III]})]$ versus $\log[\text{O3}]$, implying that the metallicity plays a fundamental role in modulating the [O III] equivalent width. This conclusion is in accordance with expectations that lower stellar metallicities result in a harder ionizing spectrum and hence larger [O III] equivalent widths when keeping both stellar mass and SFR fixed (e.g., Figure 13). As noted in Section 4.1, SFR and stellar mass are additional variables that will affect the equivalent widths, an issue that we discuss further in the next section.

4.5. Redshift Invariant Trends with $s\text{SFR}$ and Age

4.5.1. Redshift Invariance of W versus $s\text{SFR}$ at $1.5 \lesssim z \lesssim 4$

As noted in Section 3, the equivalent width depends on those properties that are sensitive to spectral shape, or mass-to-light ratio, such as $s\text{SFR}$ and age. Furthermore, the relationship between equivalent width and $s\text{SFR}$ or age for high-redshift galaxies is similar to that seen for local galaxies. The redshift invariance of the W versus $s\text{SFR}$ relationship persists at even higher redshifts. Based on simultaneous fitting of the stellar and nebular continuum and nebular line emission in a sample of $z \sim 4$ galaxies, Schaerer et al. (2013) derived relationships between $s\text{SFR}$ and the equivalent widths of both $\text{H}\alpha$ and [O II] for a number of different star formation histories. As shown in Figure 19, the relationships between equivalent width and $s\text{SFR}$ derived for a constant star-formation history for the $z \sim 4$ galaxies are consistent with the mean trends found for galaxies at $z \sim 1.5$ and $z \sim 2.3$ from the MOSDEF sample.

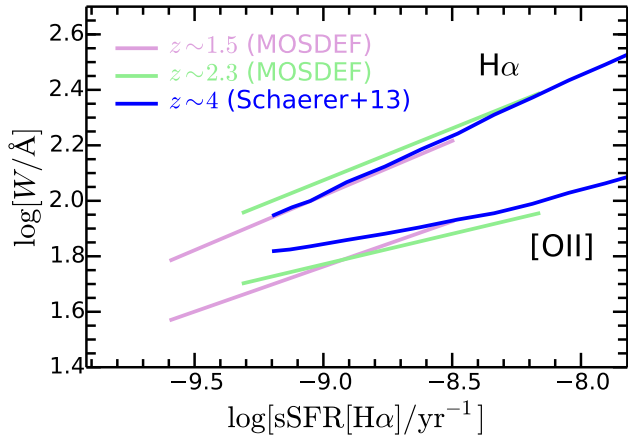


Figure 19. Average trends of $H\alpha$ and $[O II]$ equivalent widths versus $sSFR[H\alpha]$ for galaxies in the two lower redshift bins of the MOSDEF sample ($z \sim 1.5$ and $z \sim 2.3$) and the $z \sim 4$ B -dropout sample analyzed by Schaerer et al. (2013). The dispersion of objects around these average trends is typically of order $\simeq 0.2$ dex.

4.5.2. W versus $sSFR$ at a Fixed Metallicity

It is of interest to examine in more detail how the relationship between equivalent width and $sSFR$ segregates by metallicity. In particular, the equivalent width is sensitive to both line luminosity and continuum luminosity density. Hence, W is, not surprisingly, correlated with both SFR and stellar mass, as shown previously. However, the equivalent width (e.g., of $[O III]$), and in particular the line luminosity, is also sensitive to metallicity, as demonstrated in Figure 14. Figure 20 shows how $z \sim 0$ and $z \sim 2$ galaxies segregate by metallicity in $[O III]$ equivalent width versus $sSFR$ space.

In both the low- and high-redshift samples, there is a monotonic decrease in metallicity with both increasing $sSFR$ and equivalent width. Also shown in the right panel of Figure 20 are the median trends of equivalent width versus $sSFR$ for galaxies in three bins of oxygen abundance for the high redshift sample (dashed lines) and the SDSS sample (solid lines).¹² In comparing the local and high-redshift samples, we find that the median trends of equivalent width with $sSFR$ for the two lower bins of oxygen abundance for the $z \sim 0$ galaxies are roughly within a factor of two of the best-fit linear trends between these quantities in the same bins of oxygen abundance for the $z \sim 2$ galaxies. There is a more significant ($\simeq 0.3 - 0.5$ dex) offset in $\log[W([O III])]$ versus $\log[sSFR[H\alpha]]$ for the bin of highest metallicity. This offset could plausibly be explained by an enhanced nitrogen abundance in high-redshift galaxies relative to local ones at a fixed oxygen abundance. Specifically, Figure 10 shows that the largest offset between the high-redshift and local trends between $\log[W([O III])]$ and $12 + \log(O/H)_{N2}$ occurs for galaxies at higher metallicities. However, taking into consideration the apparent redshift invariance of the relationship between $\log[W([O III])]$ and $12 + \log(O/H)$, where the latter is de-

¹² Note that the slopes of the median trends of equivalent width versus $sSFR$ for galaxies in different bins of metallicity depend on the widths of the bins: the slopes decrease in magnitude with decreasing bin width. The sensitivity of these slopes to bin width applies to both the $z \sim 0$ and $z \sim 2$ trends, such that the relative comparison of the low- and high-redshift slopes remains valid.

termined from lines other than nitrogen (Section 4.4.1), we find that the high-redshift galaxies segregate with metallicity in $\log[W([O III])]$ versus $12 + \log(O/H)$ space in the same way as seen for local galaxies. In other words, at a fixed $sSFR$ and metallicity, $z \sim 2$ galaxies have $[O III]$ equivalent widths that are within a factor of two of those of $z \sim 0$ galaxies.

We also note that the W versus $sSFR$ relationship appears to separate with metallicity at $z \gtrsim 3$ in the same way as seen for $z \sim 2$ galaxies. For instance, COSMOS-1908—one of the galaxies in the MOSDEF survey for which the auroral line $[O III]\lambda 4364$ is detected—has a redshift of $z = 3.08$, a direct electron temperature based metallicity of $12 + \log(O/H) = 8.00$, and $W([O III]) \simeq 2140 \text{ \AA}$ (Sanders et al. 2016a). This object’s $sSFR$ ($\simeq 2.3 \times 10^{-8} \text{ yr}^{-1}$) places it in the same region of the $W([O III])$ versus $sSFR$ relation as lower redshift ($z \sim 2$) galaxies of the same metallicity (Figure 20). Figure 21 shows the relationship between $W(H\alpha)$ and $sSFR[H\alpha]$ for the MOSDEF sample, again color-coded by $N2$ -based metallicities. There is a single galaxy for which a nebular oxygen abundance has been derived at $z \gtrsim 4$, namely, GOODS-N-17940, also from the MOSDEF survey. Using the excess emission in the *Spitzer*/IRAC $3.6 \mu\text{m}$ band relative to the surrounding photometry for this object, Shapley et al. (2017) derived an $H\alpha$ (rest-frame) equivalent width of $W(H\alpha) \simeq 1200 \text{ \AA}$ and a $sSFR[H\alpha] \simeq 9.67 \times 10^{-9} \text{ yr}^{-1}$.¹³ Based on spectroscopic detections of $[O II]$ and $[Ne III]$, Shapley et al. (2017) derived an oxygen abundance of $12 + \log(O/H) \simeq 8.00$, again placing this object in approximately the same region of the $W(H\alpha)$ - $sSFR[H\alpha]$ parameter space occupied by lower redshift objects of the same metallicity.

4.5.3. Summary

Based on the relationships between equivalent width and $sSFR$ for local galaxies, $z \sim 2$ galaxies from the MOSDEF sample, two galaxies with metallicity determinations at $z \gtrsim 3$, and the $z \sim 4$ galaxies analyzed by Schaerer et al. (2013), we conclude that the W versus $sSFR$ relation is largely invariant with redshift, particularly when considering galaxies of the same metallicity. This conclusion is supported by the residual analysis presented previously, which indicates that the line equivalent width is approximately fixed for a given $sSFR$ and metallicity.

Finally, the tight relationship between equivalent width and $sSFR$ at a given metallicity implies a similarly tight relationship between equivalent width and mass-to-light (M/L) ratio. For the constant star-formation history assumed in our analysis, the age of the stellar population is directly related to M/L , modulo the effects of dust. As a consequence, the equivalent width correlates with age in a manner that is independent of the redshifts of the galaxies, as discussed in Section 3.3.

4.6. Redshift Evolution of Equivalent Widths

¹³ The $H\alpha$ -based $sSFR$ was derived by assuming a conversion from $L(H\alpha)$ to $SFR[H\alpha]$ consistent with that of our fiducial model, and assuming the Balmer decrement measured from the $H\gamma$ and $H\delta$ lines to correct for dust. Similarly, the stellar mass was computed assuming our fiducial model.

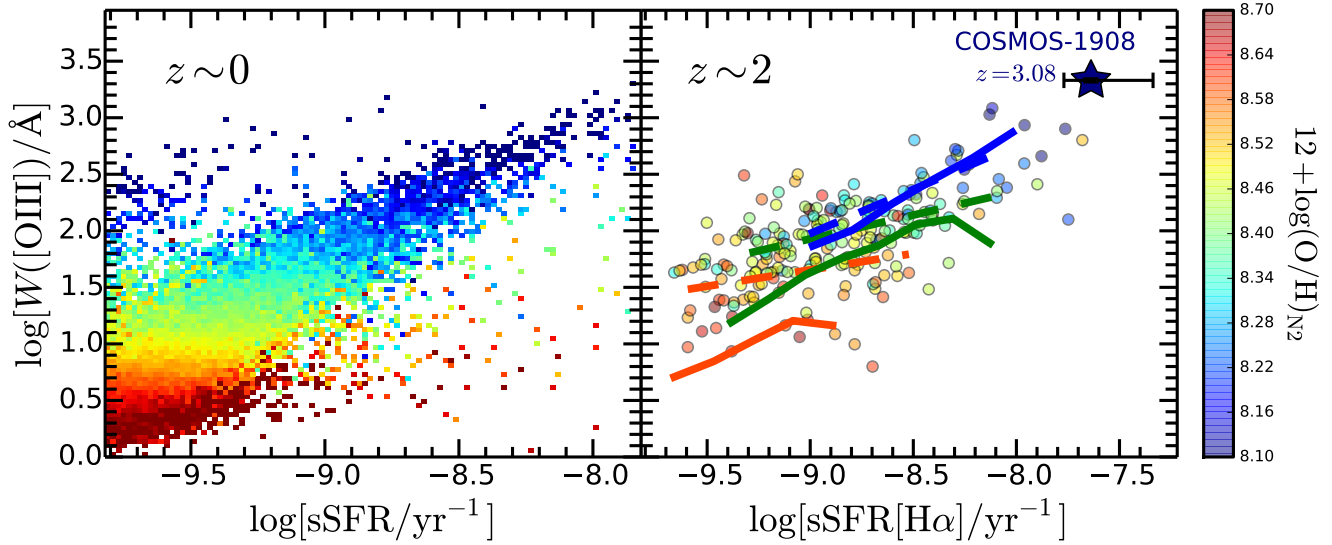


Figure 20. *Left:* relationship between $\log[W([\text{O III})]/\text{\AA}]$ and $\log[\text{sSFR}/\text{yr}^{-1}]$ for $z \sim 0$ galaxies from the SDSS, color-coded by N2-inferred oxygen abundance. *Right:* same as the left panel, for the $z \sim 2$ galaxies. The solid lines indicate the median trend of $\log[W([\text{O III})]/\text{\AA}]$ with $\log[\text{sSFR}/\text{yr}^{-1}]$ for SDSS galaxies in three bins of oxygen abundance: $12 + \log[\text{O}/\text{H}] < 8.26$, $8.26 \leq 12 + \log[\text{O}/\text{H}] < 8.49$, and $12 + \log[\text{O}/\text{H}] \geq 8.49$. The dashed lines show the best-fit linear relations between $\log[W([\text{O III})]/\text{\AA}]$ and $\log[\text{sSFR}/\text{yr}^{-1}]$ for the $z \sim 2$ galaxies in the same bins of oxygen abundance specified above. The large star shows the position of the $z = 3.08$ galaxy, COSMOS-1908, with a direct electron temperature-based metallicity from Sanders et al. (2016a).

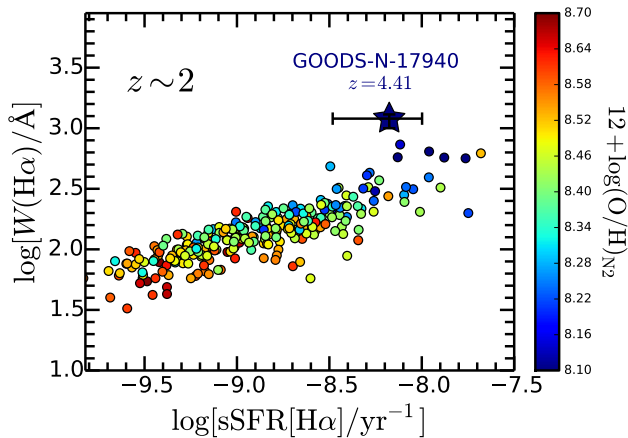


Figure 21. Same as the right panel of Figure 20 for $\log[W(\text{H}\alpha)/\text{\AA}]$ versus $\log[\text{sSFR}[\text{H}\alpha]]$, again color-coded by N2-inferred oxygen abundance. For clarity, the median trends for the $z \sim 0$ and $z \sim 2$ samples are not shown. The single galaxy for which a nebular oxygen abundance has been measured at $z \gtrsim 4$ (Shapley et al. 2017) is shown by the large star.

4.6.1. $W([\text{O III}])$ versus M_*

The tight correlation between rest-frame optical emission line equivalent widths and sSFR (e.g., Figures 7, 20, and 21), and the fact that the former do not depend sensitively on model assumptions, have prompted the use of equivalent width measurements to infer the redshift evolution in the sSFR of galaxies, giving insights into the typical star-formation histories of such galaxies (e.g., Papovich et al. 2011; Reddy et al. 2012b; González et al. 2012; Bouwens et al. 2012; Stark et al. 2013; González et al. 2014; Smit et al. 2014, 2016; Faisst et al. 2016). In this context, we compare the [O III] equivalent width measurements from the MOSDEF survey with others from a subset of the literature at similar (and lower) redshifts in Figure 22. Note that some of these studies

were based on samples that targeted preferentially those galaxies with large equivalent widths (Cardamone et al. 2009; van der Wel et al. 2011; Maseda et al. 2014) or required the detection of the [O III] λ 4364 auroral line (Ly et al. 2015). The latter will tend to select those galaxies with the lowest metallicities and brightest [O III] lines. As such, the relationships between equivalent width and stellar mass derived in these studies may not be reflective of the relationships for all star-forming galaxies at the same redshifts. Not shown in Figure 22 are combined [O III] + H β equivalent widths derived either from narrowband-selected galaxies at $z \simeq 0.8 - 3.3$ (e.g., Khosrovani et al. 2016) or from IRAC color excesses for galaxies at $z \sim 6 - 8$ (e.g., Labbé et al. 2013; Smit et al. 2014; Castellano et al. 2017), but these studies generally point to rest-frame $W([\text{O III}] + \text{H}\beta) \simeq 500 - 3000 \text{\AA}$.

Regardless, when taking our results in context with those of other investigations that targeted lower mass galaxies, we find some hint that the $W([\text{O III}])$ -versus- M_* relation may flatten at $M_* \lesssim 10^{8.7} M_\odot$, with an absence of star-forming galaxies having rest-frame $W([\text{O III}]) \gtrsim 3000 \text{\AA}$. This upper limit appears to be consistent with the typical range of [O III] rest-frame equivalent widths of extreme emission line star-forming galaxies found from other studies at both low and high redshifts (e.g., Atek et al. 2011; van der Wel et al. 2011; Maseda et al. 2014; Smit et al. 2014, 2016; Forrest et al. 2017; Tang et al. 2018).

While the lower redshift emission line samples of van der Wel et al. (2011) and Maseda et al. (2014) are unlikely to have missed a large population of even more extreme emitters (i.e., $W([\text{O III}]) \gtrsim 3000 \text{\AA}$) at the same redshifts, such emitters could be present at even higher redshifts ($z \gtrsim 4$) given the aforementioned evolution toward higher $W([\text{O III}])$ with redshift at a fixed stellar mass (Section 4.1). Thus, the apparent scarcity of galaxies with rest-frame $W([\text{O III}]) \gtrsim 3000 \text{\AA}$ may sim-

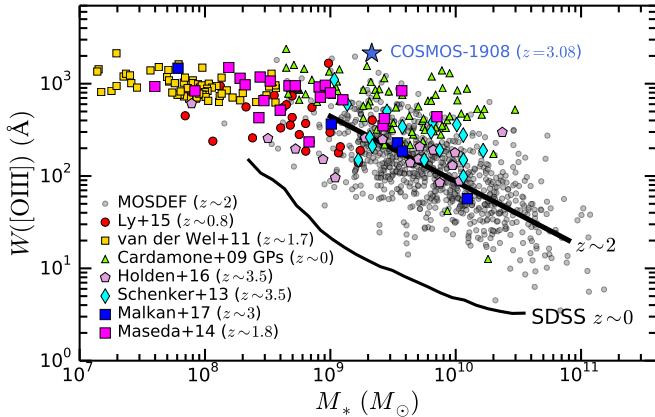


Figure 22. Rest-frame equivalent width of the $[\text{O III}]\lambda\lambda 4960, 5008$ doublet versus stellar mass from MOSDEF (excluding upper limits in $W([\text{O III}])$, for clarity), compared with values from the literature at lower and similar redshifts. These include the $[\text{O III}]\lambda 4364$ -detected sample from Ly et al. (2015), extreme emission line galaxy samples of van der Wel et al. (2011) and Maseda et al. (2014), the Green Peas sample of Cardamone et al. (2009), and the LBG-selected samples of Schenker et al. (2013), Holden et al. (2016), and Malkan et al. (2017). Also shown is COSMOS-1908 from Sanders et al. (2016a). For those studies that included only the 5008 Å line, the equivalent widths were multiplied by a factor of 1.34 to account for the 4960 Å emission line. The thick and thin solid lines indicate the average relationships between $W([\text{O III}])$ and stellar mass for MOSDEF galaxies (including those with upper limits in $W([\text{O III}])$) and SDSS galaxies, respectively.

ply reflect the current absence of line measurements for such objects at $z \gtrsim 4$. With the exception of a few individual galaxies, inferences of line equivalent widths at these redshifts are presently limited to galaxies with $M_* \gtrsim 10^{8.5} M_\odot$ (e.g., Labbé et al. 2013; Smit et al. 2014; Castellano et al. 2017). These studies suggest $[\text{O III}]$ equivalent widths that are consistent with those of the highest equivalent width galaxies in the $z \sim 2$ MOSDEF sample. We must keep in mind, however, that the equivalent widths inferred for $z \sim 6 - 8$ studies are based on stacking photometry, a procedure that can potentially mask the presence of individual strong line emitters.

Alternatively, the plateau in the relationship between $W([\text{O III}])$ and M_* at low masses ($M_* \lesssim 10^9 M_\odot$) may be physical in nature. The prompt enrichment of α elements such as oxygen implies that a “floor” in gas-phase metallicity, and hence stellar metallicity, may be reached over very short (less than tens of Myr) timescales.¹⁴ Given the decrease in the ionizing photon production rate and softening of the ionizing spectrum with increasing stellar metallicity, one might naturally also expect a “ceiling” in the $[\text{O III}]$ equivalent widths for such low-mass galaxies. Another possibility is that the MZR would predict such galaxies to have very low metallicities ($\lesssim 0.2Z_\odot$) such that the collisional line luminosities may be suppressed due to a low oxygen abundance.¹⁵ Indeed, Fig-

¹⁴ Given the apparent α -enhancement present in high-redshift galaxies (Steidel et al. 2016), the actual *measured* stellar metallicity may lag the *measured* gas-phase metallicity, since the former is modulated by iron-peak elements, while the latter is sensitive to α elements (i.e., oxygen).

¹⁵ The critical density for $[\text{O III}]$ is ≈ 3.5 orders of magnitude larger than the typical n_e of $z \sim 2$ galaxies (e.g., Sanders et al. 2016a; Strom et al. 2017), so collisional de-excitation is unlikely to be responsible for the suppression of the $[\text{O III}]$ doublet emission

ure 13 shows that the $[\text{O III}]$ line intensity at a fixed SFR reaches a maximum around $\frac{1}{3}Z_\odot$, below which point the $[\text{O III}]$ line intensity decreases. This non-monotonic behavior in $L([\text{O III}])$ versus Z would translate to a change in slope of the $W([\text{O III}])$ versus M_* relation around a stellar mass of $\approx 10^9 M_\odot$, similar to the behavior seen in Figure 22. It is also possible that the stochastic star formation believed to be present in these low-mass galaxies (Weisz et al. 2012; Hopkins et al. 2014; Domínguez et al. 2015; Guo et al. 2016; Sparre et al. 2017; Faucher-Giguère 2018) may result in the efficient expulsion of metals via supernovae (SNe) and stellar feedback. This effect results in a decrease of the gas-phase metallicity and potential reduction in the strengths of oxygen lines. Future spectroscopic campaigns to measure the oxygen (and other metal and H I recombination) lines in low-mass galaxies at high redshift may be able to distinguish between these various possibilities.

4.6.2. Redshift Evolution in W at a Fixed Mass

For another view of the redshift evolution in equivalent widths, and one that can be used to more directly infer the redshift evolution of the sSFRs and ionization parameters of galaxies, we show in Figure 23 the average $[\text{O III}] + \text{H}\beta$, $[\text{O II}]$, and $\text{H}\alpha$ equivalent widths of $M_* = 10^{9.5} - 10^{10.0} M_\odot$ galaxies as a function of redshift.¹⁶ We include data from the MOSDEF sample analyzed here, as well as several other results from the literature (Thomas et al. 2013; Lamareille et al. 2009; Khostovan et al. 2016; Schenker et al. 2013; Malkan et al. 2017; Smit et al. 2015; Labbé et al. 2013; Adams et al. 2011; Sobral et al. 2014; Faisst et al. 2016; Mármol-Queraltó et al. 2016). Focusing on the top panel, we find that the average $W([\text{O III}] + \text{H}\beta)$ for the redshift subsamples of the MOSDEF survey are consistent with previous measurements at similar redshifts (e.g., Schenker et al. 2013; Khostovan et al. 2016; Malkan et al. 2017). Moreover, we find that the average equivalent widths deduced for the MOSDEF sample are consistent with the double power-law fit to $W([\text{O III}] + \text{H}\beta)$ versus $1 + z$ that includes data at both lower ($z \lesssim 1$) and higher ($z \gtrsim 5$) redshifts provided in Khostovan et al. (2016). This fit—which does not include the MOSDEF galaxies but is nonetheless consistent with our data—indicates that the $[\text{O III}] + \text{H}\beta$ equivalent widths do not continually increase with redshift, but reach a plateau consistent with the absence of very high $[\text{O III}]$ equivalent width galaxies ($W([\text{O III}]) \gtrsim 3000 \text{ \AA}$) as suggested by Figure 22.

The average $W([\text{O II}])$ for galaxies with similar stellar masses also increases with redshift, at least up to $z \sim 2$. While Khostovan et al. (2016) found that $W([\text{O II}])$ continues to increase up to $z \sim 3$, the MOSDEF data suggest an average $W([\text{O II}])$ at $z \sim 3$ that is similar to that measured at $z \sim 2$. There are a few possible reasons for this difference in the inferred redshift evolution of $W([\text{O II}])$. During the course of the MOSDEF survey,

at low stellar masses.

¹⁶ The redshift evolution in equivalent widths shown in Figure 23 should not be interpreted as indicating an evolution in equivalent widths for individual galaxies since, for example, $M_* = 10^{9.5} M_\odot$ galaxies in the local Universe had progenitors at $z \sim 2$ that were significantly less massive than the $M_* = 10^{9.5} M_\odot$ galaxies at $z \sim 2$.

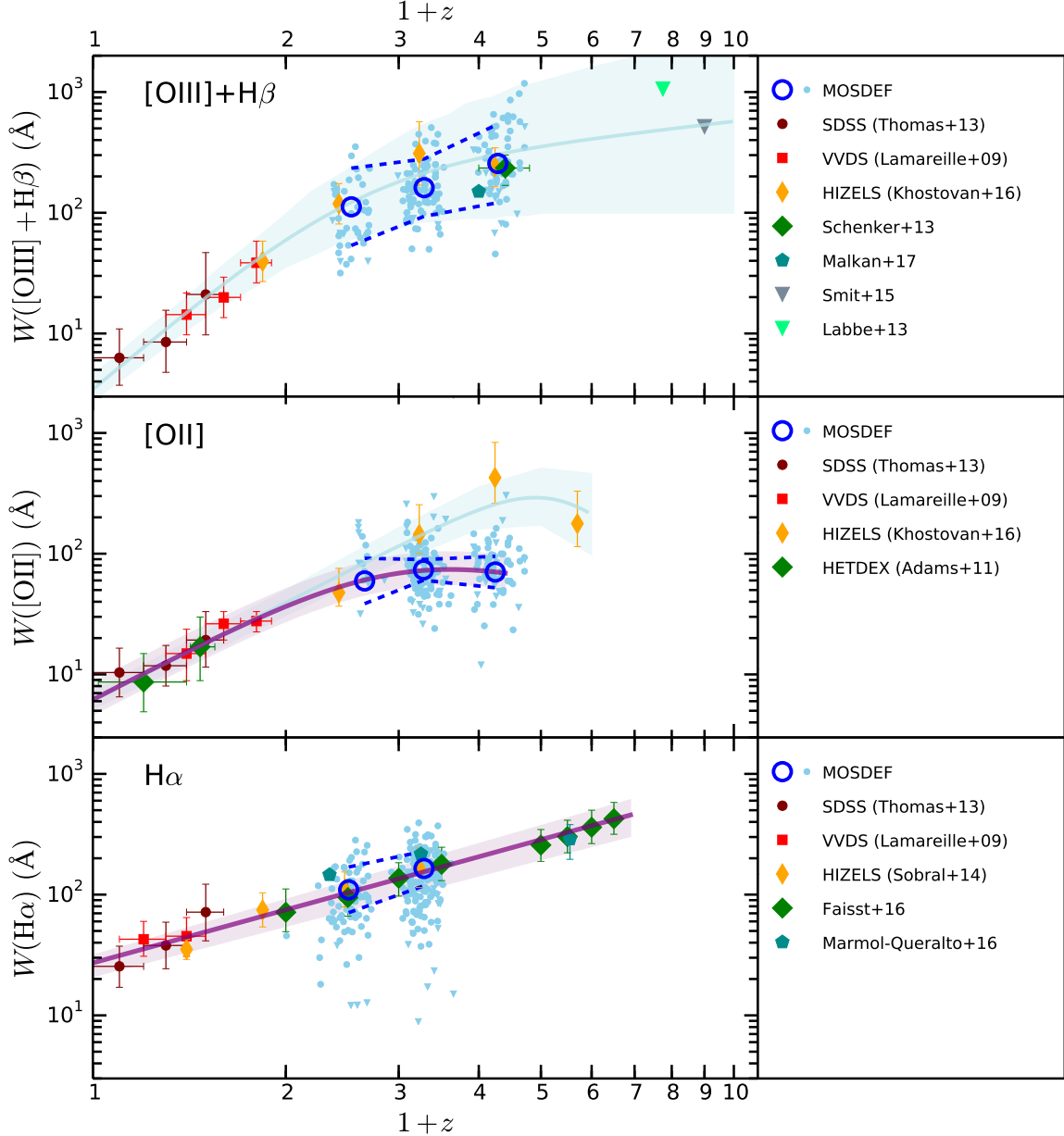


Figure 23. Average rest-frame equivalent widths of [O III] + H β (*top*), [O II] (*middle*), and H α (*bottom*) as a function of redshift for star-forming galaxies with $M_* = 10^{9.5} - 10^{10.0} M_\odot$ in the MOSDEF sample, where individual objects with detected lines are indicated by the small cyan circles, objects with upper limits in line equivalent widths are shown by the small downward-pointing cyan triangles, and averages for each redshift subsample (including both detections and non-detections) are denoted by the large open blue circles. Several other literature values are included for galaxies over the same aforementioned stellar mass range (e.g., see Khostovan et al. 2016). In each panel, the thick dashed blue lines indicate the average equivalent widths for galaxies in two other mass ranges, $M_* = 10^{9.0} - 10^{9.5} M_\odot$ (upper dashed lines) and $M_* = 10^{10.0} - 10^{10.5} M_\odot$ (lower dashed lines). The light blue line and shaded regions in the upper two panels show double power-law fits and their 95% confidence bands to the evolution in $W([\text{O III}] + \text{H}\beta)$ and $W([\text{O II}])$ with redshift presented in Khostovan et al. (2016). The purple line and shaded region in the middle panel shows a double power-law fit and the 95% confidence band to the evolution in $W([\text{O II}])$ with redshift when including only the MOSDEF points above $z \gtrsim 1$. The purple line and shaded region in the bottom panel indicate the same for a single power-law fit to $W(\text{H}\alpha)$ versus redshift for all the data shown.

slits were placed on galaxies according to their H -band continuum centroids. If the [O II] line emission is significantly offset from the continuum centroid of a galaxy, then the spectroscopically measured $W([\text{O II}])$ for such a galaxy may underestimate the true value.

Another possible contributing reason for this disparity in the inferred redshift evolution of $W([\text{O II}])$ is that the Khostovan et al. (2016) analysis was based on a narrowband selection of line emitters that is sensitive to galaxies

with $W([\text{O II}]) \gtrsim 25 \text{ \AA}$. If these narrowband samples miss populations of galaxies with equivalent widths lower than this limit, then the average equivalent widths deduced from these samples will be biased high relative to those inferred from spectroscopic surveys such as MOSDEF. Indeed, in the MOSDEF sample, we find a small number of galaxies with either measured $W([\text{O II}]) \lesssim 25 \text{ \AA}$ or upper limits in [O II] that could potentially lie below this equivalent width limit. Consequently, one should be

cautious of using narrowband-selected samples of high-redshift galaxies to deduce the evolution of equivalent widths of weak lines such as [O II].

Finally, while the MOSDEF sample has been vetted for AGNs using a number of different photometric, spectroscopic, and multi-wavelength criteria (Coil et al. 2015), such detailed (and particularly spectroscopic) information was only available for a subset of the HIZELS sample (Sobral et al. 2016). Contaminating AGNs with very high [O II] equivalent widths may result in a high average $W([\text{O II}])$ for the narrowband sample. In principle, one might expect such AGNs to also exhibit high equivalent widths of [O III] as well, but we find that insofar as [O III]+H β is concerned, the mean equivalent widths of this line complex are similar between the MOSDEF and HIZELS samples (top panel of Figure 23). At any rate, complete spectroscopy for the existing narrowband samples should help to clarify the cause of the discrepancy in the evolution of $W([\text{O II}])$ versus redshift deduced from these samples relative to that inferred from the MOSDEF sample. One obvious implication of the steep redshift evolution of $W([\text{O III}] + \text{H}\beta)$ (and $W([\text{O III}])$) relative to that of $W([\text{O II}])$ for galaxies with similar masses is that the O32 ratio, or ionization parameter, increases with redshift at a fixed stellar mass, a result that has been noted previously (e.g., Khostovan et al. 2016; Sanders et al. 2016b).

Separately, we note that the nebular reddening of galaxies of a fixed stellar mass does not appear to evolve strongly with redshift (e.g., Domínguez et al. 2013), in much the same way that the stellar attenuation at a fixed stellar mass also appears to be invariant with redshift (e.g., see Section 4.3). As such, the redshift evolution in the dust-corrected SFR[H α] versus M_* relationship translates directly to a corresponding evolution in the observed $L(\text{H}\alpha)$, or $W(\text{H}\alpha)$, versus M_* relation, such that galaxies at a fixed stellar mass have $W(\text{H}\alpha)$ that increase with redshift. This expectation is borne out by the bottom panel of Figure 23, which shows a steady increase in $W(\text{H}\alpha)$ for galaxies of a fixed stellar mass of $M_* \simeq 10^{9.75} M_\odot$. One of the primary results of our analysis is that the redshift evolution of the equivalent widths is directly tied to the redshift evolution in the SFR- M_* and MZR relations (Section 4.1).

4.7. A Strategy for Identifying High-excitation and High-ionization Galaxies

The relationships presented in Section 3 and discussed in Section 4 point to a clear strategy of identifying galaxies that are likely typical of those at much higher redshifts ($z \gtrsim 5$), namely, those with bluer UV spectral slopes and lower reddening, lower stellar masses, younger ages, higher sSFRs, ISM line ratios indicative of higher ionization parameters and excitation conditions, lower metallicities, and higher ionizing photon production efficiencies (ξ_{ion}). Specifically, these characteristics are typical of galaxies with the highest equivalent widths of the [O III] and recombination lines. Additionally, many of the trends between equivalent width and other galaxy/ISM properties are dependent on redshift, in the sense of increasing equivalent widths with redshift at fixed values of reddening, stellar mass, SFR, and metallicity.

Of the emission lines explored in our study, the equiva-

lent width of [O III] correlates most strongly with many of the aforementioned properties, while [O II] shows the least significant correlations. Fortuitously, the [O III] line can be the strongest rest-frame optical emission line, particularly for low-mass and faint star-forming galaxies where the recombination lines may be weak (e.g., see Malkan et al. 2017 and references therein). By combining the information shown in Figures 9 and 10, we can assess how the equivalent width can be used to select galaxies in certain regions of “BPT” space, traditionally defined as $\log[\text{O3}]$ versus $\log[\text{N2}]$ (Baldwin et al. 1981). A number of studies have found that $z \gtrsim 1$ galaxies are offset toward higher $\log[\text{O3}]$ at a fixed $\log[\text{N2}]$ than local galaxies (e.g., Shapley et al. 2005; Erb et al. 2006b; Liu et al. 2008; Masters et al. 2014; Steidel et al. 2014; Shapley et al. 2015), a result that is shown through the MOSDEF sample in Figure 24. Despite this offset, it is clear that both the low- and high-redshift galaxies exhibit increasing $W([\text{O III}])$ with decreasing N2 and increasing O3 (e.g., see also Figures 9 and 10). Galaxies with the highest equivalent widths of [O III] occupy the upper-left region of the BPT diagram, indicative of them being the most “extreme” sources in our sample in terms of their low metallicities and high excitation-sensitive line ratios (e.g., O3). This is a similar region of BPT parameter space where local compact starbursting galaxies known as “Green Peas” lie, many of which have low stellar masses ($M_* \lesssim 10^{10} M_\odot$; Cardamone et al. 2009), low metallicities ($12 + \log(\text{O}/\text{H}) \simeq 8.05$; Amorín et al. 2010, 2012), and high sSFRs (typically between 10^{-10} and 10^{-8} yr^{-1} ; Cardamone et al. 2009; Izotov et al. 2011). The ease of detecting the strong [O III] line and the sensitivity of its equivalent width to stellar population and ISM properties—assuming that AGNs can be isolated based on other imaging and/or spectroscopy—make the [O III] line an ideal target for future narrowband and spectroscopic followup of high-excitation, low-mass, and low-metallicity galaxies at high redshift.

Such galaxies are also believed to be conducive to both the production and escape of ionizing radiation. In terms of production, for example, galaxies with higher equivalent widths also tend to have larger ionizing photon production efficiencies, ξ_{ion} (Figure 12). The sensitivity of equivalent width to ξ_{ion} is expected for simple physical reasons. Higher ionizing photon production rates can result from stellar populations with harder ionizing spectra, which in turn can lead to higher ionization parameters and higher [O III] and Balmer emission line equivalent widths (e.g., Figure 13).

In terms of the escape of ionizing radiation, the trend of increasing neutral gas covering fraction with reddening (Reddy et al. 2016b) and the trend between equivalent width and reddening/UV slope imply that galaxies with higher equivalent widths have lower gas covering fractions, and hence larger ionizing escape fractions, on average. Moreover, galaxies that occupy the upper-left region of the BPT diagram also show significantly larger Ly α equivalent widths (Erb et al. 2014; Trainor et al. 2016) which may be indicative of lower gas covering fractions (Shapley et al. 2003; Hayes et al. 2011; Jones et al. 2013; Rudie et al. 2013; Borthakur et al. 2014; Alexandroff et al. 2015; Trainor et al. 2015; Dijkstra et al. 2016; Reddy et al. 2016b) and/or a higher

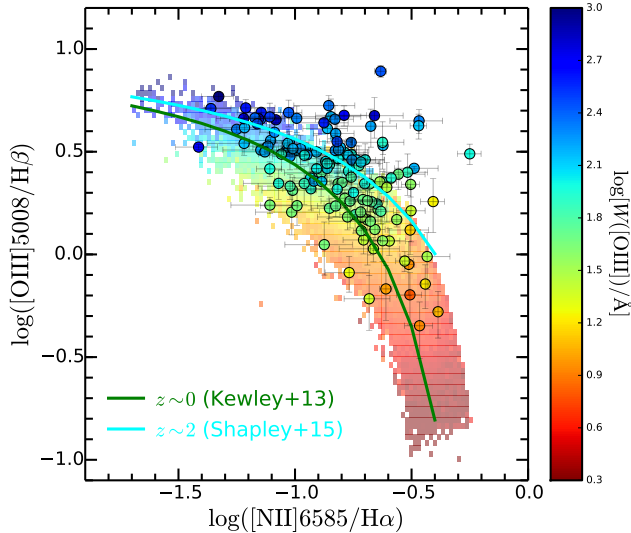


Figure 24. $\log(\text{O3})$ versus $\log(\text{N2})$ (i.e., the BPT diagram) for galaxies in the MOSDEF sample where all four lines are detected, indicated by the circles. The same is also shown for the SDSS sample—objects lying above the Kauffmann et al. (2003) demarcation between star-forming galaxies and AGNs are not shown as they were excluded from the local comparison sample (see Section 2.3). To facilitate the comparison with previous studies (i.e., Kewley et al. 2013 and Shapley et al. (2015)), the O3 and N2 line ratios shown here for the SDSS galaxies are not corrected for DIG emission. Points have been color-coded by [O III] equivalent width. The green and cyan lines indicate the average trend between $\log(\text{O3})$ and $\log(\text{N2})$ for the SDSS and $z \sim 2$ MOSDEF samples, respectively, from Kewley et al. (2013) and Shapley et al. (2015).

intrinsic production rate of ionizing photons (Erb et al. 2014; Trainor et al. 2016; Du et al. 2018). While the gas covering fraction may correlate inversely with $W([\text{O III}])$, we find that the highest $W([\text{O III}])$ galaxies in our sample have average O32 ratios $\lesssim 5$ (Figure 8), below the values expected for density-bounded nebulae (e.g., Nakajima et al. 2013). Thus, one might still expect significant Ly α opacity along the line-of-sight for galaxies with high $W([\text{O III}])$, as would be the case for a patchy ISM. Regardless, local Lyman continuum emitters also appear to lie in the region of the BPT diagram occupied by high $W([\text{O III}])$ galaxies (Izotov et al. 2016, 2017).

Along these lines, several studies have suggested that local galaxies with higher Balmer line equivalent widths have larger Ly α escape fractions (Cowie et al. 2011; Henry et al. 2015; Izotov et al. 2016). The connection between Ly α and the escape of ionizing radiation in both local and high-redshift galaxies (e.g., Kornei et al. 2010; Hayes et al. 2011; Jones et al. 2013; Wofford et al. 2013; Borthakur et al. 2014; Henry et al. 2015; Izotov et al. 2016; Trainor et al. 2015; Dijkstra et al. 2016; Trainor et al. 2016; Reddy et al. 2016b; Steidel et al. 2018) then suggests that galaxies with high Balmer emission line equivalent widths are likely to have larger ionizing escape fractions, at least up to the point where the escape fractions are not so high as to suppress the H I recombination line strengths. Our results show that galaxies with high Balmer line equivalent widths exhibit the highest [O III] equivalent widths as well (e.g., see also Cowie et al. 2011; Nakajima et al. 2013; Henry et al. 2015; Izotov et al. 2016). Thus, galaxies with high [O III] (and Balmer emission line) equivalent widths may be typical of those that leak ionizing radiation and contribute significantly

to cosmic reionization. Given the connection between escaping ionizing radiation and the intensity and hardness of the ionizing radiation field, it is clear that understanding the relationship between proxies for the latter (e.g., O32, O3, and ξ_{ion}) and line equivalent widths will be essential for identifying and characterizing galaxies that dominate the ionizing photon budget at high redshift.

5. CONCLUSIONS

We use ground-based *YJHK* spectroscopy for 1,134 galaxies with stellar masses $M_* \gtrsim 10^9 M_\odot$ from the MOSDEF survey to investigate how strong rest-frame optical emission line equivalent widths vary with a number of galaxy and ISM properties, including stellar mass, UV slope, age, SFR, sSFR, ionization parameter, gas-phase metallicity, and ionizing photon production efficiency. Our main results are summarized below.

- In general, rest-frame optical emission line equivalent widths are significantly correlated with several galaxy properties. We find that at a fixed redshift, galaxies with larger equivalent widths have lower stellar masses, bluer UV slopes, younger ages, higher specific SFRs, higher ionization parameters, lower gas-phase metallicities, and higher ionizing photon production efficiencies (ξ_{ion}). The equivalent width of [O II] generally exhibits the least significant correlations with the aforementioned properties, while the equivalent widths of [O III] and [O III]+H β correlate most strongly with these properties.
- The redshift evolution of the trends between equivalent width and stellar mass, UV slope, and SFR can be explained in the context of the increasing SFR and decreasing metallicity with redshift for galaxies of a fixed stellar mass. At a fixed mass and metallicity, the [O III] line luminosity and equivalent width increase with SFR due to a larger ionizing photon rate, while at a fixed mass and SFR, the [O III] line luminosity and equivalent width increase with decreasing metallicity due to a harder ionizing spectrum. The aforementioned trends imply that when the SFR, stellar mass, and metallicity are fixed, galaxies have similar equivalent widths irrespective of redshift. It is for this reason that the relationship between equivalent width and specific SFR evolves very little with redshift between $z \sim 0$ and $z \sim 4$, particularly when considering galaxies of a fixed metallicity.
- The relationship between [O III] equivalent width and stellar mass plateaus at stellar masses $M_* \lesssim 10^9 M_\odot$. This behavior could be physically explained by a rapid enrichment of α elements, the suppression of the oxygen lines in galaxies with metallicities below $\simeq \frac{1}{3} Z_\odot$, and/or the efficient dilution of the gas-phase metallicity due to SNe and stellar feedback in low-mass galaxies.
- Of all the strong rest-frame optical lines, the equivalent width of [O III] correlates most significantly with many of the galaxy and ISM properties considered in this study, thus marking it as a powerful probe of low-mass, young, high-excitation, and

low-metallicity galaxies at high redshift. In particular, the [O III] (and Balmer emission line) equivalent widths correlate significantly with age, ionization parameter, and the ionizing photon production efficiency ξ_{ion} , all factors that are believed to be conducive to the escape of ionizing radiation. As a consequence, galaxies with high [O III] and Balmer emission line equivalent widths are likely to contribute significantly to cosmic reionization.

In Appendix D, we provide prescriptions for translating the equivalent widths of line complexes (e.g., [O III] + H β , H α + [N II]) obtained from narrowband or low-spectral-resolution data to those of single ionic species. Beyond enabling such simple prescriptions and allowing one to evaluate the impact of line emission on galaxy photometry, the MOSDEF sample provides a robust foundation for evaluating the evolution of equivalent widths over broader dynamic ranges in galaxy/ISM properties and redshifts made possible with the next generation of ground- and space-based observatories. In the future, the *James Webb Space Telescope (JWST)* will allow spectroscopic access to many of the same emission features for galaxies up to $z \simeq 10$. Thus, it is anticipated that within the next several years, we will have a comprehensive view of how the strong rest-frame optical emission lines and the properties inferred from them evolve over roughly 97% of cosmic history.

N.A.R. thanks Matt Malkan and Daniel Cohen for providing some of the data shown in Figure 22 in electronic format. We acknowledge support from NSF AAG grants AST-1312780, 1312547, 1312764, and 1313171; archival grant AR-13907 provided by NASA through the Space Telescope Science Institute; and grant NNX16AF54G from the NASA ADAP program. R.L.S. was supported by a UCLA Graduate Division Dissertation Year Fellowship. A.E.S. acknowledges a NASA contract supporting the “WFIRST Extragalactic Potential Observations (EXPO) Science Investigation Team” (15-WFIRST15-0004), administered by GSFC. We are grateful to the MOSFIRE instrument team for building this powerful instrument, and to Marc Kassis at the Keck Observatory for his many valuable contributions to the execution of the MOSDEF survey. We also acknowledge the 3D-HST collaboration, who provided us with spectroscopic and photometric catalogs used to select MOSDEF targets and derive stellar population parameters. We also thank I. McLean, K. Kulas, and G. Mace for taking observations for the MOSDEF survey in 2013 May and June. We wish to extend special thanks to those of Hawaiian ancestry on whose sacred mountain we are privileged to be guests. Without their generous hospitality, the observations presented herein would not have been possible.

REFERENCES

- Abazajian, K. N., Adelman-McCarthy, J. K., Agüeros, M. A., et al. 2009, *ApJS*, 182, 543
- Adams, J. J., Blanc, G. A., Hill, G. J., et al. 2011, *ApJS*, 192, 5
- Alexandroff, R. M., Heckman, T. M., Borthakur, S., Overzier, R., & Leitherer, C. 2015, *ApJ*, 810, 104
- Amorín, R., Pérez-Montero, E., Vílchez, J. M., & Papaderos, P. 2012, *ApJ*, 749, 185
- Amorín, R. O., Pérez-Montero, E., & Vílchez, J. M. 2010, *ApJ*, 715, L128
- Anders, P., & Fritze-v. Alvensleben, U. 2003, *A&A*, 401, 1063
- Andrews, B. H., & Martini, P. 2013, *ApJ*, 765, 140
- Asplund, M., Grevesse, N., Sauval, A. J., & Scott, P. 2009, *ARA&A*, 47, 481
- Atek, H., Malkan, M., McCarthy, P., et al. 2010, *ApJ*, 723, 104
- Atek, H., Siana, B., Scarlata, C., et al. 2011, *ApJ*, 743, 121
- Atek, H., Kneib, J.-P., Pacifici, C., et al. 2014, *ApJ*, 789, 96
- Azadi, M., Coil, A. L., Aird, J., et al. 2017, *ApJ*, 835, 27
- Baldwin, J. A., Phillips, M. M., & Terlevich, R. 1981, *PASP*, 93, 5
- Borthakur, S., Momjian, E., Heckman, T. M., et al. 2014, *ApJ*, 795, 98
- Bouwens, R. J., Illingworth, G. D., Oesch, P. A., et al. 2015, *ApJ*, 811, 140
- Bouwens, R. J., Smit, R., Labbé, I., et al. 2016, *ApJ*, 831, 176
- Bouwens, R. J., Illingworth, G. D., Oesch, P. A., et al. 2012, *ApJ*, 754, 83
- Brammer, G. B., van Dokkum, P. G., Franx, M., et al. 2012, *ApJS*, 200, 13
- Brinchmann, J., Charlot, S., White, S. D. M., et al. 2004, *MNRAS*, 351, 1151
- Brott, I., de Mink, S. E., Cantiello, M., et al. 2011, *A&A*, 530, A115
- Bruzual, G., & Charlot, S. 2003, *MNRAS*, 344, 1000
- Calzetti, D., Armus, L., Bohlin, R. C., et al. 2000, *ApJ*, 533, 682
- Calzetti, D., Kinney, A. L., & Storchi-Bergmann, T. 1994, *ApJ*, 429, 582
- Caputi, K. I., Deshmukh, S., Ashby, M. L. N., et al. 2017, *ApJ*, 849, 45
- Cardamone, C., Schawinski, K., Sarzi, M., et al. 2009, *MNRAS*, 399, 1191
- Cardelli, J. A., Clayton, G. C., & Mathis, J. S. 1989, *ApJ*, 345, 245
- Castellano, M., Pentericci, L., Fontana, A., et al. 2017, *ApJ*, 839, 73
- Chabrier, G. 2003, *PASP*, 115, 763
- Chevallard, J., Charlot, S., Senchyna, P., et al. 2018, *MNRAS*, 479, 3264
- Coil, A. L., Aird, J., Reddy, N., et al. 2015, *ApJ*, 801, 35
- Cowie, L. L., Barger, A. J., & Hu, E. M. 2011, *ApJ*, 738, 136
- Daddi, E., Dickinson, M., Morrison, G., et al. 2007, *ApJ*, 670, 156
- Davidzon, I., Ilbert, O., Laigle, C., et al. 2017, *A&A*, 605, A70
- de Barros, S., Schaerer, D., & Stark, D. P. 2014, *A&A*, 563, A81
- Dijkstra, M., Gronke, M., & Venkatesan, A. 2016, *ApJ*, 828, 71
- Domínguez, A., Siana, B., Brooks, A. M., et al. 2015, *MNRAS*, 451, 839
- Domínguez, A., Siana, B., Henry, A. L., et al. 2013, *ApJ*, 763, 145
- Donley, J. L., Koekemoer, A. M., Brusa, M., et al. 2012, *ApJ*, 748, 142
- Dopita, M. A., & Evans, I. N. 1986, *ApJ*, 307, 431
- Dopita, M. A., Fischera, J., Sutherland, R. S., et al. 2006, *ApJ*, 647, 244
- Du, X., Shapley, A. E., Reddy, N. A., et al. 2018, *ArXiv e-prints*, arXiv:1803.05912
- Eldridge, J. J., & Stanway, E. R. 2009, *MNRAS*, 400, 1019
- Eldridge, J. J., Stanway, E. R., Xiao, L., et al. 2017, *PASA*, 34, e058
- Erb, D. K., Shapley, A. E., Pettini, M., et al. 2006a, *ApJ*, 644, 813
- Erb, D. K., Steidel, C. C., Shapley, A. E., et al. 2006b, *ApJ*, 646, 107
- Erb, D. K., Steidel, C. C., Trainor, R. F., et al. 2014, *ApJ*, 795, 33
- Faisst, A. L., Masters, D., Wang, Y., et al. 2018, *ApJ*, 855, 132
- Faisst, A. L., Capak, P., Hsieh, B. C., et al. 2016, *ApJ*, 821, 122
- Faucher-Giguère, C.-A. 2018, *MNRAS*, 473, 3717
- Ferland, G. J., Chatzikos, M., Guzmán, F., et al. 2017, *Rev. Mexicana Astron. Astrofis.*, 53, 385
- Forrest, B., Tran, K.-V. H., Broussard, A., et al. 2017, *ApJ*, 838, L12
- Förster Schreiber, N. M., Genzel, R., Bouché, N., et al. 2009, *ApJ*, 706, 1364
- Fumagalli, M., Patel, S. G., Franx, M., et al. 2012, *ApJ*, 757, L22
- Gallazzi, A., Charlot, S., Brinchmann, J., White, S. D. M., & Tremonti, C. A. 2005, *MNRAS*, 362, 41
- Geach, J. E., Smail, I., Best, P. N., et al. 2008, *MNRAS*, 388, 1473
- González, V., Bouwens, R., Illingworth, G., et al. 2014, *ApJ*, 781, 34
- González, V., Bouwens, R. J., Labbé, I., et al. 2012, *ApJ*, 755, 148

- Gordon, K. D., Clayton, G. C., Misselt, K. A., Landolt, A. U., & Wolff, M. J. 2003, *ApJ*, 594, 279
- Groggin, N. A., Kocevski, D. D., Faber, S. M., et al. 2011, *ApJS*, 197, 35
- Groves, B., Brinchmann, J., & Walcher, C. J. 2012, *MNRAS*, 419, 1402
- Guo, Y., Rafelski, M., Faber, S. M., et al. 2016, *ApJ*, 833, 37
- Hainline, K. N., Shapley, A. E., Kornei, K. A., et al. 2009, *ApJ*, 701, 52
- Hao, C.-N., Kennicutt, R. C., Johnson, B. D., et al. 2011, *ApJ*, 741, 124
- Hayashi, M., Ly, C., Shimasaku, K., et al. 2015, *PASJ*, 67, 80
- Hayes, M., Schaerer, D., Östlin, G., et al. 2011, *ApJ*, 730, 8
- Henry, A., Scarlata, C., Martin, C. L., & Erb, D. 2015, *ApJ*, 809, 19
- Holden, B. P., Oesch, P. A., González, V. G., et al. 2016, *ApJ*, 820, 73
- Hopkins, P. F., Kereš, D., Oñorbe, J., et al. 2014, *MNRAS*, 445, 581
- Inoue, A. K. 2001, *AJ*, 122, 1788
- Inoue, A. K., Hirashita, H., & Kamaya, H. 2001, *ApJ*, 555, 613
- Izotov, Y. I., Guseva, N. G., & Thuan, T. X. 2011, *ApJ*, 728, 161
- Izotov, Y. I., Schaerer, D., Thuan, T. X., et al. 2016, *MNRAS*, 461, 3683
- Izotov, Y. I., Thuan, T. X., & Guseva, N. G. 2017, *MNRAS*, 471, 548
- Jones, T. A., Ellis, R. S., Schenker, M. A., & Stark, D. P. 2013, *ApJ*, 779, 52
- Kashino, D., Silverman, J. D., Rodighiero, G., et al. 2013, *ApJ*, 777, L8
- Kashino, D., Silverman, J. D., Sanders, D., et al. 2017, *ApJ*, 835, 88
- Kauffmann, G., Heckman, T. M., Tremonti, C., et al. 2003, *MNRAS*, 346, 1055
- Kennicutt, R. C. 1998, *ARA&A*, 36, 189
- Kewley, L. J., & Ellison, S. L. 2008, *ApJ*, 681, 1183
- Kewley, L. J., Maier, C., Yabe, K., et al. 2013, *ApJ*, 774, L10
- Kewley, L. J., Zahid, H. J., Geller, M. J., et al. 2015, *ApJ*, 812, L20
- Khostovan, A. A., Sobral, D., Mobasher, B., et al. 2016, *MNRAS*, 463, 2363
- Koekemoer, A. M., Faber, S. M., Ferguson, H. C., et al. 2011, *ApJS*, 197, 36
- Kornei, K. A., Shapley, A. E., Erb, D. K., et al. 2010, *ApJ*, 711, 693
- Kriek, M., van Dokkum, P. G., Whitaker, K. E., et al. 2011, *ApJ*, 743, 168
- Kriek, M., Shapley, A. E., Reddy, N. A., et al. 2015, *ApJS*, 218, 15
- Labbé, I., Oesch, P. A., Bouwens, R. J., et al. 2013, *ApJ*, 777, L19
- Lamareille, F., Brinchmann, J., Contini, T., et al. 2009, *A&A*, 495, 53
- Leitherer, C., Ekström, S., Meynet, G., et al. 2014, *ApJS*, 212, 14
- Leitherer, C., Schaerer, D., Goldader, J. D., Delgado, R. M. G., Robert, C., Kune, D. F., de Mello, D. F., Devost, D., & Heckman, T. M. 1999, *ApJS*, 123, 3
- Levesque, E. M., Leitherer, C., Ekstrom, S., Meynet, G., & Schaerer, D. 2012, *ApJ*, 751, 67
- Liu, X., Shapley, A. E., Coil, A. L., Brinchmann, J., & Ma, C.-P. 2008, *ApJ*, 678, 758
- Ly, C., Malkan, M. A., Kashikawa, N., et al. 2012, *ApJ*, 757, 63
- Ly, C., Malkan, M. A., Rigby, J. R., & Nagao, T. 2016, *ApJ*, 828, 67
- Ly, C., Rigby, J. R., Cooper, M., & Yan, R. 2015, *ApJ*, 805, 45
- Mainali, R., Kollmeier, J. A., Stark, D. P., et al. 2017, *ApJ*, 836, L14
- Maiolino, R., Nagao, T., Grazian, A., et al. 2008, *A&A*, 488, 463
- Malkan, M. A., Teplitz, H., & McLean, I. S. 1996, *ApJ*, 468, L9
- Malkan, M. A., Cohen, D. P., Maruyama, M., et al. 2017, *ApJ*, 850, 5
- Mannucci, F., Thompson, D., Beckwith, S. V. W., & Williger, G. M. 1998, *ApJ*, 501, L11
- Mármol-Queraltó, E., McLure, R. J., Cullen, F., et al. 2016, *MNRAS*, 460, 3587
- Maseda, M. V., van der Wel, A., Rix, H.-W., et al. 2014, *ApJ*, 791, 17
- Masters, D., McCarthy, P., Siana, B., et al. 2014, *ApJ*, 785, 153
- Matthee, J., Sobral, D., Best, P., et al. 2017, *MNRAS*, 471, 629
- McCarthy, P. J., Yan, L., Freudling, W., et al. 1999, *ApJ*, 520, 548
- McLean, I. S., Steidel, C. C., Epps, H. W., et al. 2012, in *Society of Photo-Optical Instrumentation Engineers (SPIE) Conference Series*, Vol. 8446, Society of Photo-Optical Instrumentation Engineers (SPIE) Conference Series
- Meurer, G. R., Heckman, T. M., & Calzetti, D. 1999, *ApJ*, 521, 64
- Nakajima, K., Ellis, R. S., Iwata, I., et al. 2016, *ApJ*, 831, L9
- Nakajima, K., Ouchi, M., Shimasaku, K., et al. 2013, *ApJ*, 769, 3
- Nanayakkara, T., Glazebrook, K., Kacprzak, G. G., et al. 2017, *MNRAS*, 468, 3071
- Noeske, K. G., Weiner, B. J., Faber, S. M., et al. 2007, *ApJ*, 660, L43
- Oke, J. B., & Gunn, J. E. 1983, *ApJ*, 266, 713
- Onodera, M., Carollo, C. M., Lilly, S., et al. 2016, *ApJ*, 822, 42
- Pannella, M., Carilli, C. L., Daddi, E., et al. 2009, *ApJ*, 698, L116
- Papovich, C., Finkelstein, S. L., Ferguson, H. C., Lotz, J. M., & Giavalisco, M. 2011, *MNRAS*, 412, 1123
- Pérez-Montero, E. 2014, *MNRAS*, 441, 2663
- Pettini, M., & Pagel, B. E. J. 2004, *MNRAS*, 348, L59
- Rasappu, N., Smit, R., Labbé, I., et al. 2016, *MNRAS*, 461, 3886
- Reddy, N., Dickinson, M., Elbaz, D., et al. 2012a, *ApJ*, 744, 154
- Reddy, N. A., Erb, D. K., Pettini, M., Steidel, C. C., & Shapley, A. E. 2010, *ApJ*, 712, 1070
- Reddy, N. A., Pettini, M., Steidel, C. C., et al. 2012b, *ApJ*, 754, 25
- Reddy, N. A., Steidel, C. C., Fadda, D., et al. 2006, *ApJ*, 644, 792
- Reddy, N. A., Steidel, C. C., Pettini, M., & Bogosavljević, M. 2016a, *ApJ*, 828, 107
- Reddy, N. A., Steidel, C. C., Pettini, M., Bogosavljević, M., & Shapley, A. E. 2016b, *ApJ*, 828, 108
- Reddy, N. A., Kriek, M., Shapley, A. E., et al. 2015, *ApJ*, 806, 259
- Reddy, N. A., Oesch, P. A., Bouwens, R. J., et al. 2018, *ApJ*, 853, 56
- Robertson, B. E., Furlanetto, S. R., Schneider, E., et al. 2013, *ApJ*, 768, 71
- Rodighiero, G., Daddi, E., Baronchelli, I., et al. 2011, *ApJ*, 739, L40
- Rudie, G. C., Steidel, C. C., Shapley, A. E., & Pettini, M. 2013, *ApJ*, 769, 146
- Salim, S., Lee, J. C., Davé, R., & Dickinson, M. 2015, *ApJ*, 808, 25
- Salim, S., Rich, R. M., Charlot, S., et al. 2007, *ApJS*, 173, 267
- Sanders, R. L., Shapley, A. E., Zhang, K., & Yan, R. 2017, *ApJ*, 850, 136
- Sanders, R. L., Shapley, A. E., Kriek, M., et al. 2015, *ApJ*, 799, 138
- . 2016a, *ApJ*, 825, L23
- . 2016b, *ApJ*, 816, 23
- . 2018, *ApJ*, 858, 99
- Schaerer, D., & de Barros, S. 2009, *A&A*, 502, 423
- Schaerer, D., de Barros, S., & Sklias, P. 2013, *A&A*, 549, A4
- Schenker, M. A., Ellis, R. S., Konidaris, N. P., & Stark, D. P. 2013, *ApJ*, 777, 67
- Schmidt, K. B., Huang, K.-H., Treu, T., et al. 2017, *ApJ*, 839, 17
- Schreiber, C., Pannella, M., Elbaz, D., et al. 2015, *A&A*, 575, A74
- Shapley, A. E., Coil, A. L., Ma, C.-P., & Bundy, K. 2005, *ApJ*, 635, 1006
- Shapley, A. E., Steidel, C. C., Pettini, M., & Adelberger, K. L. 2003, *ApJ*, 588, 65
- Shapley, A. E., Reddy, N. A., Kriek, M., et al. 2015, *ApJ*, 801, 88
- Shapley, A. E., Sanders, R. L., Reddy, N. A., et al. 2017, *ApJ*, 846, L30
- Shim, H., Chary, R.-R., Dickinson, M., et al. 2011, *ApJ*, 738, 69
- Shivaei, I., Reddy, N. A., Steidel, C. C., & Shapley, A. E. 2015a, *ApJ*, 804, 149
- Shivaei, I., Reddy, N. A., Shapley, A. E., et al. 2015b, *ApJ*, 815, 98
- Shivaei, I., Reddy, N. A., Siana, B., et al. 2018, *ApJ*, 855, 42
- Skelton, R. E., Whitaker, K. E., Momcheva, I. G., et al. 2014, *ApJS*, 214, 24
- Smit, R., Bouwens, R. J., Labbé, I., et al. 2016, *ApJ*, 833, 254
- Smit, R., Swinbank, A. M., Massey, R., et al. 2017, *MNRAS*, 467, 3306

- Smit, R., Bouwens, R. J., Labbé, I., et al. 2014, *ApJ*, 784, 58
 Smit, R., Bouwens, R. J., Franx, M., et al. 2015, *ApJ*, 801, 122
 Sobral, D., Best, P. N., Matsuda, Y., et al. 2012, *MNRAS*, 420, 1926
 Sobral, D., Best, P. N., Smail, I., et al. 2014, *MNRAS*, 437, 3516
 Sobral, D., Smail, I., Best, P. N., et al. 2013, *MNRAS*, 428, 1128
 Sobral, D., Kohn, S. A., Best, P. N., et al. 2016, *MNRAS*, 457, 1739
 Sparre, M., Hayward, C. C., Feldmann, R., et al. 2017, *MNRAS*, 466, 88
 Stark, D. P., Schenker, M. A., Ellis, R., et al. 2013, *ApJ*, 763, 129
 Stark, D. P., Walth, G., Charlot, S., et al. 2015, *MNRAS*, 454, 1393
 Stasińska, G., & Leitherer, C. 1996, *ApJS*, 107, 661
 Steidel, C. C., Bogosavlevic, M., Shapley, A. E., et al. 2018, *ArXiv e-prints*, arXiv:1805.06071
 Steidel, C. C., Strom, A. L., Pettini, M., et al. 2016, *ApJ*, 826, 159
 Steidel, C. C., Rudie, G. C., Strom, A. L., et al. 2014, *ApJ*, 795, 165
 Straughn, A. N., Kuntschner, H., Kümmel, M., et al. 2011, *AJ*, 141, 14
 Strom, A. L., Steidel, C. C., Rudie, G. C., et al. 2017, *ApJ*, 836, 164
 Suzuki, T. L., Kodama, T., Tadaki, K.-i., et al. 2015, *ApJ*, 806, 208
 Tang, M., Stark, D., Chevallard, J., et al. 2018, *ArXiv e-prints*, arXiv:1809.09637
 Teplitz, H. I., Malkan, M., & McLean, I. S. 1998, *ApJ*, 506, 519
 Teplitz, H. I., Malkan, M. A., Steidel, C. C., et al. 2000, *ApJ*, 542, 18
 Thomas, D., Steele, O., Maraston, C., et al. 2013, *MNRAS*, 431, 1383
 Thompson, D., Mannucci, F., & Beckwith, S. V. W. 1996, *AJ*, 112, 1794
 Trainor, R. F., Steidel, C. C., Strom, A. L., & Rudie, G. C. 2015, *ApJ*, 809, 89
 Trainor, R. F., Strom, A. L., Steidel, C. C., & Rudie, G. C. 2016, *ApJ*, 832, 171
 Tran, K.-V. H., Nanayakkara, T., Yuan, T., et al. 2015, *ApJ*, 811, 28
 Troncoso, P., Maiolino, R., Sommariva, V., et al. 2014, *A&A*, 563, A58
 Trump, J. R., Weiner, B. J., Scarlata, C., et al. 2011, *ApJ*, 743, 144
 van der Wel, A., Straughn, A. N., Rix, H.-W., et al. 2011, *ApJ*, 742, 111
 Weisz, D. R., Johnson, B. D., Johnson, L. C., et al. 2012, *ApJ*, 744, 44
 Whitaker, K. E., Franx, M., Leja, J., et al. 2014, *ApJ*, 795, 104
 Wisnioski, E., Förster Schreiber, N. M., Wuyts, S., et al. 2015, *ApJ*, 799, 209
 Wofford, A., Leitherer, C., & Salzer, J. 2013, *ApJ*, 765, 118
 Wuyts, S., Förster Schreiber, N. M., Lutz, D., et al. 2011, *ApJ*, 738, 106
 York, D. G., Adelman, J., Anderson, Jr., J. E., et al. 2000, *AJ*, 120, 1579
 Zackrisson, E., Bergvall, N., & Leitert, E. 2008, *ApJ*, 676, L9

APPENDIX

A. LINE LUMINOSITY COMPLETENESS

Here, we present evidence that the MOSDEF sample is mostly complete in line luminosity for galaxies above our “mass-completeness” threshold of $\simeq 10^{9.0} M_{\odot}$. Specifically, limiting our sample to galaxies that have [O III] line fluxes that are twice our nominal detection threshold changes the normalization of the trend between $W([\text{O III}])$ and M_* by $\lesssim 0.1$ dex, implying that our sample probes the tail of the $W([\text{O III}])$ distribution over the relevant range of stellar mass. Moreover, we achieve a high spectroscopic success rate ($\approx 80\%$) of identifying redshifts for objects where prior targeting information—i.e., photometric redshifts or external grism/spectroscopic redshifts—indicate that the lines of interest should fall in the wavelength ranges accessible to MOSFIRE, independent of redshift (Kriek et al. 2015). In other words, there would only be an incremental increase in successful redshifts for star-forming galaxies if we were to have increased the spectroscopic integration time. Finally, as shown in Section 3, the inclusion of objects with successful redshifts, but where one or more lines may not have been significantly detected, does little to alter the mean trends between equivalent widths and the other galaxy properties analyzed here. Further evidence of the line luminosity completeness of the MOSDEF sample comes from a comparison of the line luminosity functions inferred from the MOSDEF survey and those obtained from narrowband selected samples of high-redshift galaxies, a topic that will be discussed elsewhere. As such, we assume that relative comparisons of the trends between equivalent widths and other galaxy properties between the MOSDEF and local SDSS samples remain valid, irrespective of the depth of the MOSDEF spectroscopic observations.

B. COMPOSITE SPECTRA

Some of the lines included in our analysis are formally undetected for some galaxies, yielding only upper limits on W . To include such objects in our analysis, we combined the spectra of galaxies with detected and undetected lines in order to create a composite spectrum and compute mean equivalent widths. A composite spectrum was computed by shifting each galaxy’s spectrum into the rest frame, converting to luminosity density units, normalizing the individual spectra by the continuum luminosity density at the center of the line for which we were interested in computing the mean equivalent width for, and averaging the spectra for all galaxies contributing to the composite. Further details on how composite (and associated error) spectra were calculated are provided in Shivaee et al. (2018). Figure 25 shows an example composite spectrum—in this case, derived from 292 galaxies lying in the lowest quartile in stellar mass—along with the best-fit line profiles used to calculate the average equivalent widths.

The average equivalent width was then computed by simply integrating the composite spectrum over the line of interest in the same way that fluxes are computed for emission lines in individual galaxy spectra. Also, analogous to how line flux errors are computed for individual galaxies, the error in the average line flux was obtained by perturbing the composite spectrum by its associated error spectrum, remeasuring the line fluxes for each of these realizations, and then taking the error as the 1σ width of the distribution of the resulting line flux measurements. The error in average line flux is folded into the uncertainty on the average equivalent width.

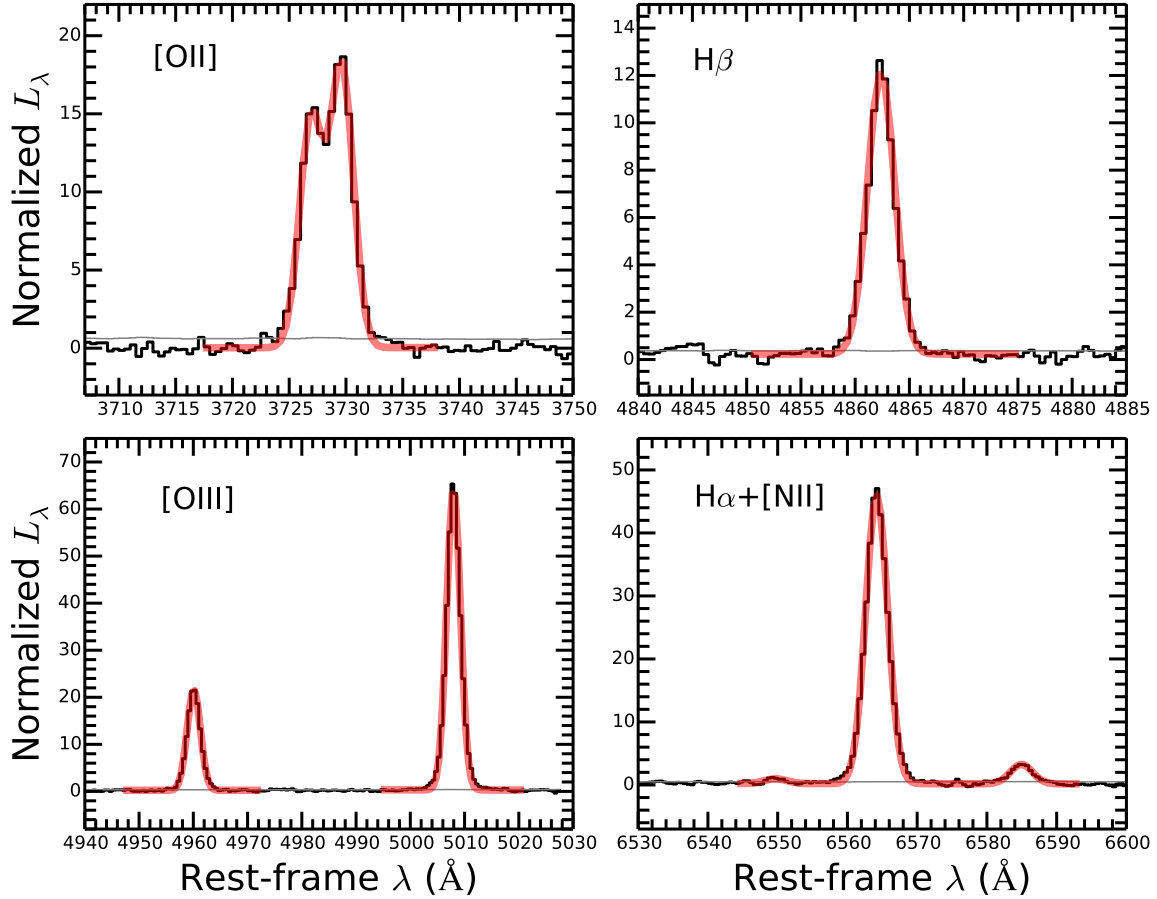


Figure 25. Composite spectrum of 292 galaxies lying in the lowest quartile of the distribution of stellar mass (*black curve*), along with the associated error spectrum (*thin gray line*), and the best-fit line profile (*red*) to each of the lines considered in our analysis.

C. EFFECT OF CHANGING THE ASSUMED STELLAR METALLICITY AND DUST OBSCURATION CURVE

As noted in Section 2.4, we assumed a fixed stellar population model ($0.28Z_{\odot}$ BC03 model) and attenuation curve (SMC) for all galaxies in our sample. In principle, a more realistic approach would allow for the stellar population to increase in stellar metallicity with the stellar mass, and also allow for grayer attenuation curves toward higher stellar masses (e.g., Reddy et al. 2018). One key test that can be used to evaluate whether a more sophisticated treatment is warranted is to directly compare the measured equivalent widths of $H\alpha$ with those predicted from the intrinsic stellar population that best fits the observed photometry. Specifically, the ionizing flux per unit SFR increases with decreasing metallicity, among other things (see below). As recombination line fluxes are directly related to the ionizing flux, a comparison between the observed recombination lines (e.g., $H\alpha$) and those predicted from various stellar population models can be used to potentially distinguish between these models.

The $H\alpha$ line luminosity predicted from a given stellar population model was computed as follows. First, the intrinsic SED corresponding to the SED that best fits the observed photometry was integrated in the range $\lambda = 200 - 912 \text{ \AA}$ to compute the H-ionizing photon luminosity, $Q(H)$. The corresponding intrinsic $H\alpha$ luminosity, $L(H\alpha)$, was calculated assuming Case B recombination and an electron temperature of $T_e = 10,000 \text{ K}$. We also assumed no escape of ionizing photons ($f_{\text{esc}} = 0$) and that there is no dust attenuation of ionizing photons, referred to as Lyman continuum extinction (Inoue 2001; Inoue et al. 2001). The former is justified as f_{esc} is on average $\lesssim 10\%$ for typical (L^*) star-forming galaxies at $z \sim 2 - 3$ (Reddy et al. 2016b; Steidel et al. 2018). The latter assumption is based on the high gas column densities inferred for $z \sim 3$ galaxies, such that photoelectric absorption, rather than dust attenuation, dominates the depletion of ionizing photons (Reddy et al. 2016b). With these assumptions, the predicted equivalent width of $H\alpha$ ($W(H\alpha)_{\text{pred}}$) was then computed by dividing $L(H\alpha)$ by the continuum luminosity density from the best-fit SED model.

To compare $W(H\alpha)_{\text{pred}}$ with the measured $W(H\alpha)$, the latter must be corrected for the attenuation of the $H\alpha$ line. For those galaxies where both $H\alpha$ and $H\beta$ were significantly detected, the Balmer decrement was computed directly from these lines. For those galaxies where only $H\alpha$ was significantly detected, and $H\beta$ was not, the Balmer decrement was derived as follows. First, we constructed composite spectra of all galaxies where $H\alpha$ was detected, without regard to whether $H\beta$ was detected, in four bins of stellar mass. The average Balmer decrement was computed from each of these composite spectra, and then we fit a linear function to these mean Balmer decrements as a function of stellar mass. Based on this linear function, a Balmer decrement was assigned to each galaxy for which $H\beta$ was undetected. Balmer decrements were then used to correct the measured $H\alpha$ equivalent widths, $W(H\alpha)_{\text{meas}}$, for the attenuation of

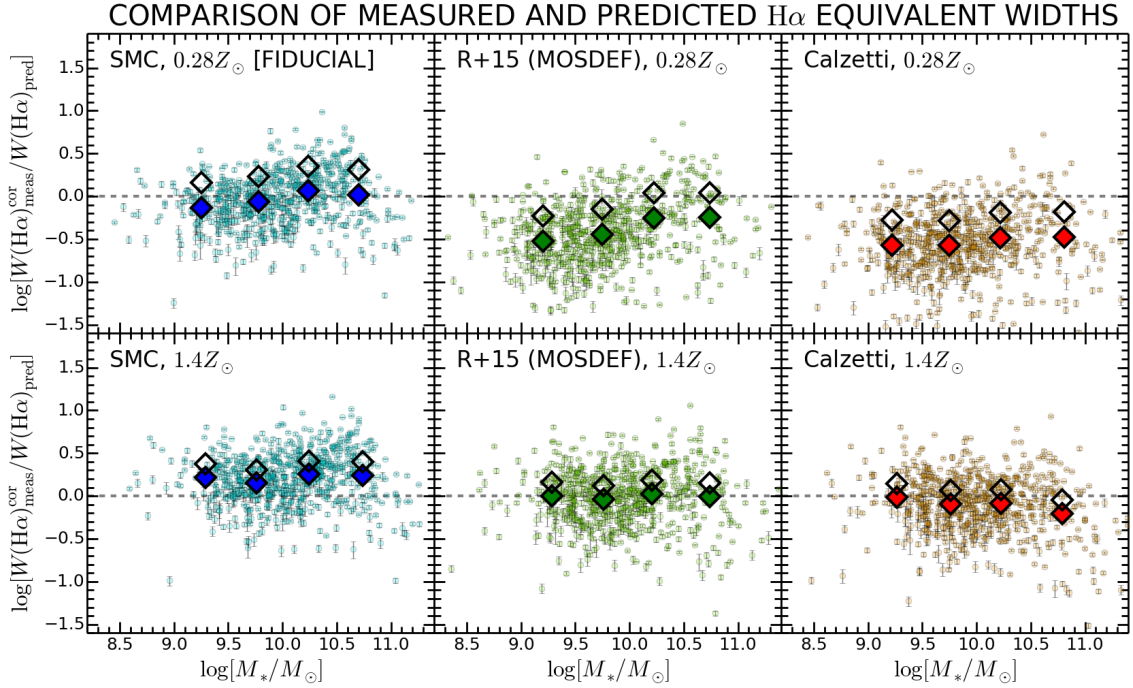


Figure 26. Comparison of the measured and predicted $H\alpha$ equivalent widths for MOSDEF galaxies with detected $H\alpha$ for different assumptions of the stellar attenuation curve and stellar population model, as indicated at the top of each panel. For comparison with the model predictions, the measured equivalent widths are corrected for dust attenuation ($W(H\alpha)_{\text{meas}}^{\text{cor}}$) based on the Balmer decrement and assuming the Cardelli et al. (1989) extinction curve. For those galaxies where $H\beta$ is undetected, the Balmer decrement is computed assuming the mean relationship between Balmer decrement and stellar mass (see text for details). The small points denote individual objects, where $\log[W(H\alpha)_{\text{meas}}^{\text{cor}}/W(H\alpha)_{\text{pred}}]$ assumes the BPASS stellar population synthesis models. The large filled and open diamonds in each panel correspond to the mean $\log[W(H\alpha)_{\text{meas}}^{\text{cor}}/W(H\alpha)_{\text{pred}}]$ in four bins of stellar mass for the BPASS and BC03 stellar population models, respectively. $H\alpha$ using the procedure outlined in Section 2.5, to yield $W(H\alpha)_{\text{meas}}^{\text{cor}}$. Note that the dust corrections are only applied to the $H\alpha$ emission; the continuum flux density is not corrected for dust in either the model predictions or the measured values.

There are large systematic offsets in the ionizing flux per unit SFR predicted by various models, particularly those that include binaries and/or rotating stars (e.g., Eldridge & Stanway 2009; Brott et al. 2011; Levesque et al. 2012; Leitherer et al. 2014; Eldridge et al. 2017). Given the apparent success of models that include binaries in reproducing simultaneously the rest-frame far-UV continuum, stellar photospheric lines, and nebular lines (both in the rest-frame far-UV and optical) of the average galaxy at $z \sim 2$ (e.g., Steidel et al. 2016), we examined the $W(H\alpha)$ predictions for the Binary Population and Spectral Synthesis (BPASS) models (Eldridge et al. 2017) that match the metallicity assumed for our fiducial model ($0.28Z_{\odot}$) and a metallicity of $1.4Z_{\odot}$.

The log of the ratio of the measured and predicted $H\alpha$ equivalent widths for galaxies with detected $H\alpha$ is shown as a function of stellar mass in Figure 26 for these two different metallicities and for three different dust curves: the SMC extinction curve, the Reddy et al. (2015) attenuation curve derived for MOSDEF galaxies at $z \sim 2$, and the Calzetti et al. (2000) attenuation curve.¹⁷ The attenuation curve used for modeling the SEDs is relevant in this comparison because the shape of the dust curve affects SFR[SED]: for a given observed SED, a steeper (SMC-like) attenuation curve yields lower $E(B - V)_{\text{stars}}$, lower SFR[SED], and hence lower $Q(H)$, relative to those derived with a grayer attenuation curve. Thus, modeling that includes an SMC-like dust curve results in $W(H\alpha)_{\text{pred}}$ that are systematically lower, and hence $\log[W(H\alpha)_{\text{meas}}^{\text{cor}}/W(H\alpha)_{\text{pred}}]$ that are systematically higher, than those derived with either the Reddy et al. (2015) or Calzetti et al. (2000) attenuation curves. These offsets that result from different assumptions of the attenuation curve increase as metallicity decreases.

The average $\log[W(H\alpha)_{\text{meas}}^{\text{cor}}/W(H\alpha)_{\text{pred}}]$ in four bins of stellar mass are indicated by the large filled diamonds in each panel of Figure 26. For comparison—and to illustrate the relative offsets in the predicted $L(H\alpha)$ between single and

¹⁷ Similar to the SMC curve used here, the dust curves given in Reddy et al. (2015) and Calzetti et al. (2000) were updated in the far-UV ($\lambda \simeq 950 - 1250 \text{ \AA}$) based on the analysis of Reddy et al.

(2016a).

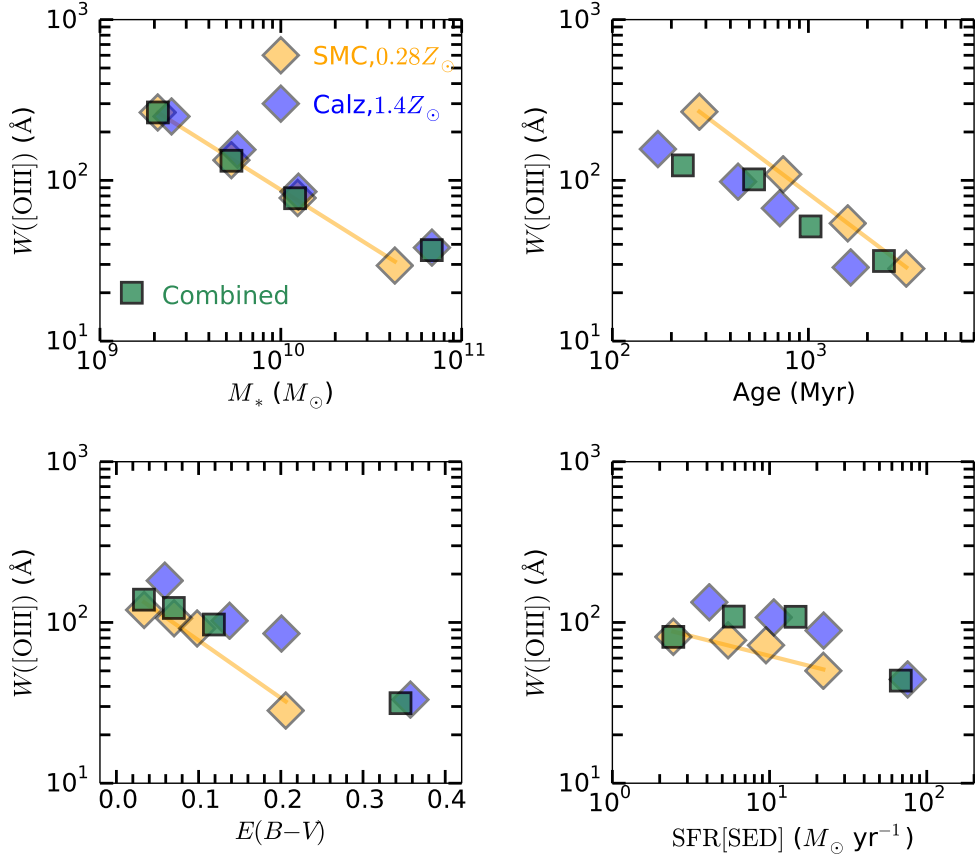


Figure 27. $W([\text{O III}])$ versus M_* , age, $E(B-V)_{\text{stars}}$, and SFR[SED]. Orange diamonds and the solid lines indicate the average values and best-fit relations, respectively, assuming our fiducial modeling with a Bruzual & Charlot (2003) $0.28Z_\odot$ metallicity stellar population and the SMC extinction curve. Blue diamonds indicate the same for a $1.4Z_\odot$ metallicity and the Calzetti et al. (2000) attenuation curve. The green squares show the results when assuming the latter set of assumptions for galaxies with $M_* \geq 3 \times 10^{10} M_\odot$, and the fiducial modeling for lower mass galaxies.

binary evolution stellar synthesis models—the large open diamonds indicate the average $\log[W(\text{H}\alpha)_{\text{meas}}^{\text{cor}}/W(\text{H}\alpha)_{\text{pred}}]$ assuming the BC03 models when computing the intrinsic ionizing flux. The single stellar evolution models predict lower ionizing fluxes per unit SFR than the binary models, resulting in larger $\log[W(\text{H}\alpha)_{\text{meas}}^{\text{cor}}/W(\text{H}\alpha)_{\text{pred}}]$ for the former.

These comparisons indicate that models that include sub-solar metallicity stellar populations and gray attenuation curves, or solar metallicity models with steep attenuation curves, predict $\text{H}\alpha$ equivalent widths that are systematically offset by up to a factor of three from the measured $\text{H}\alpha$ equivalent widths. On the other hand, our fiducial model, as well as models that include grayer attenuation curves with solar metallicity stellar populations, are generally able to reproduce the measured $\text{H}\alpha$ equivalent widths. As noted earlier, sub-solar metallicity models with steeper attenuation curves are able to better-reproduce the dust obscuration (as measured from far-IR data) at a given UV slope for $z \sim 2$ galaxies (Reddy et al. 2018). Furthermore, modeling of far-UV stellar photospheric absorption lines for typical star-forming galaxies at $z \sim 2$ also favors sub-solar metallicity models (Steidel et al. 2016). It is for these reasons that we adopted the assumptions corresponding to our fiducial modeling. However, given that the combination of solar metallicity models with gray attenuation curves is able to reproduce the measured $\text{H}\alpha$ equivalent widths, it is useful to examine how adopting these assumptions may alter some of the aforementioned trends seen between equivalent width and SED-derived parameters.

In Figure 27, we show how changing our initial assumptions for the metallicity of the stellar population and reddening curve affects the relationship between line equivalent width and SED parameters, focusing on $W([\text{O III}])$. For this demonstration, we compared the trends obtained with the fiducial modeling (i.e., SMC extinction curve and a $0.28Z_\odot$ stellar population) and those obtained with a Calzetti et al. (2000) attenuation curve and a $1.4Z_\odot$ stellar population. The latter set of assumptions yields stellar masses that are roughly 10% smaller and ages that are a factor of $\simeq 2$ younger than those obtained with the fiducial modeling. The $E(B-V)_{\text{stars}}$ are on average larger for the Calzetti et al. (2000) curve—as this is a grayer curve than the SMC extinction curve, a larger reddening is required to reproduce an observed UV spectral shape. Because of this, SFR[SED] is also systematically larger.

If we assume that all galaxies with $M_* > 3 \times 10^{10} M_\odot$ are better described by a $1.4Z_\odot$ BC03 model and the Calzetti et al. (2000) curve, and assume that galaxies below this mass follow a $0.28Z_\odot$ model and the SMC curve, then we obtain the mean trends of $W([\text{O III}])$ versus M_* , age, $E(B-V)_{\text{stars}}$, and SFR[SED] indicated by the green squares in

Table 7
Parameters for the Equivalent Width Corrections^a

Correction	Redshift Subsample	c_0	c_1	c_2
$W([\text{O III}] + \text{H}\beta) \rightarrow W([\text{O III}])$	$z \sim 1.5$	0.665	-0.0119	7.430×10^{-3}
	$z \sim 2.3$	0.616	-0.0079	6.616×10^{-3}
	$z \sim 3.4$	0.581	-0.0074	6.232×10^{-3}
$W(\text{H}\alpha + [\text{N II}]) \rightarrow W(\text{H}\alpha)$	$z \sim 1.5$	0.951	-0.1451	1.758×10^{-2}
	$z \sim 2.3$	2.063	-0.4662	3.820×10^{-2}
$W(\text{H}\alpha + [\text{N II}] + [\text{S II}]) \rightarrow W(\text{H}\alpha)$	$z \sim 1.5$	3.812	-0.8955	6.677×10^{-2}
	$z \sim 2.3$	2.376	-0.5334	4.419×10^{-2}

^a This table gives the correction factors (c) by which $W([\text{O III}] + \text{H}\beta)$ must be divided by to compute $W([\text{O III}])$, and by which $W(\text{H}\alpha + [\text{N II}])$ and $W(\text{H}\alpha + [\text{N II}] + [\text{S II}])$ must be divided by to compute $W(\text{H}\alpha)$. The correction factors are expressed as $c = c_0 + c_1x + c_2x^2$ where $x = \log[M_*/M_\odot]$, and are valid over the range $9.0 \leq \log[M_*/M_\odot] \leq 11.5$.

Figure 27. Not surprisingly, the resultant trends lie somewhere between those obtained when assuming either model for all of the galaxies in the sample. The slopes of the $W([\text{O III}])$ versus M_* and $W([\text{O III}])$ versus $E(B - V)_{\text{stars}}$ relations become slightly less negative than those obtained with the fiducial modeling. On the other hand, the slopes of $W([\text{O III}])$ versus age and $W([\text{O III}])$ versus SFR[SED] relations are not significantly affected while their normalizations are slightly lower and higher by $\simeq 0.2$ dex, respectively, than those obtained with the fiducial modeling. Similar trends are seen for lines other than [O III]. These results underscore the importance of keeping in mind the assumptions of the stellar population model and attenuation curve when examining trends between equivalent width and stellar population parameters. In the context of even higher redshift galaxies (e.g., $z \gtrsim 3$), the results obtained with our fiducial modeling are likely to be closer to reality given that such galaxies will be less metal-rich than more massive galaxies at lower redshifts.

D. EMISSION LINE EQUIVALENT WIDTH CORRECTIONS

As is often the case, various combinations of emission lines may enter into a narrowband or broadband filter depending on the redshifts of the galaxies of interest. It is common practice to use color excesses between photometric filters that contain and surround such emission lines in order to select strong line emitters. In this context, it is useful to assess the corrections required to recover the equivalent widths of single emission lines, or the emission associated with a single ionic species, from the equivalent widths inferred from such color excesses, or from low-resolution spectral data. The most common corrections involve translating $W([\text{O III}] + \text{H}\beta)$ to $W([\text{O III}])$, $W(\text{H}\alpha + [\text{N II}])$ to $W(\text{H}\alpha)$, and $W(\text{H}\alpha + [\text{N II}] + [\text{S II}])$ to $W(\text{H}\alpha)$. The relations discussed in Section 3 and tabulated in Table 8 allow us to compute these corrections as a function of various properties. Here, we focus on the corrections as a function of stellar mass computed for each redshift subsample, and shown in Figure 28 and tabulated in Table 7.

Focusing on the translation between $W([\text{O III}] + \text{H}\beta)$ and $W([\text{O III}])$, the associated corrections decrease with decreasing stellar mass at a fixed redshift, reflecting the fact that the O3 ratio decreases with increasing stellar mass (e.g., Sanders et al. 2016b). This conclusion is supported by the results shown in Figure 3, where the [O III] line luminosity is effectively constant with mass above $10^9 M_\odot$, but the H β line luminosity decreases with decreasing stellar mass over the same range in stellar mass. We also note that the correction factor at fixed mass decreases with redshift, implying that the $W([\text{O III}])$ evolves more strongly with redshift than $W(\text{H}\beta)$, another result that is evident in Figure 3, and one that can be explained in terms of the redshift evolution of the SFR- M_* and mass-metallicity relations (Section 4.1).

The corrections required to translate $W(\text{H}\alpha + [\text{N II}])$ to $W(\text{H}\alpha)$ also increase with stellar mass. In this case, as the ratio of [N II]-to-H α (i.e., the N2 index) is sensitive to oxygen abundance, the increasing strength of [N II] relative to H α with stellar mass simply reflects the higher metallicities of more massive galaxies (e.g., see also Faisst et al. 2018). While there is little discernible redshift evolution in the aforementioned corrections between the $z \sim 1.5$ and $z \sim 2.3$ subsamples, the redshift evolution of the MZR implies that the corrections to $W(\text{H}\alpha + [\text{N II}])$ should decrease with increasing redshift at a fixed stellar mass.

The correction factors associated with $W(\text{H}\alpha + [\text{N II}] + [\text{S II}])$ depend on stellar mass in a way that implies that [S II]/H α is not constant with stellar mass for the lower redshift galaxies. Comparing the slopes of the corrections for $W(\text{H}\alpha + [\text{N II}])$ and $W(\text{H}\alpha + [\text{N II}] + [\text{S II}])$ implies that that [S II]/H α increases with stellar mass for the $z \sim 1.5$ sample, but is essentially constant with stellar mass for the $z \sim 2.3$ sample. These results may suggest the varying contribution of shock-heated gas or diffuse ionized gas to the measured line ratios for galaxies of different stellar masses, a topic that is beyond the scope of this paper and will be discussed elsewhere.

Table 8
Dependence of Equivalent Widths on Stellar Populations

Attribute ^a	Line ^a	z -Range ($\langle z \rangle$) ^b	N (det/undet) ^c	ρ^d	σ_P^d	Intercept ^e	Slope ^e	RMS ^e
$\log \left[\frac{M_*}{M_\odot} \right]$	[O II]	All: 1.6013 – 3.7152 (2.4970)	542 (407/135)	-0.50	10.1	3.814 ± 0.070	-0.202 ± 0.007	0.17
		Low- z : 1.6013 – 1.7112 (1.6545)	54 (25/29)	-0.53	2.6	5.440 ± 0.279	-0.376 ± 0.029	0.21

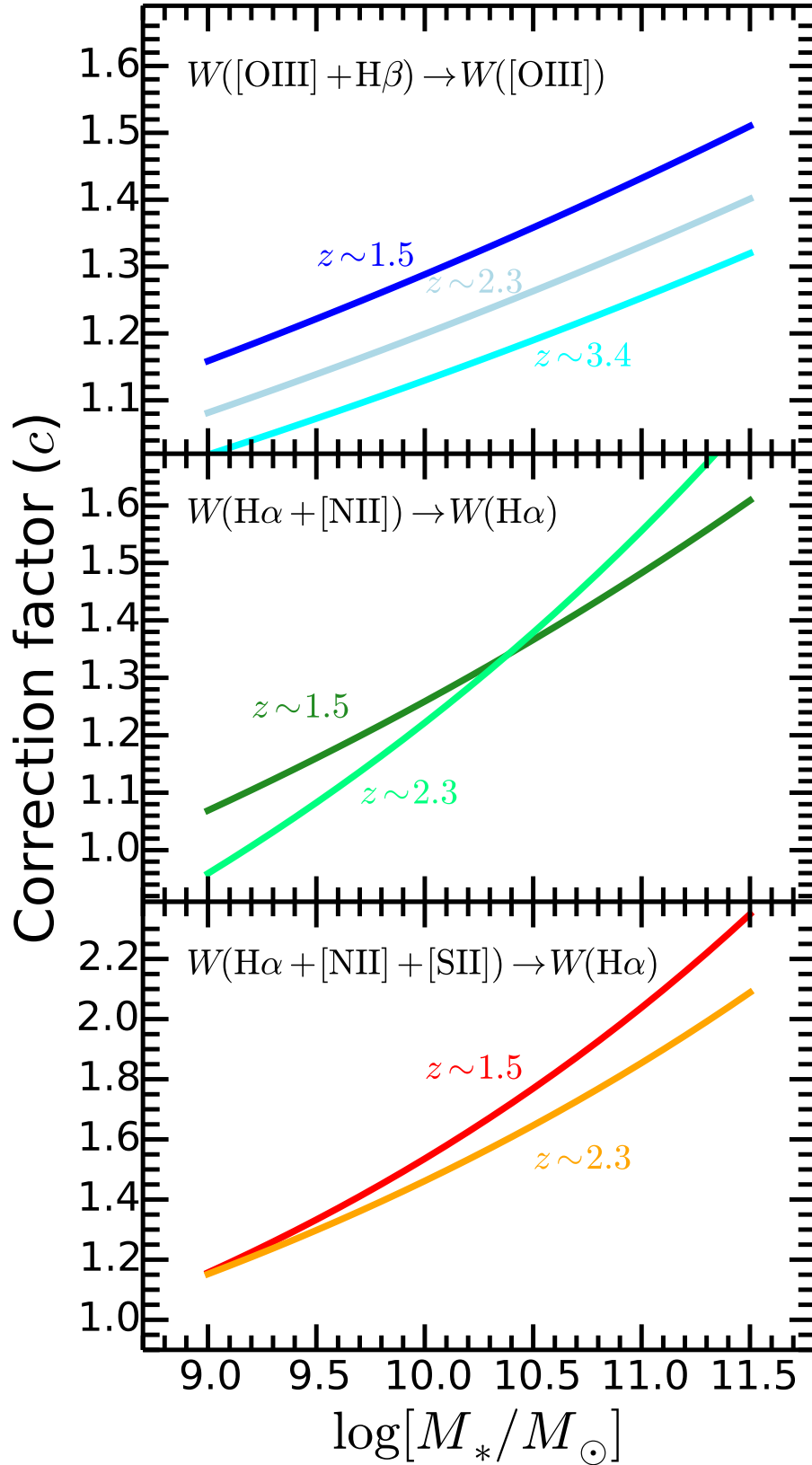


Figure 28. Correction factors (c) by which $W([\text{O III}] + \text{H}\beta)$, $W(\text{H}\alpha + [\text{N II}])$, and $W(\text{H}\alpha + [\text{N II}] + [\text{S II}])$ must be *divided* by to yield $W([\text{O III}])$, $W(\text{H}\alpha)$, and $W(\text{H}\alpha)$, respectively, as a function of stellar mass for different redshift subsamples. Functional forms for these corrections are given in Table 7.

Table 8 — *Continued*

Attribute ^a	Line ^a	z -Range ($\langle z \rangle$) ^b	N (det/undet) ^c	ρ^d	σ_P^d	Intercept ^e	Slope ^e	RMS ^e
	[O III]	Mid- z : 2.0461 – 2.6541 (2.3023)	243 (243/0)	-0.07	1.0	1.214 ± 0.020	0.087 ± 0.013	0.29
		All: 1.2467 – 2.5855 (2.0595)	388 (373/15)	-0.07	1.4	1.873 ± 0.005	0.046 ± 0.004	0.42
		Low- z : 1.2467 – 1.7292 (1.5323)	123 (111/12)	-0.27	2.9	1.884 ± 0.012	-0.121 ± 0.010	0.40
		Mid- z : 2.0151 – 2.5855 (2.2828)	265 (262/3)	-0.05	0.8	1.986 ± 0.008	0.045 ± 0.005	0.39
	[O III]+	All: 1.3685 – 2.5855 (2.0411)	301 (290/11)	0.28	5.9	1.929 ± 0.006	0.066 ± 0.005	0.39
	H β	Low- z : 1.3685 – 1.7292 (1.5232)	102 (93/9)	-0.30	2.9	1.958 ± 0.013	-0.102 ± 0.009	0.35
		Mid- z : 2.0461 – 2.5855 (2.2856)	199 (197/2)	-0.01	0.1	2.036 ± 0.008	0.060 ± 0.005	0.36
	H α	All: 1.2467 – 2.6541 (2.0897)	434 (434/0)	0.28	5.9	1.876 ± 0.004	0.134 ± 0.003	0.25
		Low- z : 1.2467 – 1.7338 (1.5361)	121 (121/0)	0.22	2.4	1.954 ± 0.006	0.015 ± 0.005	0.24
		Mid- z : 2.0151 – 2.6541 (2.3020)	314 (314/0)	0.28	5.0	1.866 ± 0.007	0.216 ± 0.004	0.25
	H α +	All: 1.3896 – 2.5605 (2.0728)	398 (267/131)	0.29	4.8	1.925 ± 0.005	0.181 ± 0.004	0.23
	[N II]	Low- z : 1.3896 – 1.7338 (1.5366)	104 (79/25)	0.21	1.9	1.995 ± 0.008	0.082 ± 0.006	0.18
		Mid- z : 2.0151 – 2.5605 (2.2981)	294 (188/106)	0.28	3.9	1.893 ± 0.008	0.268 ± 0.005	0.22
$\log \left[\frac{\text{sSFR}[\text{H}\alpha]}{\text{yr}^{-1}} \right]$	[O II]	All: 1.6013 – 2.6196 (2.2431)	231 (203/28)	0.51	7.2	3.876 ± 0.080	0.234 ± 0.009	0.17
		Low- z : 1.6013 – 1.7112 (1.6605)	25 (15/10)	0.27	1.0	4.688 ± 0.367	0.325 ± 0.042	0.20
		Mid- z : 2.0824 – 2.6196 (2.2896)	206 (188/18)	0.54	7.3	3.751 ± 0.084	0.220 ± 0.010	0.17
	H β	All: 1.3685 – 2.6541 (2.0584)	354 (354/0)	0.56	10.5	4.129 ± 0.099	0.323 ± 0.012	0.23
		Low- z : 1.3685 – 1.7338 (1.5267)	112 (112/0)	0.50	5.2	3.605 ± 0.255	0.266 ± 0.028	0.24
		Mid- z : 2.0461 – 2.6541 (2.3023)	243 (243/0)	0.63	9.8	4.292 ± 0.196	0.334 ± 0.022	0.22
	[O III]	All: 1.2467 – 2.5855 (2.0595)	388 (373/15)	0.67	12.9	6.654 ± 0.032	0.537 ± 0.004	0.32
		Low- z : 1.2467 – 1.7292 (1.5323)	123 (111/12)	0.54	5.6	5.193 ± 0.091	0.386 ± 0.010	0.38
		Mid- z : 2.0151 – 2.5855 (2.2828)	265 (262/3)	0.69	11.1	6.112 ± 0.036	0.467 ± 0.004	0.28
	[O III]+	All: 1.3685 – 2.5855 (2.0411)	301 (290/11)	0.69	11.7	6.393 ± 0.034	0.497 ± 0.004	0.30
	H β	Low- z : 1.3685 – 1.7292 (1.5232)	102 (93/9)	0.50	4.8	5.053 ± 0.090	0.357 ± 0.010	0.34
		Mid- z : 2.0461 – 2.5855 (2.2856)	199 (197/2)	0.73	10.2	5.829 ± 0.044	0.423 ± 0.005	0.27
	H α	All: 1.2467 – 2.6541 (2.0897)	434 (434/0)	0.85	17.8	5.808 ± 0.022	0.419 ± 0.003	0.13
		Low- z : 1.2467 – 1.7338 (1.5361)	121 (121/0)	0.86	9.3	5.565 ± 0.037	0.394 ± 0.004	0.13
		Mid- z : 2.0151 – 2.6541 (2.3020)	314 (314/0)	0.87	15.3	5.440 ± 0.034	0.374 ± 0.004	0.14
	H α +	All: 1.3896 – 2.5605 (2.0728)	398 (267/131)	0.82	13.4	5.408 ± 0.027	0.361 ± 0.003	0.12
	[N II]	Low- z : 1.3896 – 1.7338 (1.5366)	104 (79/25)	0.81	7.1	5.307 ± 0.044	0.353 ± 0.005	0.11
		Mid- z : 2.0151 – 2.5605 (2.2981)	294 (188/106)	0.82	11.2	5.085 ± 0.040	0.320 ± 0.005	0.13

^a Statistics are presented for the relationship between $\log[W/\text{\AA}]$ for the line (or lines) listed under column heading “Line” and the property listed under column heading “Attribute.”

^b Redshift range and mean redshift of objects in this subsample.

^c Total number of objects and the number of detections and non-detections of the line (or lines) listed under column heading “Line.”

^d Spearman rank correlation coefficient and the number of standard deviations by which the correlation deviates from the null hypothesis of no correlation.

^e Intercept and slope of the best-fit linear function to the composite averages and the rms of the data points about this best-fit linear function.